

TRACING ABUNDANCES IN GALAXIES WITH THE SPITZER SPACE
TELESCOPE INFRARED SPECTROGRAPH

A Dissertation

Presented to the Faculty of the Graduate School
of Cornell University

in Partial Fulfillment of the Requirements for the Degree of
Doctor of Philosophy

by

Shannon Laura Gutenkunst

May 2008

© 2008 Shannon Laura Gutenkunst
ALL RIGHTS RESERVED

TRACING ABUNDANCES IN GALAXIES WITH THE SPITZER SPACE
TELESCOPE INFRARED SPECTROGRAPH

Shannon Laura Gutenkunst, Ph.D.

Cornell University 2008

As a galaxy evolves, its stars change the amounts (abundances) of elements within it. Thus determining the abundances of these elements in different locations within a galaxy traces its evolution. This dissertation presents abundances of planetary nebulae in our Galaxy and of H II regions in a nearby galaxy (M51). Observations at optical wavelengths dominated such studies in the past. However, abundances determined from infrared lines have the advantages that they are less affected by extinction and the adopted electron temperature. We employ spectra from the *Spitzer Space Telescope* Infrared Spectrograph and derive abundances for argon, neon, sulfur, and oxygen. These elements are not usually affected by nucleosynthesis in the progenitor stars of planetary nebulae, and thus their abundances trace the amounts of these elements in the progenitor cloud. The abundances of these elements in H II regions trace the amounts of these elements in the interstellar medium today. We do a case study of abundances in the planetary nebula IC 2448, finding that it has subsolar abundances, which indicates that the progenitor star formed out of subsolar material. We also derive abundances and assess the dust properties of eleven planetary nebulae in the Bulge of the Milky Way. We find that the abundances from these planetary nebulae do not follow the abundance trend observed in planetary nebulae in the Disk. This points toward separate evolution for the Bulge and Disk components. Additionally, we find peculiar dust properties in planetary nebulae in the Bulge which indicate that the progenitors of these

nebulae evolved in binaries. Finally, we make a pilot study of the abundances in H II regions across the galaxy M51.

BIOGRAPHICAL SKETCH

Shannon was born on May 23, 1979 in Albuquerque, New Mexico to Norman and Sharon Guiles. They all moved to Redlands, California when Shannon was six months old. Her brother, Jason, was born there on February 3, 1981, and Shannon cannot remember life without him. As Shannon grew up, her father helped her when she got stuck on math or science homework and her mother taught her how to learn from books. She also learned a lot from tutoring her brother in math when he wanted help.

Shannon graduated from Redlands High School in 1997. She went on to attend the University of California, San Diego (UCSD) where she received her Bachelor's Degree in Physics in 2001. During her undergraduate years she participated in three Research Experience for Undergraduates (REU) programs: (1) with Prof. Ami Berkowitz at UCSD on magnetic materials, (2) in Prof. Michael Wiescher's group at the University of Notre Dame in nuclear physics, and (3) with Prof. George Fuller at UCSD in theoretical astrophysics. The most enjoyable of these REU programs was working with George Fuller, who encouraged her in applying to graduate schools, and for part of the year after she graduated she continued to work with him and his graduate student Jason Pruet.

In August of 2002, Shannon and her mom took a road trip to Ithaca, New York where Shannon became a graduate student in the Department of Physics at Cornell University. During her first summer in graduate school she worked in biophysics with Prof. Carl Frank, but ultimately decided that biophysics was not for her. After her second year in graduate school she joined Prof. Jim Houck's group in Astronomy, and she has worked in this group for the last four years, with her work in this group culminating in her dissertation. She also met her husband, Ryan Gutenkunst, while at Cornell, and they married on April 29, 2007.

To my husband Ryan, my parents Sharon and Norman Guiles, my brother Jason
Guiles, and my grandma Frieda Maloney.

ACKNOWLEDGEMENTS

First and foremost, I thank Jeronimo Bernard-Salas, who mentored me during my last two years of research. The work I have done with him forms the bulk of this dissertation. I am grateful to him for paying attention when I needed help, for sharing and explaining his code for calculating abundances, and for finding my mistakes and pointing me in the right direction to fix them (although of course any mistakes left in this dissertation are my fault and not his). Thanks also to Jim Houck for providing me with such a great opportunity to work on data from the *Spitzer Space Telescope* Infrared Spectrograph. I feel fortunate that I happened to be a graduate student when and where I had the chance to work with data from such an important instrument. Additionally, thanks to all of the other members of my special committee: Terry Herter, Saul Teukolsky, and Ira Wasserman.

I thank the past and present members of the *Spitzer* IRS group at Cornell whom I have had the pleasure to work with (in alphabetical order): Don Barry, Jeronimo Bernard-Salas, Bernhard Brandl, Vassilis Charmandaris, Daniel Devost, Duncan Farrah, Elise Furlan, Peter Hall, Lei Hao, Terry Herter, James Higdon, Sarah Higdon, Jim Houck, Jason Marshall, Laurie McCall, Greg Sloan, Henrik Spoon, Keven Uchida, Dan Weedman, and Yanling Wu. All of them have helped me at some point, and their support has meant a lot to me. I would like to single out Don Barry who kept my computer running happily, Elise Furlan for teaching me the intricacies of SMART, Peter Hall for keeping SMART running, Laurie McCall for keeping things in the group running smoothly, Greg Sloan for answering my questions about dust, and Yanling Wu for being a kind and supportive office mate who never hesitated to answer my questions.

Thanks to all of my co-authors on the two papers about planetary nebulae. Jeronimo Bernard-Salas and Stuart Pottasch gave me thorough comments and

suggestions on the two papers, which indubitably made the papers fly through the review process with ease; their expertise in the subject helped immensely. Jeronimo also planned the observations on which the second paper was based. Also thanks to my other co-authors on those papers: Tom Roellig (who planned the observations on which the first paper was based), Greg Sloan (who helped with the interpretation of the dust features in the second paper), and Jim Houck (who gave me helpful comments on both papers and donated the IRS GTO time for the observations for the second paper).

I also thank Daniel Devost and Terry Herter for helping me with a project to take data at Palomar, and to Thomas Jarrett for showing me how to best use the WIRC instrument there for narrow-band imaging and setting me up to use his data reduction software. Thanks to James Lloyd and Don Banfield for letting me use some of their telescope time to learn how to use the WIRC instrument before my observing run. Thanks also to the night assistant there, Jean Mueller.

Also thanks to NASA for funding my research. This work is based in part on observations made with the *Spitzer Space Telescope*, which is operated by the Jet Propulsion Laboratory, California Institute of Technology under NASA contract 1407. Support for this work was provided by NASA through Contract Number 1257184 issued by JPL/Caltech.

Additionally, I thank the members of the Ithaca Area Toastmasters Club. Their support and positive feedback have helped me improve my public speaking skills, which in turn helped me when I gave presentations on my work and talks for outreach. I also found their friendship, cheer, and different outlook on life invaluable.

Finally, I thank my family. My parents and grandparents always encouraged me to do my best, and without that encouragement I would not be here. My brother is one of my best friends, and I appreciate his support. Most of all, I

thank my husband Ryan. The rest of my family lives across the country. Ryan's presence here and his love, support, and encouragement helped buoy me through the deep and sometimes turbulent waters of graduate school.

TABLE OF CONTENTS

Biographical Sketch	iii
Dedication	iv
Acknowledgements	v
Table of Contents	viii
List of Tables	x
List of Figures	xi
1 Introduction	1
1.1 Elements and the Evolution of the Galaxy	2
1.1.1 Creation of the Elements	2
1.1.2 Formation and Evolution of the Galaxy	4
1.2 Photoionization Regions	7
1.2.1 Planetary Nebulae	10
1.2.2 H II Regions	12
1.3 What We Can Learn from Spectra of Photoionization Regions	13
1.3.1 Extinction	13
1.3.2 Electron Density and Temperature	14
1.3.3 Abundances	15
1.3.4 Ionizing Radiation Field	20
1.4 Dust: Gemstones and Carcinogens in Space	21
1.4.1 Silicates	23
1.4.2 Polycyclic Aromatic Hydrocarbons (PAHs)	25
1.5 Observing with the Spitzer Space Telescope	26
1.6 In This Dissertation	29
2 The <i>Spitzer</i> IRS Infrared Spectrum and Abundances of the Planetary Nebula IC 2448	30
2.1 Abstract	30
2.2 Introduction	30
2.3 Spitzer Observations and Data Reduction	32
2.4 Optical and UV Data	38
2.5 Data Analysis	40
2.5.1 Extinction Correction	40
2.5.2 Electron Density	42
2.5.3 Electron Temperature	43
2.5.4 Abundances	43
2.6 Discussion	47
2.7 Conclusions	50

3	Chemical Abundances and Dust in Planetary Nebulae in the Galactic Bulge	52
3.1	Abstract	52
3.2	Introduction	53
3.3	Spitzer IRS Data	55
3.3.1	Observations	55
3.3.2	Source Selection	55
3.3.3	Data Reduction	59
3.4	Supplementary Data	60
3.5	Data Analysis	66
3.5.1	Abundances	66
3.5.2	Crystalline Silicates	76
3.5.3	PAHs	76
3.6	Discussion	77
3.6.1	Elemental Abundances	77
3.6.2	Crystalline Silicates	90
3.6.3	PAHs	92
3.6.4	Dual Chemistry Nebulae	93
3.7	Conclusions	94
4	Abundances in H II Regions Across M51 from <i>Spitzer</i> Spectra	96
4.1	Introduction	96
4.2	Observations and Data Reduction	98
4.2.1	Spitzer Data	98
4.2.2	H α Map	103
4.3	Data Analysis	105
4.3.1	Extinction Correction	105
4.3.2	Electron Temperature and Density	105
4.3.3	Abundances	106
4.4	Discussion	108
4.4.1	Ionizing Radiation Field	108
4.4.2	Neon to Sulfur Abundance Ratio	109
4.5	Conclusions	110

LIST OF TABLES

1.1	Atomic data references	19
2.1	<i>Spitzer</i> IRS observed line fluxes of IC 2448	37
2.2	Extinction corrected optical line fluxes of IC 2448	39
2.3	Selected observed ultraviolet line fluxes of IC 2448	39
2.4	Derivation of extinction coefficient from H I lines	41
2.5	Electron densities assuming $T_e = 12700$ K	43
2.6	Electron temperatures assuming $N_e = 1860$ cm ⁻³	44
2.7	Ionic and elemental abundances	44
2.8	Comparison of abundances in IC 2448 to other sources	45
3.1	Positions and AORkeys for observed GBPNe	57
3.2	Properties of observed GBPNe	58
3.3	Multiplicative scaling factors for GBPNe spectra	62
3.4	Observed infrared line fluxes	64
3.5	Extinction corrected optical line fluxes for our GBPNe	65
3.6	Comparison of the derived $C_{H\beta}$ with the literature	68
3.7	Electron temperatures and densities	72
3.8	Adopted parameters for determining abundances	73
3.9	Ionic abundances	74
3.10	Comparison of total elemental abundances for individual GBPNe	75
3.11	Net PAH feature fluxes	81
3.12	Comparison of mean Bulge abundances	85
3.13	Abundances of PNe and H II regions across the Galaxy	87
3.14	Parameters of linear fits to abundance gradients	90
4.1	M51 H II region data	101
4.2	M51 H II region line fluxes	103
4.3	Abundances in M51 H II regions	107

LIST OF FIGURES

1.1	Diagram of the structure of the Milky Way	5
1.2	Example IRS spectrum	9
1.3	Configuration as well as N_e and T_e diagnostics for S III	16
1.4	Synthetic spectra of the radiation from an instantaneous starburst	22
1.5	Example of crystalline silicate features in an IRS spectrum	24
1.6	Image of an olivine grain	24
1.7	Structure of forsterite	25
1.8	Example structures of PAH molecules	26
1.9	Example of PAH features in an IRS spectrum	27
2.1	The <i>Spitzer</i> IRS spectrum of IC 2448.	35
2.2	Close-ups of emission lines in the <i>Spitzer</i> spectrum of IC 2448	36
3.1	<i>Spitzer</i> IRS spectra of our GBPNe	63
3.2	Continuum subtracted spectra showing crystalline silicates	80
3.3	Profiles of PAH features	82
3.4	Abundances of Bulge and Disk PNe versus galactocentric distance	89
3.5	Comparison of mean 28 and 33 μm silicate features	91
4.1	SINGS $H\alpha$ continuum subtracted image of M51	99
4.2	IRS spectra of H II regions in M51	102
4.3	M51 H II region Ne III/Ne II flux ratio versus distance	108
4.4	M51 $(\text{Ne}^+ + \text{Ne}^{++}) / (\text{S}^{++} + \text{S}^{3+})$ abundance ratio versus distance	109

CHAPTER 1

INTRODUCTION

On Earth, some snakes in the pit viper family have sacks on the sides of their heads that allow them to detect infrared light, or heat. This ability to “see” in the infrared allows the snakes to detect delectable rodents in dark underground tunnels where there is no optical light. Just as viewing objects on Earth in the infrared can uncover secrets hidden from optical light, viewing objects in space in the infrared allows astronomers to probe precious pieces of the cosmos unseen in the optical. For example, dust hinders optical studies because it absorbs optical light, but this same dust re-radiates the light in the infrared. Astronomers can identify the type of dust by looking at the features they produce in the infrared spectra (see §1.4).

Infrared spectra also allow astronomers to determine the amounts of various elements (abundances) by measuring fluxes in infrared emission lines. Abundances from different locations in a galaxy give information about its formation and evolution. In the past, observations at optical wavelengths dominated abundance studies. However, studies at other wavelengths give new insights. This dissertation concentrates on what we can learn from infrared spectra of photoionization regions (specifically planetary nebulae and H II regions) in our Galaxy and M51 (NGC 5194). First we derive abundances of the planetary nebula IC 2448 in the Disk of the Milky Way, finding that it has abundances of argon, neon, sulfur, and oxygen slightly lower than solar which implies that the cloud from which the progenitor star formed had a subsolar abundance. Then we derive abundances for eleven planetary nebulae in the Galactic Bulge, finding that these nebulae do not follow the trend of abundance versus galactocentric distance displayed by nebulae in the Disk, thus indicating the separate evolution of the Bulge and the Disk. Ad-

ditionally we find that these nebulae in the Bulge have different dust properties than typical for nebulae in the Disk, and the dust signatures indicate that the progenitors of many of the Bulge nebulae probably evolved in binary systems. Finally we derive abundances from H II regions across M51; while we cannot derive accurate abundances with respect to hydrogen, we can make an approximation of the neon to sulfur abundance ratio which appears to show that Ne/S decreases with increasing distance from the center, but this probably is not a real affect.

The next section (§1.1) discusses the formation of elements and how determining elemental abundances in different parts of a galaxy gives clues about how it formed and evolved. §1.2 summarizes the important properties of photoionization regions that are relevant to this work. Then §1.3 discusses what we can learn from spectra of these photoionization regions. §1.4 discusses the types of dust which produce features in infrared spectra of planetary nebulae and H II regions. §1.5 gives information about the *Spitzer Space Telescope* Infrared Spectrograph (IRS) which made the bulk of the observations for this dissertation. Finally §1.6 gives a brief description of the remaining chapters of the dissertation.

1.1 Elements and the Evolution of the Galaxy

1.1.1 Creation of the Elements

Big Bang nucleosynthesis created the elements of hydrogen, helium, lithium, and trace amounts of beryllium. Stars create the rest. Understanding what types of stars make which elements and on what timescales these elements form is vital for understanding how galaxies form and evolve. A summary of when various elements are made in different types of stars follows; for more details see Matteucci (2001) on which this discussion is based.

Massive stars with masses above $\sim 8 M_{\odot}$ end their lives in core collapse (Type

II and Ib/c) supernovae (SNe) explosions. They produce the bulk of the oxygen, the principal element in the global abundance, as well as the bulk of other α -elements (such as argon, neon, and sulfur) which are formed by fusing together α particles (helium-4 nuclei, He^{+2}) either in the core of the star or during the explosion (Matteucci, 2008). These supernova also produce other heavy elements through the r-process, the *rapid* capture of neutrons onto seed nuclei relative to the timescale of β decay (Woosley et al., 1994). Such massive stars have short lifetimes in the range of 1 to 10 Myr.

Type Ia SNe caused by exploding white dwarfs in binary systems produce most ($\sim 70\%$) of the iron and small amounts of other heavy elements (Matteucci & Greggio, 1986). Because the progenitors of these Type Ia SNe are low-intermediate mass stars, they have long lifetimes of several 10 Myr to over 10 Gyr. These low mass stars live longer than the massive stars which produce oxygen and other α -elements, and thus there is a delay between the iron and α -element enrichment of the ISM for a group of stars which formed at the same time. Thus the abundance ratio of α -elements to iron $[\alpha/\text{Fe}]$ can serve as a ‘cosmic clock’.

Low and intermediate mass stars with masses in the range ~ 0.8 to $\sim 8 M_{\odot}$ ignite helium in their core and dredge-up episodes occur which bring the processed material from the core to the surface. The stars then eject some of their material in stellar winds during the Red Giant Branch (RGB) and Asymptotic Giant Branch (AGB) phases (Iben & Renzini, 1983). Radiation from the central star ionizes this ejected material which then “lights up” during a planetary nebula (PN) phase before the star ends its life as a carbon-oxygen white dwarf. In this way the stars restore part of their processed and unprocessed material to the interstellar medium, enriching the interstellar medium in helium, carbon, nitrogen, and the heavy s-process elements which are made by the *slow* capture of neutrons onto

seed nuclei relative to the β decay timescale (Iben & Renzini, 1983). While each of these stars has much less mass and evolves more slowly than a massive star, the Galaxy contains many more of these low-intermediate mass stars, and they probably produce most of the nitrogen and carbon in the interstellar medium today (Chiappini et al., 2003), making carbon mainly as a primary element and making nitrogen mainly as a secondary element during hydrogen burning (in the CNO cycle).

In summary, stars with masses ($\sim 8 M_{\odot}$ – $100 M_{\odot}$) which explode as core collapse SNe make most of the α -elements (like oxygen, neon, sulfur, and argon) as well as heavy r-process elements on short timescales (1–10 Myr). Low–intermediate mass stars that end their lives as Type Ia SNe produce most of the iron and limited amounts of other heavy elements on long timescales (10 Myr to 10+ Gyr). The other low–intermediate mass stars produce helium, carbon, nitrogen and heavy s-process elements, releasing their material into the interstellar medium also on long timescales. The abundance ratio of an element released in to the interstellar medium on a short timescale to that of an element released on a long timescale serves as a cosmic clock, revealing the nature of the chemical evolution of a galaxy.

1.1.2 Formation and Evolution of the Galaxy

Figure 1.1 shows a diagram of the different parts of the Milky Way. The Disk (including the Thin and Thick Disks) contains gas and stars. The Thin Disk contains most of the mass of the Disk and the young stars; the Thick Disk contains only a few percent of the total mass of the Disk and most of the old stars. The Bulge resides at the center of the Disk, and a spherical Outer Halo of stars surrounds the Disk and Bulge, with a spherical dark matter Halo extending out beyond the stellar Halo (Carroll & Ostlie, 1996). The Inner Halo of stars has a more squashed

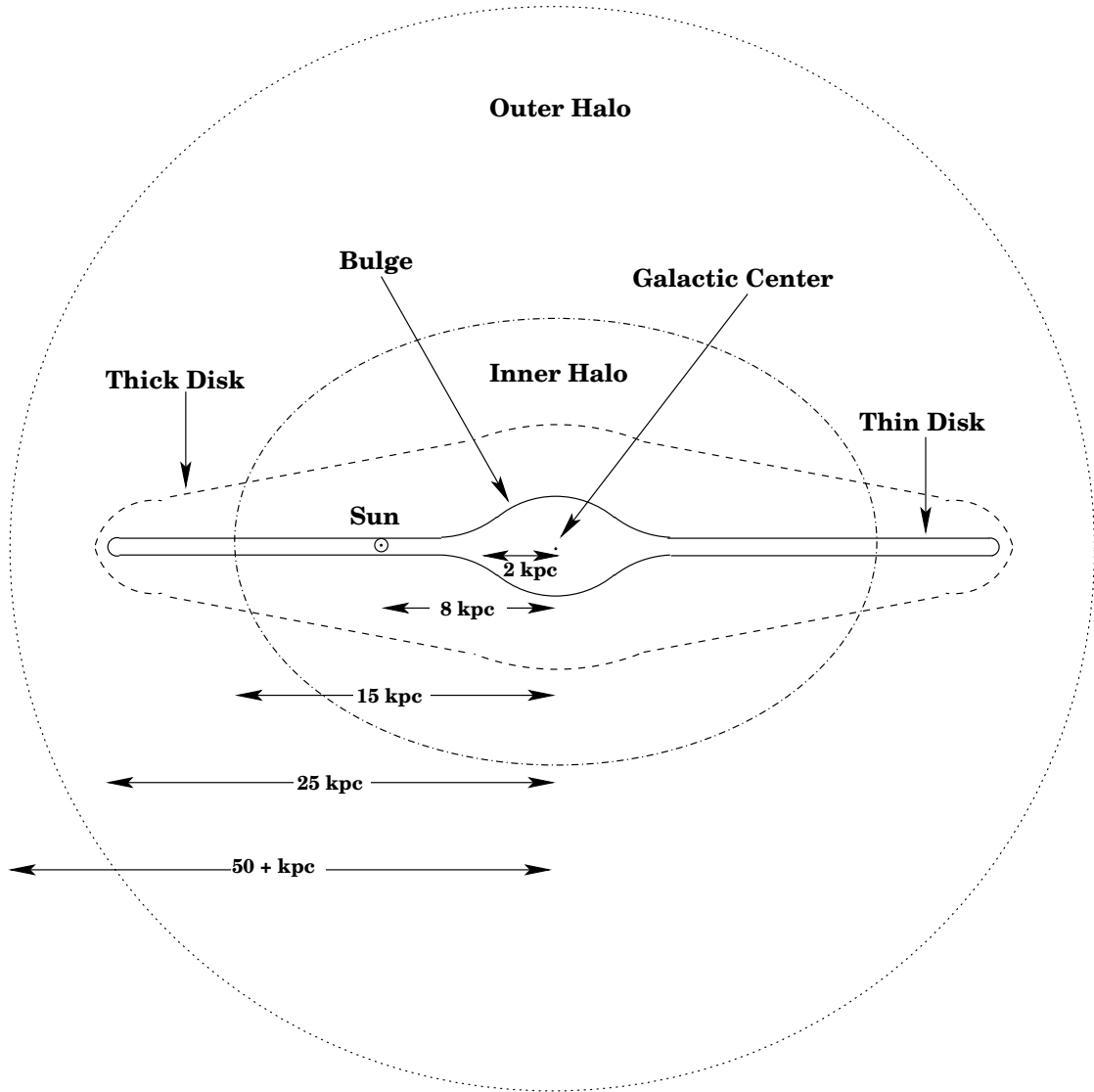


Figure 1.1 Diagram of the structure of the Milky Way; not to scale. Figure design after Matteucci (2001) Figure 1.1; distances in the figure taken from Carroll & Ostlie (1996), except for the boundary between the Inner and Outer Halo not given in Carroll & Ostlie (1996) which is from Carollo et al. (2007). The Outer stellar Halo extends out to a radius of about 50 kpc, but the dark matter Halo extends beyond a radius of 100 kpc.

shape (Carollo et al., 2007). These different parts of the Galaxy have different chemical compositions which gives information about their evolution, as discussed below.

Determining how the Galaxy formed and evolved from the abundances and motions of stars began in the 1960's with the paper by Eggen et al. (1962). They found that high velocity stars with lower abundances move in more elliptical orbits and have smaller angular momenta than stars with higher abundances, and they concluded that the old low abundance stars populate a Halo formed out of a quick infall of a cloud of gas. In the 1970's Searle & Zinn (1978) questioned this picture of Halo formation. They found that some globular clusters in the Halo were much older than others, implying that the Halo could not have formed as quickly as proposed by Eggen et al. (1962). They suggested that the Halo formed out of many cloud fragments, which may themselves already have formed stars and globular clusters.

Radial elemental abundance gradients indicate how the Disk formed. Different elements can have different gradients because they are made in different processes in stars. That is, the gradient of each element depends on the timescale for production (and release into the interstellar medium) of that element. For example, nitrogen and iron have slightly steeper gradients than oxygen because long-lived low to intermediate mass stars produce most of the nitrogen (released during the PN phase) and iron (from Type Ia SNe) whereas short-lived high mass stars produce most of the oxygen; additionally nitrogen is a secondary element and thus is produced proportionally to the original oxygen abundance. Characterizing these abundances gives important information on when star formation occurred in different regions of the Galaxy (Matteucci, 2001).

Several studies comparing galactic chemical evolution models of the Milky Way

with observationally derived abundances give the following description of its formation and evolution, but this is still an area of active research. The Inner Halo and Bulge form out of an infall episode on a short timescale of ~ 1 Gyr (Buonanno et al., 1994; Ballero et al., 2007). The Outer Halo forms with a longer timescale of ~ 5 Gyr by accreting satellite stellar systems and/or extragalactic gas (Buonanno et al., 1994; Carollo et al., 2007). The Thin Disk forms out of another infall episode *inside-out* and more slowly — with the timescale increasing linearly with galactocentric distance with a value of ~ 7 Gyr in the solar neighborhood (Chiappini et al., 1997). The *inside-out* Disk formation is brought about because the outer parts of the Disk form later as gas with higher angular momentum settles into the plane of the Disk at larger radii, and this theory can reproduce the observed abundance gradients along the Disk (Matteucci, 2001). The Thick Disk may have formed from mergers of satellite galaxies with the primordial Thin Disk (Quinn et al., 1993). Other spiral galaxies may form through similar processes.

1.2 Photoionization Regions

Photoionization regions are present around newly formed stars (H II regions), dying stars (planetary nebulae, PNe), and accreting black holes; the following discussion on such regions is based on Ferland (2003) and Osterbrock (1989) where the reader can find further details. Ultraviolet (and optical to a lesser extent) photons emitted by a radiation source (such as a star) inside or nearby a gaseous nebula heat its dust grains to ~ 100 K which then re-radiate the energy in the infrared, causing the continuum in infrared spectra. Additionally these photons collide with atomic hydrogen (hydrogen being the most abundant element in the Universe and in these nebulae) and photionize it. The photoelectrons ejected in this process then (elastically) collide with each other and ions, reaching a Maxwell-

Boltzmann velocity distribution characterized by a unique electron temperature, which is usually between 5000 and 20000 K. A typical photoelectron remains in the continuum for several years, often (elastically) colliding with other photoelectrons, and every few weeks or so it (inelastically) collides with an ion, losing part of its kinetic energy to internal excitations in the ion.

At the low densities of these nebulae ($N_e \lesssim 10^4 \text{ cm}^{-3}$) collisional de-excitation of these excited levels of ions does not occur often, and thus these excited levels radiate photons to reach the ground state, causing forbidden lines in the spectra of these nebulae. The lines are called ‘forbidden’ because the energy transitions which produce them (electric quadrupole or magnetic dipole) are less likely to occur than the ‘permitted’ (electric dipole) transitions; additionally the forbidden lines cannot be seen in laboratory experiments on Earth because even in the best man-made vacuum the density is high enough for collisional de-excitation to occur. The permitted transitions do not dominate the spectra of photoionization regions because they often require a very high energy to excite (and would only occur in the far-UV), and thus it is important to study the forbidden transitions in photoionization regions.

Measuring the fluxes of these forbidden lines along with other information allows us to determine elemental abundances in these regions, as discussed more in §1.3.3. The brightest forbidden lines are labeled in the the *Spitzer* IRS spectrum of the Bulge planetary nebulae PNG000.7+04.7 shown in Figure 1.2. The forbidden lines are denoted by square brackets surrounding an abbreviation of the element and a roman numeral equal to the ionization state plus one, e.g. a forbidden line of O^{+3} is denoted by [O IV].

In a photoionization region, an ion (usually hydrogen or helium) will eventually recapture a thermal photoelectron, producing a free-bound photon, and the balance

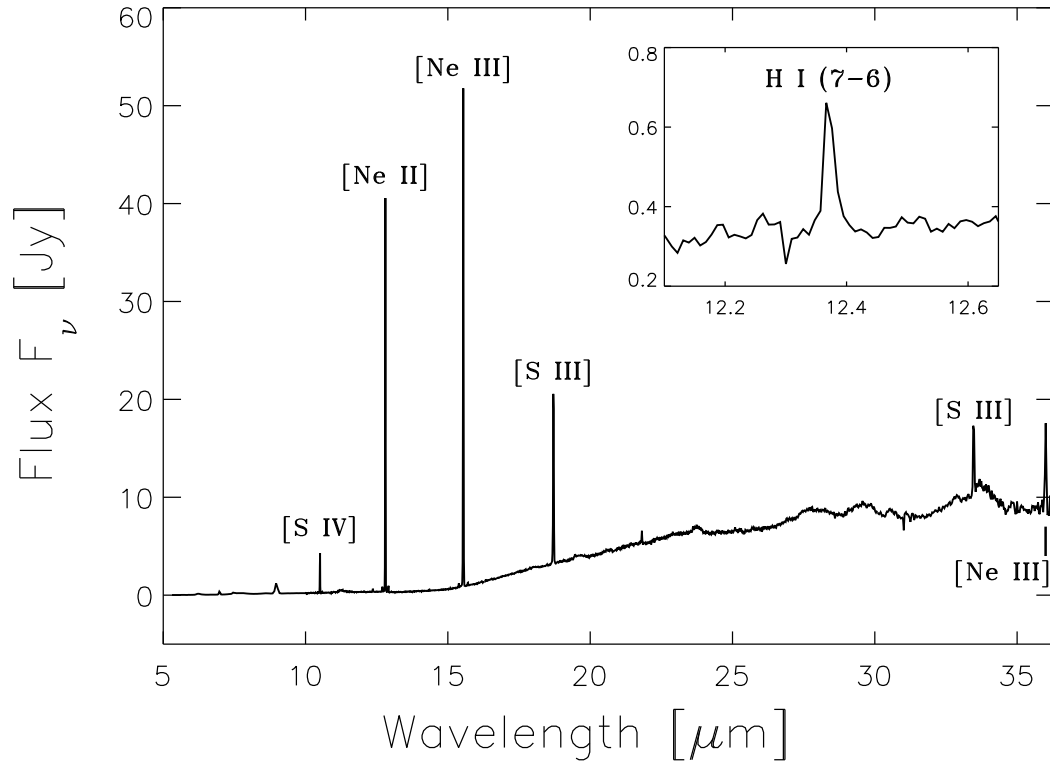


Figure 1.2 Example IRS spectrum the Bulge planetary nebula PNG000.7+04.7. The above spectrum results from averaging the fluxes from the two nod positions and scaling the flux in each module to the module with the highest flux (LH). The spectrum consists of low resolution data below 10 μm and high resolution data above 10 μm . Bright lines are labeled. The inset shows a close-up of the spectrum around the H I(7-6) Humphreys- α line at 12.37 μm .

between recapture and photoionization sets the degree of ionization in each part of the nebula. The ion recaptures the electron to an excited level in the process called recombination, and the excited atom decays to lower levels by radiating photons. When a hydrogen ion (H^+) recombines with an electron (leading to an excited H^0 atom), the excited H^0 atom decays to the ground state by emitting a series of photons which generate the H I recombination lines, such as the H I(6-5) Pfund- α line at $7.46 \mu\text{m}$ and the H I(7-6) Humphreys- α line at $12.37 \mu\text{m}$ observed in *Spitzer* spectra of photoionization regions. Figure 1.2 shows a close-up of the Humphreys- α line observed in the spectrum of PNG000.7+04.7. Other elements such as helium also emit recombination lines.

1.2.1 Planetary Nebulae

The name “planetary” is a misnomer and was originally derived from the fact that when PNe were studied through small telescopes over two hundred years ago they looked like planets. The name “nebula”, Latin for “cloud” is, however, more appropriate. Huggins & Miller (1864) were the first to look at planetary nebulae through a spectrograph, finding that the spectra of these nebulae differed significantly from those of stars. The planetary nebulae showed only three bright emission lines with little continuum emission in their spectra, and Huggins & Miller (1864) remark *“In place of an incandescent solid or liquid body transmitting light of all [wavelengths] through an atmosphere which intercepts by absorption a certain number of them, such as our sun appears to be, we must probably regard these objects, or at least their photo-surfaces, as enormous masses of luminous gas or vapour. For it is alone from matter in the gaseous state that light consisting of certain definite [wavelengths] only, as is the case with the light of these nebulae, is known to be emitted.”* This marked the beginning of our understanding of the physical nature

of these beautiful objects. Recent references on which this discussion about them is based are: Pottasch (1984), Osterbrock (1989), and Bernard-Salas (2003).

The blown off outer layers of a star form the gas cloud of a planetary nebula. This low density ($\sim 10^2\text{--}10^4\text{ cm}^{-3}$) gas is illuminated by a low to intermediate mass ($\sim 1\text{--}8 M_{\odot}$) hot ($T_{*} \sim 3 \times 10^4\text{--}2 \times 10^5\text{ K}$) central star which is evolving quickly towards a white-dwarf. The nebula expands at $\sim 100\text{ km sec}^{-1}$, and as it expands the density and emission decrease, so that they become unobservable in a few ten thousand years. Most PNe have a higher ionization level of elements than H II regions due to the higher temperatures of their central stars, but the lower-ionization PNe have similar spectra to H II regions. PNe can have many shapes and are observed in our Galaxy and nearby galaxies. They are concentrated in the Galactic plane and the center of the Galaxy.

PNe have strong forbidden lines in their spectra, which may be employed to derive abundances, as discussed in §1.3.3. A series of dredge-up events that occur as the central star evolves bring the products of nucleosynthesis from the core of the star (such as helium, carbon, and nitrogen) to the surface of the star. Additionally, for stars more massive than $\sim 4\text{--}4.5 M_{\odot}$, hot bottom burning leads to the production of elements in nuclear processing at the bottom of the convective envelope of the star. Stellar winds then push the outer envelope of the star out into the interstellar medium. Measuring the abundances of these elements in the PN then gives information about the nucleosynthesis processes inside the star. However, the abundances of elements not affected by nucleosynthesis in the central star (such as argon, neon, and sulfur) give information about the initial composition of the cloud from which the star formed, and thus about the chemical evolution of the interstellar medium at the time that the star formed. Abundances from PNe across the Galaxy give information about the chemical evolution of the Galaxy as

a whole. Additionally, abundances from different types of PNe can be employed in order to probe different time scales during the evolution of the Galaxy.

1.2.2 H II Regions

H II regions are gaseous nebulae excited by young massive main sequence stars. They derive their name from the fact that they contain mostly ionized hydrogen. (PNe contain mostly ionized hydrogen as well, but the name H II region is reserved for clouds of gas heated by young massive stars.) The central radiation source of H II regions is a hot (effective temperature $T_* \sim 40000$ K) high-mass star ($M_* \gtrsim \text{few } M_\odot$) or set of stars. The nebulae contain ionized hydrogen, singly ionized helium, and mostly single or double ionization stages of other elements. The electron density is typically 10 to 100 cm^{-3} but may range up to several thousands. H II regions are observed across our Galaxy and in other nearby galaxies, and they are most common in spirals and irregulars. In spiral galaxies the H II regions are concentrated in the disk in the spiral arms, whereas in irregulars their distribution is not as well organized (Osterbrock, 1989).

H II regions are young and therefore they trace the composition of the interstellar medium today. The abundance gradient of H II regions across the Galaxy was first measured by Shaver et al. (1983) using optical and radio recombination lines. They determined an oxygen abundance gradient of $\frac{\Delta \log_{10}(O/H)}{\Delta R_G} = -0.07 \pm 0.015 \text{ dex kpc}^{-1}$ across the Disk (the unit dex refers to the \log_{10} scale). Some more recent studies employ infrared lines in determining abundances across the Disk of the Galaxy (e.g Simpson et al., 1995). Additionally we can determine abundances of H II regions in external galaxies; Chapter 4 discusses some infrared derived abundances for H II regions across the galaxy M51.

1.3 What We Can Learn from Spectra of Photoionization Regions

Ratios of hydrogen recombination line fluxes from photoionization regions determine the extinction toward them. Ratios of emission line fluxes from such regions aid in the determination of the physical conditions there, such as the electron density (N_e) and temperature (T_e), the chemical composition of the gas, and the properties of the ionizing radiation field. Additionally, features in the continua of spectra identify the kinds of dust present there. An extensive body of literature covers this topic, and this discussion is based on Ferland (2003) and Osterbrock (1989).

1.3.1 Extinction

We derive the extinction toward these regions in two ways. Both involve comparing the observed $H\beta$ line flux with a predicted actual $H\beta$ line flux (the flux from the $H\beta$ line if there were no extinction) in order to infer the logarithmic extinction at $H\beta$, $C_{H\beta}$:

$$C_{H\beta} = \log_{10} \left(\frac{F_{H\beta} \text{ actual}}{F_{H\beta} \text{ observed}} \right)$$

In the first method, we predict the actual optical $H\beta$ line flux from observed infrared H I line fluxes, which will give a value close to the actual $H\beta$ flux because the small particles which cause the extinction have little effect on the longer wavelength infrared light. In order to predict the actual $H\beta$ flux from an infrared H I line flux, we adopt theoretical ratios of hydrogen recombination lines (e.g. Hummer & Storey, 1987) and assume Case B recombination (which assumes a large optical depth in the H I lines and thus the line photons are scattered multiple times and converted into photons with lower energies before escaping the nebula) for a gas

at the appropriate temperature and density for the region.

In the second method, we predict the actual $H\beta$ flux from the radio flux at 6 cm (S_{6cm}), and this will again give a value close to the actual $H\beta$ flux because the extinction in the radio is small compared to that in the optical. We assume that the nebula is optically thin and that the 6 cm radio continuum is due to free-free emission produced by the close approach of electrons with H^+ , He^+ , and He^{++} , and we employ the following formula from Pottasch (1984) in order to obtain the predicted $H\beta$ flux:

$$F(H\beta)_{6cm}^{actual} = \frac{S_{6cm}}{2.82 \times 10^9 t^{0.53} (1 + He^+/H^+ + 3.7He^{++}/H^+)}$$

where $t \equiv T_e/10^4$ K, and 2.82×10^9 converts units so that S_{6cm} is in Jy and $F(H\beta)$ is in $\text{erg cm}^{-2} \text{ s}^{-1}$.

1.3.2 Electron Density and Temperature

The **electron density** (N_e) can be determined from flux ratios of pairs of lines from the same ion that originate from levels with similar excitation energies, which ensures that the relative excitation rates for each level depend only on their collisional strengths (and not on T_e). Thus as long as the two levels have different collisional de-excitation rates or radiative transition probabilities, the relative population of the levels depends on N_e (Osterbrock, 1989). For example, the ratio of the [S III] infrared line fluxes, $F([\text{S III}] \text{ at } 18.7 \mu\text{m})/F([\text{S III}] \text{ at } 33.5 \mu\text{m})$, is frequently employed to determine N_e . Astronomers have observed these line fluxes and used their ratio to infer densities in ionized regions for over twenty-five years (e.g. Herter et al., 1982). Figure 1.3 (a) shows an energy level diagram for the ground state of S III and some of its fine structure transitions, including the transition from the 3P_2 level to the 3P_1 at $18.7 \mu\text{m}$ and the transition from the 3P_1 level

to the 3P_0 at $33.5 \mu\text{m}$. Figure 1.3 (b) shows the predicted line flux ratio $F([\text{S III}] 18.7 \mu\text{m})/F([\text{S III}] 33.5 \mu\text{m})$ as a function of the log of the electron density for several values of the electron temperature. The electron density is best determined by this ratio for values of the ratio between ~ 1 and 11, corresponding to densities between $\sim 10^3$ and 10^5 cm^{-3} , and it only has a small dependence on T_e . However, other line ratios may also be used to determine N_e ; for example, the ratio $F([\text{O II}] 3729 \text{ \AA})/F([\text{O II}] 3726 \text{ \AA})$ which is more sensitive to slightly lower densities.

The **electron temperature** (T_e) can be determined by ratios of fluxes of pairs of emission lines emitted by a single ion from two upper levels which differ significantly in excitation energy. This ensures that the relative population of the levels depends on T_e (Osterbrock, 1989). For example, the line flux ratio $F([\text{S III}] \text{ at } 6312 \text{ \AA})/F([\text{S III}] \text{ at } 18.7 \mu\text{m})$ may be used to determine T_e . The $[\text{S III}]$ line at 6312 \AA comes from the upper 1S level while the $18.7 \mu\text{m}$ line arises from one of the lower 3P levels (see Figure 1.3 (a)). The large difference in energy between the 1S and 3P levels leads to the relative rates of excitation of these levels depending strongly on T_e (the higher the temperature, the more the 1S level is populated relative to the 3P levels), and thus it is possible to use the flux ratio of lines emitted from these levels to determine T_e (see Figure 1.3 (c)).

1.3.3 Abundances

Once the electron density and temperature are determined, it is possible to derive abundances of ions and elements by number with respect to hydrogen. In order to determine ionic abundances we take the ratio of an ionic line flux to the $H\beta$ line flux. Then, we sum the ionic abundances for all of its expected stages of ionization to determine the total elemental abundance of an element. If an ionization stage is unobserved but expected to be present, we adopt an ionization correction factor

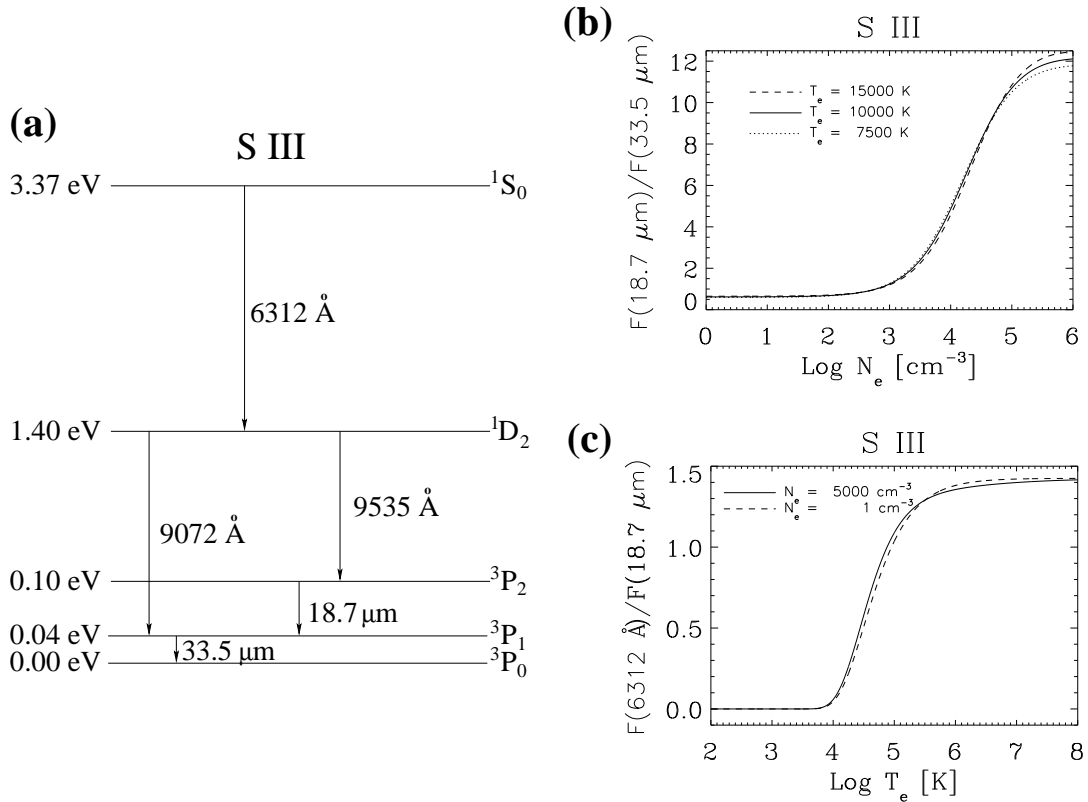


Figure 1.3 (a) The ground level configuration for S III. The splitting of the ground 3P term is exaggerated in the figure, as can be seen from the energies marked on the left side. (b) The theoretical ratio of the [S III] $18.7 \mu\text{m}$ line flux over the [S III] $33.5 \mu\text{m}$ line flux as a function of the log of the electron density. The separate curves are for different adopted electron temperatures. (c) The theoretical ratio of the [S III] 6312 \AA line flux over the [S III] $18.7 \mu\text{m}$ line flux as a function of the log of the electron temperature. The separate curves are for different adopted electron densities.

(ICF) to account for it.

A program written by Jeronimo Bernard-Salas solves for the population of the levels and ionic abundances following equations found, for example, in Osterbrock (1989). This program assumes a five level atom which serves as a good approximation because the upper levels are only sparsely populated. The populations of the levels are found by assuming statistical equilibrium for each level i :

$$\underbrace{\sum_{j \neq i} n_j N_e q_{ij}}_{\substack{\text{collisional} \\ \text{(de)excitation} \\ \text{rate}}} + \underbrace{\sum_{j > i} n_j A_{ji}}_{\substack{\text{radiative} \\ \text{transition} \\ \text{rate from all} \\ \text{upper levels}}} = \underbrace{\sum_{j \neq i} n_i N_e q_{ij}}_{\substack{\text{collisional} \\ \text{(de)excitation} \\ \text{rate}}} + \underbrace{\sum_{j < i} n_i A_{ij}}_{\substack{\text{radiative} \\ \text{transition} \\ \text{rate from} \\ \text{level } i}} \quad (1.1)$$

where n_i is the fraction of the population of the ion in level i , q_{ij} is the electron (de)excitation rate coefficient ($\text{cm}^3 \text{s}^{-1}$), and A_{ij} is the radiative transition probability (s^{-1}) from level i to level j . Additionally, for normalization, the fraction of the ion in all of the different levels sum to unity,

$$\sum_i n_i = 1. \quad (1.2)$$

The electron (de)excitation rate coefficients depend on T_e , the statistical weight of level i which accounts for the number of states with energy i (ω_i), and the effective collisional strength $\Omega(j, i)$ according to:

$$q_{ij} = \frac{8.63 \times 10^{-6} \Omega(j, i)}{T_e^{1/2} \omega_i} \text{ cm}^{-3} \text{ s}^{-1}. \quad (1.3)$$

The atomic data (values of A and Ω) which the program employs are mainly from two references: Mendoza (1983) and the IRON Project (Hummer et al., 1993)¹; see Table 1.1 for a complete list of references for the atomic data for each ion for which abundances are obtained in this dissertation. In order to determine abundances, we employ the relation between the intensity of the extinction corrected ionic line

¹<http://vizier.u-strasbg.fr/tipbase/home.html>

(I_{ion}), the radiative transition rate for the line between the upper and lower levels (A_{ul}), the total population in the upper level ($N_{\text{ion}} n_{\text{u}}$ where N_{ion} is the total population density of the ion and n_{u} is the ratio of the population density of the upper level from which the line originates to N_{ion}), and the energy of the line ($h\nu_{\text{ul}}$):

$$I_{\text{ion}} \propto A_{\text{ul}} N_{\text{ion}} n_{\text{u}} h\nu_{\text{ul}}. \quad (1.4)$$

Additionally we use the relation between the intensity of the extinction corrected H β line ($I_{\text{H}\beta}$), the effective recombination coefficient for H β ($\alpha_{\text{H}\beta}$), the density of protons (N_{H^+}), the density of electrons (N_{e}), and the energy of the line ($h\nu_{\text{H}\beta}$):

$$I_{\text{H}\beta} \propto \alpha_{\text{H}\beta} N_{\text{H}^+} N_{\text{e}} h\nu_{\text{H}\beta}. \quad (1.5)$$

Taking the ratio of these intensities and re-arranging, ionic abundances with respect to hydrogen ($N_{\text{ion}}/N_{\text{H}^+}$) are given by (Bernard-Salas et al., 2001):

$$\frac{N_{\text{ion}}}{N_{\text{H}^+}} = \frac{I_{\text{ion}} N_{\text{e}} \lambda_{\text{ul}} \alpha_{\text{H}\beta}}{I_{\text{H}\beta} n_{\text{u}} \lambda_{\text{H}\beta} A_{\text{ul}}}. \quad (1.6)$$

The bulk of the program for determining abundances is then in determining n_{u} (the fraction of the total population of the ion in the level from which the line originates) according to Equation 1.1.

Abundances derived from infrared lines have several advantages over those determined from optical lines (Rubin et al., 1988; Pottasch & Beintema, 1999). (1) There is less extinction in the infrared than the optical, and thus extinction-corrected line fluxes (from which abundances are derived) are more accurate in the infrared than in the optical because uncertainties in the extinction coefficient and law affect the infrared line fluxes less. This is especially true in areas of high extinction, such as the Galactic Bulge. (2) Infrared lines arise from levels close to the ground level and thus abundances determined from them do not depend as much on the adopted electron temperature as abundances determined from optical

Table 1.1 Atomic data references. We downloaded data from the IRON Project on 19 October 2006 from TIPbase at: <http://vizier.u-strasbg.fr/tipbase/home.html> . Energies of the levels are all from Mendoza (1983).

Ion	Effective Collisional Strength (Ω)	Transition Probability (A)
Ar ⁺	IRON Project	Mendoza (1983)
Ar ⁺⁺	IRON Project	IRON Project
Ar ⁺³	Ramsbottom et al. (1997)	Mendoza (1983)
Ar ⁺⁴	IRON Project	IRON Project
C ⁺	Blum & Pradhan (1992)	IRON Project & Mendoza (1983)
C ⁺⁺	Berrington (1985) & Berrington et al. (1985)	Mendoza (1983)
C ⁺³	Mendoza (1983)	Mendoza (1983)
Mg ⁺⁴	IRON Project	IRON Project
N ⁺	IRON Project	IRON Project & Mendoza (1983)
N ⁺⁺	Blum & Pradhan (1992)	Mendoza (1983)
N ⁺³	Ramsbottom et al. (1994)	Mendoza (1983)
N ⁺⁴	Mendoza (1983)	Mendoza (1983)
Ne ⁺	IRON Project	Mendoza (1983)
Ne ⁺⁺	IRON Project	IRON Project
Ne ⁺³	Mendoza (1983)	Mendoza (1983)
Ne ⁺⁴	IRON Project	Galavis et al. (1997)
O ⁺	Pradhan et al. (2006)	Mendoza (1983)
O ⁺⁺	IRON Project	IRON Project & Mendoza (1983)
O ⁺³	IRON Project	IRON Project
S ⁺	Keenan et al. (1996)	Mendoza (1983)
S ⁺⁺	IRON Project	IRON Project
S ⁺³	IRON Project	Mendoza (1983)

lines. For example, changing the adopted T_e from 10000 K to 13000 K for the PN IC 2448 decreases the abundance of Ne^{++} derived from the IR [Ne III] line at $15.55 \mu\text{m}$ by 6% but decreases the abundance of Ne^{++} derived from the optical [Ne III] line at 3869 \AA by 80%. (3) Some ions have lines in the infrared, but not in the optical; for example, infrared spectra show the [Ne II] line which is not observable in the optical, but this ion dominates the total elemental neon abundance in low ionization nebulae.

1.3.4 Ionizing Radiation Field

Massive stars and active galactic nuclei produce a hard radiation field (a radiation field which contains a large fraction of highly energetic photons) of high intensity. The hardness of a radiation field gives information about the type of source creating the field. Ratios of IR lines arising from ions which have ionization energies in the ultraviolet indicate the radiation field hardness. For example, it takes 22 eV to create Ne^+ from neutral neon and 41 eV to create Ne^{++} from Ne^+ , so if the line flux ratio $F(\text{Ne III at } 15.6\mu\text{m})/F(\text{Ne II at } 12.8 \mu\text{m})$ is high, then the ionizing radiation field is hard. Similarly it takes 23 eV to create S^{++} from S^+ and 35 eV to create S^{+3} from S^{++} , so the line flux ratio $F(\text{S IV at } 10.5 \mu\text{m})/F(\text{S III at } 18.7 \mu\text{m})$ also probes the ionizing radiation field. Figure 1.4 shows the ionization energies for these ions overplotted on synthetic spectra for a burst of star formation generated with the code Starburst99².

Several factors affect the hardness of the radiation field. Figure 1.4 shows four synthetic spectra: one for each of two abundances (1 and 1/3 solar) and one for each of two times (1 and 10 Myr) after the burst of star formation began. The radiation field is harder, having higher energy photons (to the left in the figure)

²Starburst99 (Leitherer et al., 1999) is available from the following website: <http://www.stsci.edu/science/starburst99/>.

at the younger time (1 Myr) than at the older time (10 Myr). This shows up in infrared ionization line ratios because at early times stars produce photons hard enough to form Ne^{++} and S^{+3} and thus produce Ne III and S IV lines in the infrared spectra, but as the stars evolve off the main sequence they cool and do not produce such hard photons, and the Ne III and S IV lines become weaker and finally disappear in the infrared spectra. Additionally, the radiation field is harder at lower abundances: at higher photon energies (left in Figure 1.4) the lower abundance $1/3 Z_{\odot}$ synthetic spectra lie above and to the left of the higher abundance $1 Z_{\odot}$ spectra. Thus a hard radiation field may be caused by radiation from a group of stars that are either young or have low abundances.

1.4 Dust: Gemstones and Carcinogens in Space

Dust dramatically alters the spectra of galaxies: typically $\gtrsim 30\%$ of starlight is absorbed by dust and then reradiated in the infrared (Bernstein et al., 2002). Additionally, dust grains efficiently radiate away heat, which helps stars form by removing the energy from a collapsing cloud (Mathis, 1990). After star formation, dust is necessary to create planets and life. While elemental abundances can give information about the evolution of the Galaxy, studying the dust can give information about the evolution of stars.

RGB and AGB stars produce the bulk of the dust observed in the interstellar medium, although novae, Wolf-Rayet stars, and supernovae may contribute some as well. The most abundant elements in the atmospheres of these giant stars after hydrogen and helium are oxygen and carbon. Due to the stability of the CO molecule, CO forms in these stars until the supply of either carbon or oxygen is exhausted. This leads to a dichotomy in the type of dust produced: if the star has $\text{C}/\text{O} < 1$ then oxygen-rich dust such as oxides, quartz (SiO_2) and silicates forms; if

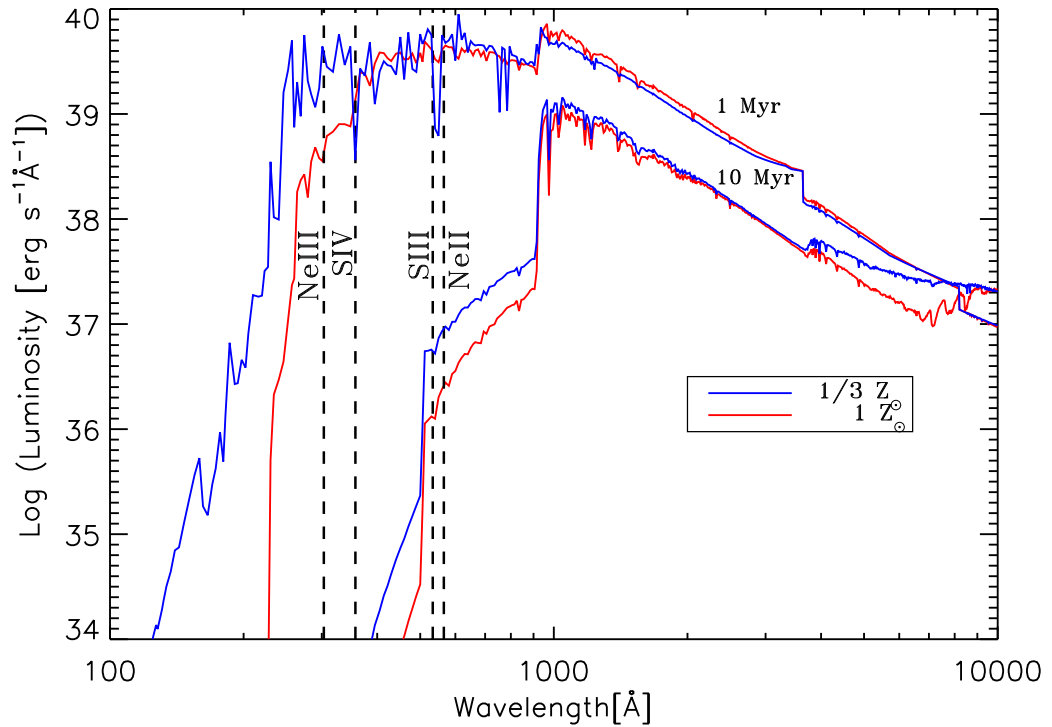


Figure 1.4 Starburst99 synthetic spectra of the stellar radiation from an instantaneous burst of star formation at two different abundances and ionization energies of Ne II, Ne III, S III and S IV. The blue lines indicate star formation at one third of the solar abundance, and the red lines indicate star formation at the solar abundance. The two different sets of tracks indicate spectra of a starburst that began 1 Myr and 10 Myr ago as labeled.

the star has $C/O > 1$ then carbon-rich dust such as silicon carbide (SiC), graphite, and polycyclic aromatic hydrocarbons (PAHs) forms (Mathis, 1990). The types of dust observed in objects discussed in this dissertation are silicates and PAHs, and are discussed more in detail below.

1.4.1 Silicates

Amorphous silicates emit broad solid state features at ~ 10 and $18 \mu\text{m}$ as well as a broad continuum in their infrared spectra which are observable by the *Spitzer* IRS. The Si-O stretching mode causes the $10 \mu\text{m}$ feature and the O-Si-O bending mode causes the $18 \mu\text{m}$ feature. The absence of substructure in these features indicates that the silicates are amorphous (having a disordered lattice structure) rather than crystalline (having long-range order in the lattice structure) (Draine, 2003).

Crystalline silicates emit features beyond $20 \mu\text{m}$. Figure 1.5 shows these crystalline silicate features in the continuum-subtracted IRS spectrum of one of the Bulge PNe. Crystalline silicate features are not usually observed below $20 \mu\text{m}$ due to the cool temperature ($\lesssim 100 \text{ K}$) of the dust. The spectral positions of the sharp solid state features produced by crystalline silicates imply that they are made of molecules such as forsterite (Mg_2SiO_4) and enstatite (MgSiO_3) and do not contain much iron. Spectra in this dissertation contain features at $23.7 \mu\text{m}$ due to forsterite, as well as complexes of features around 28 and $33 \mu\text{m}$ due to forsterite and enstatite (Molster 2000; see Figure 1.5). Figure 1.6 shows a picture of olivine ($(\text{Mg,Fe})_2\text{SiO}_4$), the crystalline silicate mineral found in the gemstone peridot, and Figure 1.7 diagrams the structure of forsterite. The spectral features of amorphous silicates are less pronounced than those of the crystalline silicates and thus it proves more difficult to infer their chemical composition (Molster, 2000).

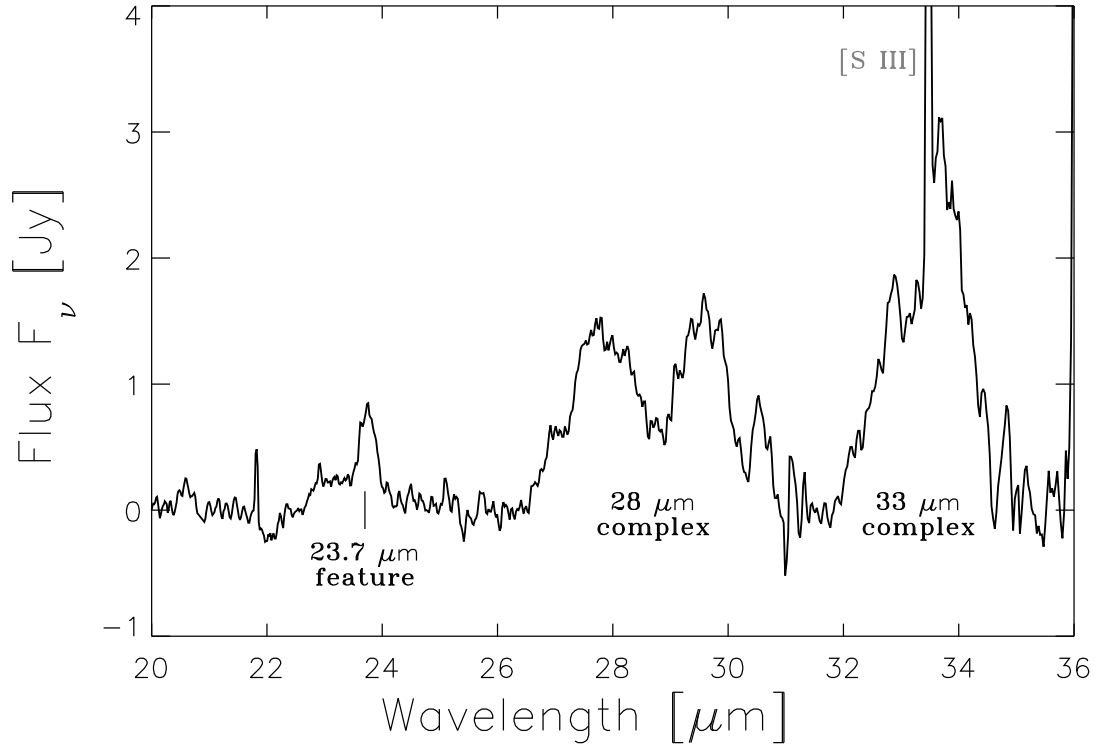
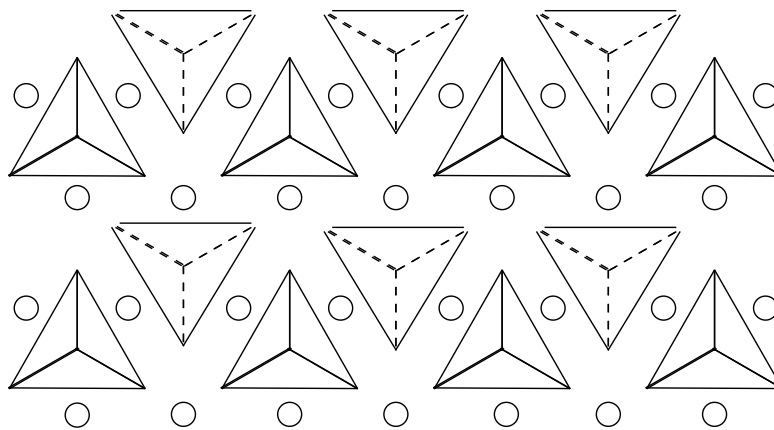


Figure 1.5 Example of crystalline silicate features in the continuum-subtracted high resolution IRS spectrum of the Bulge planetary nebula PNG000.7+04.7. The crystalline silicate features as well as the strong [S III] emission line are labeled.



Figure 1.6 Image of an olivine ($(\text{Mg,Fe})_2\text{SiO}_4$) grain. Copyright 2004 by Andrew Alden, geology.about.com, reproduced under educational fair use, and available at: <http://geology.about.com/library/bl/images/blolivine.htm>.



Forsterite (Mg_2SiO_4)

Figure 1.7 Structure of forsterite (Mg_2SiO_4). The tetrahedra represent anions of SiO_4^{-4} having an O^{-2} anion at each vertex and a Si^{+4} cation in the center. The circles represent Mg^{+2} cations. Diagram designed after one at: http://www2.odn.ne.jp/7n2pmw/meteorphy2/metphys_v12.htm.

1.4.2 Polycyclic Aromatic Hydrocarbons (PAHs)

PAHs are planar molecules made from building blocks of benzene rings containing six carbon atoms which are stuck together (like chicken wire) and that have hydrogen atoms around the periphery. For example structures of these molecules see Figure 1.8. On Earth, the incomplete combustion of carbon-containing fuels (e.g. coal, tobacco, and incense) creates these carcinogenic PAH molecules (Leger et al., 1987; BBC, 2001). In space, giant stars probably create most of the PAHs as discussed above. In our Galaxy, radiation in PAH bands accounts for $\sim 1/7$ of the reprocessing of starlight by dust, and thus PAHs serve as significant radiative coolants of the interstellar medium; additionally PAHs contain $\sim 15\text{--}20\%$ of the carbon in the interstellar medium (Galliano et al., 2008).

Spitzer IRS spectra of many H II regions and PNe (and other sources) show emission from vibrational transitions in PAHs in the $5\text{--}15\ \mu\text{m}$ range. Figure 1.9 shows these features in the continuum-subtracted IRS spectrum of a Bulge PN.

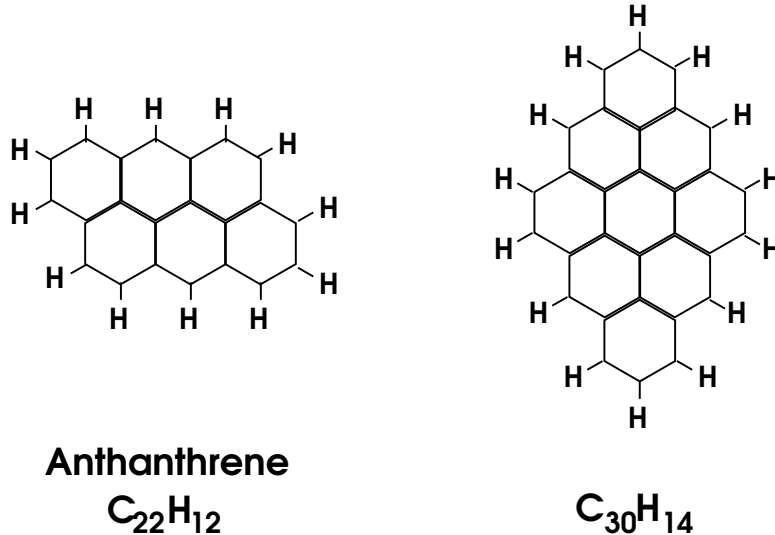


Figure 1.8 Example structures of PAH molecules following Allamandola et al. (1989). The vertices of the hexagons represent carbon atoms.

When a PAH molecule absorbs an energetic (UV or optical) photon, it quickly ($\sim 10^{-12}$ – 10^{-10} s) redistributes the energy over the vibrational modes of the PAH, and then the PAH relaxes to the ground state by emitting IR photons over the next seconds to hours, producing features such as the ones found at 6.2, 7.7, 8.6, 11.2, and 12.7 μm (Draine & Li, 2001; Li & Draine, 2002). A C–C stretching mode produces the 6.2 and 7.7 μm features, a C–H in-plane bending mode causes the 8.6 μm feature, and C–H out-of-plane bending gives rise to the 11.2 and 12.7 μm features. PAHs with sizes between twenty and forty carbon atoms are probably the dominant emitters of these features (Allamandola et al., 1989). The type of PAHs formed gives indications about the material from which they were made as well as their thermal history (Leger et al., 1987).

1.5 Observing with the Spitzer Space Telescope

This dissertation employs infrared data from the *Spitzer Space Telescope*. It has an 85 cm diameter and was launched August 25, 2003 and is expected to have a $\sim 5+$

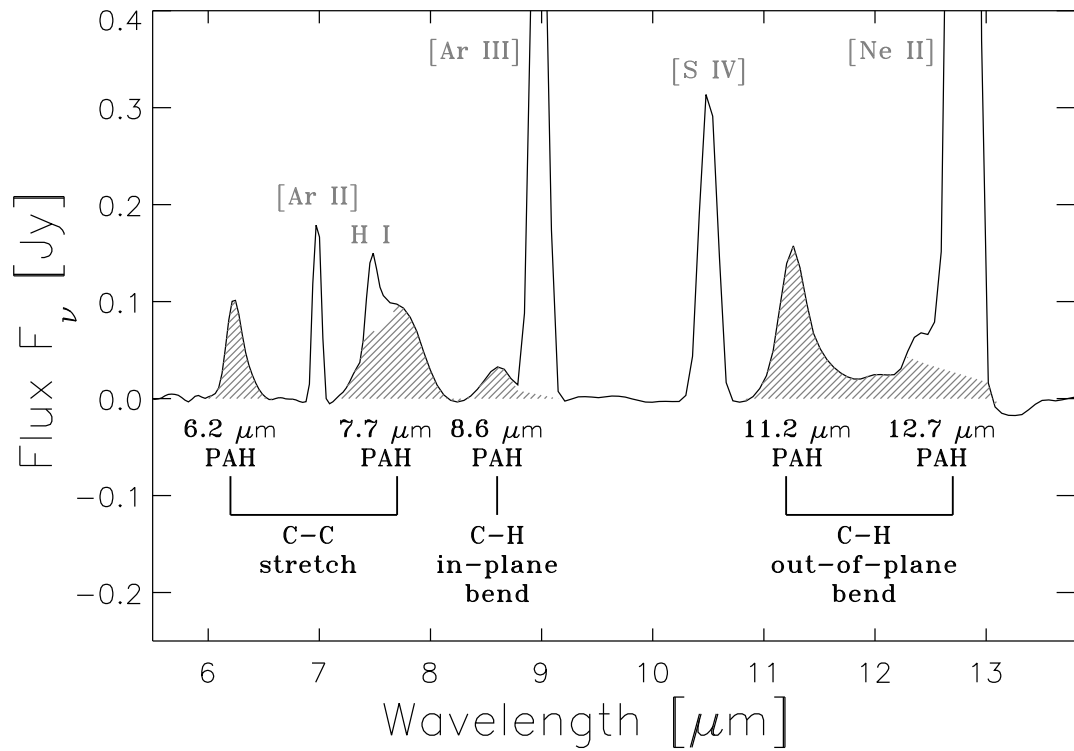


Figure 1.9 Example of PAH features (shaded) in the continuum-subtracted IRS low resolution spectrum of the Bulge planetary nebula PNG000.7+04.7. The PAH features and the strong emission lines are labeled.

year lifetime. *Spitzer* is in an Earth-trailing solar orbit. It has three instruments: the Infrared Array Camera, the Multiband Infrared Photometer, and the Infrared Spectrograph (Werner et al., 2004). This dissertation mainly employs data from the Infrared Spectrograph, and so this instrument is described in more detail below.

The Infrared Spectrograph (IRS; Houck et al., 2004) has four different modules covering wavelengths from 5 to 38 μm . It has two low spectral resolution modules (Short-Low (SL) and Long-Low (LL)) with $R \equiv \lambda/\Delta\lambda \sim 90$, and it has two high resolution modules (Short-High (SH) and Long-High (LH)) with $R \sim 600$. The low resolution modules cover the whole wavelength range of the IRS and are sensitive to the features in the continuum (e.g. crystalline silicate and polycyclic aromatic hydrocarbon (PAH) dust features), while the high resolution modules cover the wavelength range 10–37 μm and are better for studying emission lines. The observer may choose to blindly point the telescope with $\sim 1''$ positional accuracy, or choose the PCRS or PeakUp options with $0.4''$ positional accuracy.

Spectra from *Spitzer* have the advantage that they are free of atmospheric absorption and the background in space is six orders of magnitude smaller than on Earth, leading to a thousand-fold gain in sensitivity (Houck et al., 2004). Previous infrared telescope missions in space paved the way for *Spitzer* such as the *Infrared Astronomical Satellite (IRAS)* and the *Infrared Space Observatory (ISO)*. *ISO* studied PNe in our Galaxy within a few kpc of the Sun and galactic H II regions as well as some extragalactic ones. Due to its more modern detector arrays, *Spitzer* has greater sensitivity than these previous IR space telescopes. Current *Spitzer* studies build on this previous work; for example, Chapter 3 of this dissertation presents *Spitzer* data on eleven PNe in the Bulge of our Galaxy, a region far enough away that it was difficult for *ISO* to probe the PNe there. Additionally, the *Spitzer* IRS can do spectral maps, and *ISO* could not; Chapter 4 employs data

from *Spitzer* IRS maps of H II regions. Observations of dust features and emission lines with the *Spitzer* IRS allow us to probe the physical conditions in a variety of environments — e.g. the planetary nebulae and H II regions discussed in this dissertation. Knowing these physical conditions is important for understanding chemical evolution in galaxies as discussed above.

1.6 In This Dissertation

The following chapters present *Spitzer* IRS data on planetary nebulae and H II regions. Specifically, Chapter 2 presents the case study of abundances in the planetary nebula IC 2448. Chapter 3 discusses abundances and dust in eleven planetary nebulae in the Bulge of the Galaxy. Finally, Chapter 4 gives abundance results for H II regions across the galaxy M51.

CHAPTER 2

THE *SPITZER* IRS INFRARED SPECTRUM AND ABUNDANCES OF THE PLANETARY NEBULA IC 2448

Paper by S. Guiles (the maiden name of S. Gutenkunst), J. Bernard-Salas, S. R. Pottasch, & T. L. Roellig, 2007, ApJ, 660, 1282

2.1 Abstract

We present the mid-infrared spectrum of the planetary nebula IC 2448. In order to determine the chemical composition of the nebula, we use the infrared line fluxes from the *Spitzer* spectrum along with optical line fluxes from the literature and ultraviolet line fluxes from archival IUE spectra. We determine an extinction of $C_{H\beta} = 0.27$ from hydrogen recombination lines and the ratio to $H\beta$ ratio. Forbidden line ratios give an electron density of 1860 cm^{-3} and an average electron temperature of 12700 K. The use of infrared lines allows us to determine more accurate abundances than previously possible because abundances derived from infrared lines do not vary greatly with the adopted electron temperature and extinction, and additional ionization stages are observed. Elements left mostly unchanged by stellar evolution (Ar, Ne, S, and O) all have subsolar values in IC 2448, indicating that the progenitor star formed out of moderately metal deficient material. Evidence from the *Spitzer* spectrum of IC 2448 supports previous claims that IC 2448 is an old nebula formed from a low mass progenitor star.

2.2 Introduction

Determining accurate abundances of planetary nebulae (PNe) is important for understanding how stars and galaxies evolve (Kaler, 1985). PNe abundances of elements made in low and intermediate mass stars (such as helium, carbon, and

nitrogen) can be used to test stellar evolution models (Kwok, 2000). Abundances of elements which are not changed during evolution of low and intermediate mass stars (such as neon, argon, sulfur, and in some cases oxygen), can give insight into the chemical content of the gas from which the progenitor star formed (Kwok, 2000); thus abundances of PNe dispersed throughout a galaxy can be used to test galactic evolution models.

IC 2448 is an elliptical, average sized PN located at RA = $09^{\text{h}}07^{\text{m}}06^{\text{s}}.26$, DEC = $-69^{\circ}56'30''.7$ (J2000.0, Kerber et al. (2003)). Optical emission line images of IC 2448 show that diffuse [N II] and [O III] emission pervade the same oval region, which agrees with IC 2448 being an old, evolved nebula (Palen et al., 2002). McCarthy et al. (1990) give further evidence for IC 2448's advanced age, finding that its evolutionary age is 8400 years and its dynamical age is 7000 years. IC 2448 has an H α diameter of $10.''7 \times 10.''0$ (Tylenda et al., 2003). Thus at a distance of 2.1 ± 0.6 kpc (Mellema, 2004), IC 2448 has an H α size of 0.11×0.10 pc.

Two optical surveys and one optical+ultraviolet survey of PNe include abundance determinations for IC 2448 (Torres-Peimbert & Peimbert, 1977; Milingo et al., 2002a; Kingsburgh & Barlow, 1994). Here we report the first use of mid-infrared line fluxes from IC 2448 to determine its abundances. Using infrared (IR) lines to derive abundances has several advantages over using optical or ultraviolet (UV) lines (Rubin et al., 1988; Pottasch & Beintema, 1999). First, the correction for extinction in the IR is smaller than in the optical and UV, and therefore errors in the extinction coefficient and law affect IR line fluxes less. Second, IR lines are less sensitive to uncertainties in the electron temperature because they come from levels close to the ground level. Finally, some ions have lines in the IR spectrum of IC 2448, but not in the optical or UV spectra. When combined with ionic lines of these elements observed in the optical and UV, we have line fluxes for more ions of

these elements than previous studies, reducing the need for ionization correction factors (ICFs) to account for unseen ionization stages.

In this paper we use the *Spitzer* IR spectrum supplemented by the optical and UV spectra to derive ionic and total element abundances of He, Ar, Ne, S, O, N, and C in IC 2448. The next section describes the *Spitzer* observations and the data reduction. §2.4 gives the optical and UV data. In §2.5 we derive the extinction, electron density, electron temperature, and ionic and total element abundances. §2.6 compares the abundances of IC 2448 with solar and discusses the nature of the progenitor star and we conclude in §2.7.

2.3 *Spitzer* Observations and Data Reduction

IC 2448 was observed with all four modules (Short-Low (SL), Long-Low (LL), Short-High (SH), and Long-High (LH)) of the Infrared Spectrograph (IRS) (Houck et al., 2004) on the *Spitzer Space Telescope* (Werner et al., 2004) as part of the GTO program ID 45. The AORkeys for IC 2448 are 4112128 (SL, SH, LH observed 2004 July 18), 4112384 (SL, SH, LH off positions observed 2004 July 18), and 12409088 (LL observed 2005 February 17). The data were taken in ‘staring mode’ which acquires spectra at two nod positions along each IRS slit. For the on target AORkeys (4112128 and 12409088), the telescope was pointed at RA = 09^h07^m06^s.4, DEC = −69°56′31″ (J2000.0). For the off target AORkey (4112384), the telescope was pointed at RA = 09^h07^m06^s.6, DEC = −69°58′29″ (J2000.0). Peak-up imaging was performed for AORkey 4112128, but not for the other AORkeys.

The data were processed through version s14.0 of the *Spitzer* Science Center’s pipeline. We begin our analysis with the unflatfielded (*droopres*) images to avoid potential problems in the flatfield. Then we run the *irsclean*¹ program to remove

¹Program available from the *Spitzer* Science Center’s website at <http://ssc.spitzer.caltech.edu>

rogue and flagged pixels, using a mask of rogue pixels from the same campaign as the data. Next we remove the background. To do this we use the off positions for SL, SH, and LH; for LL we use the off order (for example, LL1 nod1 - LL2 nod1). The high resolution spectra (SH and LH) are extracted from the images using a scripted version of the SMART program (Higdon et al., 2004), using full-slit extraction. Due to the extended nature of IC 2448, the low resolution spectra (SL and LL) are extracted from the images manually in SMART using a fixed column extraction window of width 14.0 pixels (25.''2) for SL and 8.0 pixels (40.''8) for LL. The spectra are calibrated by multiplying by the relative spectral response function which is created by dividing the template of a standard star (HR 6348 for SL and LL, and ξ Dra for SH and LH) by the spectrum of the standard star extracted in the same way as the source (Cohen et al. (2003); G. C. Sloan, private communication). Spikes due to deviant pixels missed by the *irsclean* program are removed manually.

The large aperture LH (11''.1 x 22''.3) and LL (10''.5 x 168'') slits are big enough to contain all of the flux from IC 2448. This is supported by the fact that the continuum flux from IC 2448 in LH matches that from LL with no scaling between them. However, the smaller aperture SH (4''.7 x 11''.3) and SL (3''.6 x 57'') slits are too small to contain the entire object. Thus we scale SL up to LL and SH up to LH. SL has a scaling factor of 2.30 and SH has a scaling factor of 3.00. No scaling factor is needed for orders within a module (for example, SL1, SL2, and SL3 all have the same scaling factor of 2.30). Additionally, there is no need of a scaling factor between the two nod positions.

Figure 2.1 shows the average of the two nods of the *Spitzer* IRS spectrum of IC 2448. The peak of the continuum at $\sim 30 \mu\text{m}$ in F_λ units implies that the dust is cool, ~ 100 K. No evidence of polycyclic aromatic hydrocarbons (PAHs) or silicate

dust is seen in the spectrum. We see lines from ions of H, Ar, Ne, S and O in the IR spectrum of IC 2448. Close-ups of the lines in the high resolution *Spitzer* IRS spectrum of IC 2448 are shown in Figure 2.2. High ionization lines of [O IV] (ionization potential IP = 55 eV) and [Ar V] (IP = 60 eV) are observed, but even higher ionization lines such as [Ne V] (IP = 97 eV) and [Mg V] (IP = 109 eV) are not observed, indicating that there is only a moderately hard radiation field. Low ionization lines that would come from the photodissociation region (PDR) such as [Ar II] (IP = 16 eV) and [Si II] (IP = 8 eV) are not observed. A complete list of the observed lines and their fluxes is given in Table 2.1. The highest flux lines in the SH module ($10.51 \mu\text{m}$ [S IV] and $15.55 \mu\text{m}$ [Ne III]) have bumps on each side of them that are instrumental artifacts, possibly resulting from internal reflection in the SH module or an effect of photon-responsivity. The bumps are just visible in Figure 2.2 for the [S IV] line. However, the bumps contain a negligible amount of flux – only $\sim 3\%$ and $\sim 1\%$ of the flux in the main [S IV] and [Ne III] lines respectively, and we did not include these small contributions in our line flux measurements.

The line fluxes are measured interactively in SMART for each nod position by performing a linear fit to the continuum on both sides of the line and then fitting a gaussian to the line. The values of the average line fluxes from both nod positions are given in Table 2.1. We estimate uncertainties in the line fluxes in two ways. In the first method, we propagate the uncertainties in the gaussian fit to the line flux to determine the uncertainty on the average flux from both nod positions. In the second method, we use the standard deviation of the fluxes measured in the two nod positions to determine the uncertainty on the average flux from both nod positions. We then take the final uncertainty as the greater of these two uncertainties. Lines fluxes typically have uncertainties $\lesssim 10\%$; lines with larger uncertainties ($\lesssim 15\%$ and $\lesssim 30\%$) are marked in Table 2.1. We determine 3σ upper

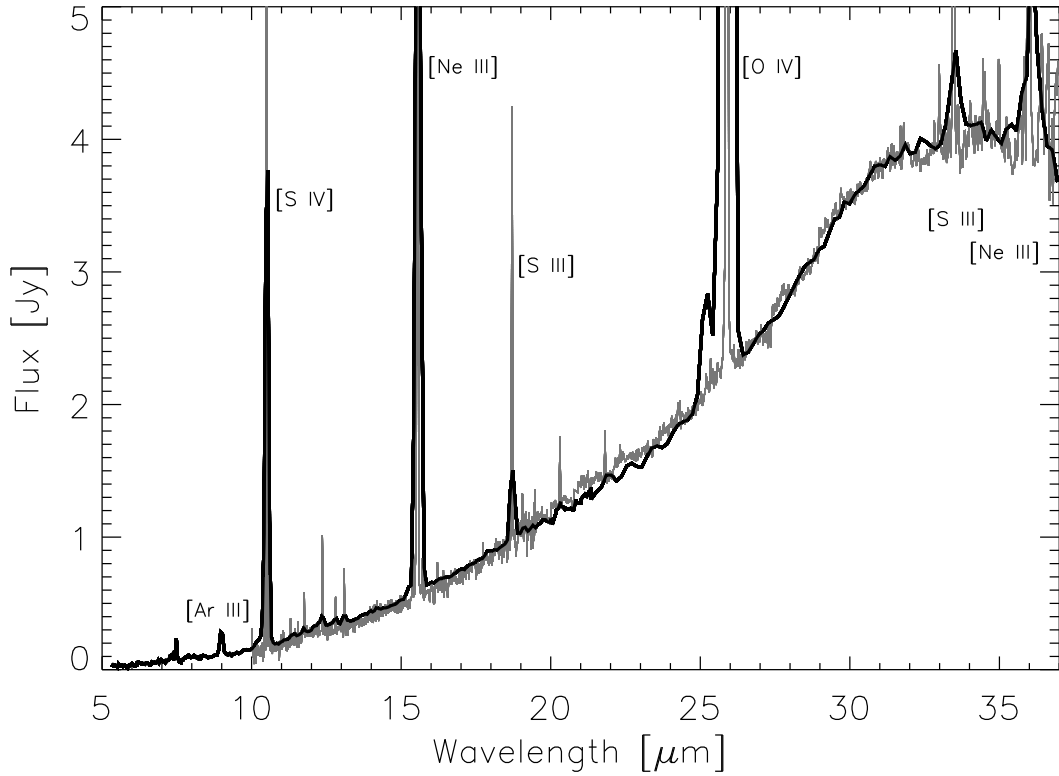


Figure 2.1 The scaled, nod averaged, *Spitzer* IRS spectrum of IC 2448. The low resolution spectrum is shown in black and the high resolution spectrum in grey. SL is scaled up to LL, and SH is scaled up to LH because SL and SH both have small apertures that do not receive the entire flux from IC 2448. Some of the lines have peaks above 5 Jy (the strongest line, O IV at 25.89 μm , peaks at 270 Jy in the HR spectrum), but the y-axis range is restricted in the plot to reveal the continuum.

limits for lines not observed but relevant for the abundance analysis (denoted by a less-than sign in Table 2.1). Upper limits are obtained by calculating the flux contained in a gaussian with width determined by the instrument resolution and height equal to three times the root mean square (RMS) deviation in the spectrum at the wavelength of the line.

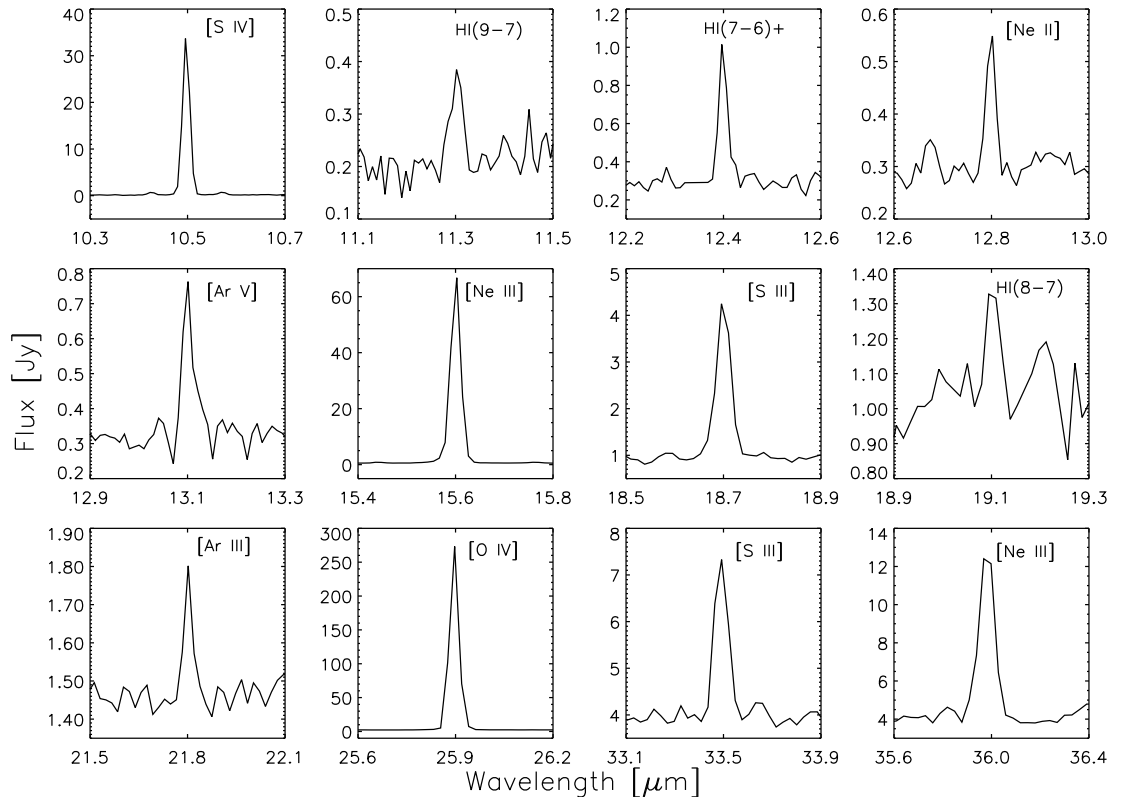


Figure 2.2 Close-ups of emission lines in the scaled, nod averaged *Spitzer* IRS high resolution spectrum of IC 2448. The H I(7-6)+ line is a blend of the H I(7-6) line (which contributes most of the flux) and the H I(11-8) line.

Table 2.1 *Spitzer* IRS observed line fluxes. All fluxes are from the high resolution modules except the lines with $\lambda < 10 \mu\text{m}$ which are from the SL module. A less-than sign indicates a three sigma upper limit.

$\lambda(\mu\text{m})$	Line	Flux ^a	$\lambda(\mu\text{m})$	Line	Flux ^a
6.99	[Ar II]	<13.9	14.32	[Ne V]	<4.83
7.90	[Ar V]	<25.7	15.55	[Ne III]	2080
8.99	[Ar III]	90.7	18.71	[S III]	103
10.51	[S IV]	1780	19.06	H I(8-7)	9.67 ^d
11.30	H I(9-7)	12.0 ^c	21.82	[Ar III]	6.74
12.37	H I(7-6) + ^b	30.5	24.30	[Ne V]	<3.68
12.81	[Ne II]	10.7 ^c	25.89	[O IV]	4280
13.10	[Ar V]	18.3 ^d	33.47	[S III]	62.3
13.53	[Mg V]	<4.36	36.01	[Ne III]	154

^aObserved flux in units of $10^{-14} \text{ erg cm}^{-2} \text{ s}^{-1}$. Flux uncertainties are $\lesssim 10\%$ unless otherwise noted.

^bThe H I(7-6) and H I(11-8) lines are blended in the spectrum.

^cFlux uncertainty $\lesssim 15\%$.

^dFlux uncertainty $\lesssim 30\%$.

2.4 Optical and UV Data

We complement our IR line fluxes with optical and UV line fluxes in order to determine abundances. The optical and UV data provide line fluxes from ions not seen in the infrared spectrum (especially carbon and nitrogen). We obtain optical line fluxes from Milingo et al. (2002b). They observed IC 2448 with the 1.5 m telescope and Cassegrain spectrograph at the Cerro Tololo Inter-American Observatory in the Spring of 1997 using a 5 "x 320" slit. The slit width is about half of the diameter of IC 2448, and so Milingo et al. (2002b) missed some of the nebular flux. We assume that the optical lines measured in the small aperture are representative of the entire nebula of IC 2448 because IC 2448 has evenly distributed optical [N II] and [O III] line emission (Palen et al., 2002). The extinction corrected fluxes for the lines we use are listed in Table 2.2 as given by Milingo et al. (2002b). These authors report uncertainties in their line fluxes of $\lesssim 10\%$ for their strong lines (with strengths $\geq H\beta$) and have flagged uncertainties of $\gtrsim 25\%$ and $\gtrsim 50\%$ for the weaker lines. These uncertainties are given in Table 2.2.

High and low resolution large aperture International Ultraviolet Explorer (IUE) spectra of IC 2448 from the IUE Newly Extracted Spectra (INES) system are available on the web². The high resolution spectra we use are labeled SWP19067 and LWR15096, and the low resolution spectra we use are labeled SWP03194 and LWR02756. We use SMART to measure the line fluxes from the spectra, and the results are listed in Table 2.3. Uncertainties are obtained from the gaussian fit to each line and are $\lesssim 15\%$ unless otherwise noted. The IUE large aperture (10"x 23" ellipse) is big enough to contain essentially all of the flux from IC 2448, and no aperture scaling factor needs to be applied to the spectra.

²The IUE INES system archive website is <http://ines.vilspa.esa.es>

Table 2.2 Extinction corrected optical line fluxes relative to $H\beta=100$ from Milingo et al. (2002b)

λ (Å)	Line	Flux ^a	λ (Å)	Line	Flux ^a
3727	[O II]	5.1 ^b	6584	[N II]	1.0
3869	[Ne III]	103	6717	[S II]	0.1
4070	[S II]	1.1	6731	[S II]	0.1
4363	[O III]	16.4	7005	[Ar V]	0.1
4471	He I	3.3	7135	[Ar III]	4.8
4686	He II	40.3	7236	[Ar IV]	0.1 ^c
4740	[Ar IV]	4.7	7264	[Ar IV]	0.1 ^c
4959	[O III]	386	7323	[O II]	0.6
5007	[O III]	1173	7751	[Ar III]	1.2
5755	[N II]	0.1 ^b	9069	[S III]	2.5
6312	[S III]	0.5	9532	[S III]	5.2
6436	[Ar V]	0.1 ^b			

^aExtinction corrected flux relative to $H\beta=100$. The $H\beta$ flux in the same aperture is 724.4×10^{-14} erg cm⁻² s⁻¹ (Milingo et al., 2002b). Flux uncertainties are $\lesssim 10\%$ unless otherwise noted.

^bFlux uncertainty $\gtrsim 50\%$.

^cFlux uncertainty $\gtrsim 25\%$.

Table 2.3 Selected observed ultraviolet line fluxes

λ (Å)	Line	Flux ^a	λ (Å)	Line	Flux ^a
1241	N V	8.86 ^b	1907	C III]	2250
1483	N IV]	58.5 ^b	2326	C II]	12.6 ^{b,c}
1548	C IV	1900	2422	[Ne IV]	184
1640	He II	2180	2471	[O II]	4.77 ^{b,d}
1750	N III]	75.5			

^aObserved flux in units of 10^{-14} erg cm⁻² s⁻¹. Unless otherwise marked, all fluxes are from IUE low resolution spectra and have uncertainties of $\lesssim 15\%$.

^bFlux from IUE high resolution spectra.

^cFlux uncertainty $\lesssim 50\%$.

^dFlux uncertainty $\lesssim 30\%$.

2.5 Data Analysis

Our goal is to calculate element abundances in IC 2448. In order to do this, we must first determine the extinction toward and physical conditions within the nebula. We iterate to find self-consistent solutions for the electron density and temperature. Then we use the derived values of extinction, electron density, and electron temperature to derive ionic abundances. Finally we sum the observed ionization stages of each element to derive total elemental abundances.

2.5.1 Extinction Correction

We calculate the amount of interstellar extinction in two ways. First, we compare the observed $H\beta$ flux for the whole nebula with the $H\beta$ flux predicted from infrared hydrogen recombination lines for case B recombination for a gas at $T_e = 10\,000$ K and $N_e = 1000\text{ cm}^{-3}$ using the theoretical hydrogen recombination line ratios from Hummer & Storey (1987). The H I(7-6) and H I(11-8) are blended in the spectrum, and theoretically the H I(11-8) line should be 12.26% of the H I(7-6) line (Hummer & Storey, 1987); thus this amount is subtracted out before predicting the $H\beta$ flux from the H I(7-6) line. The results are shown in Table 2.4. Using the average predicted $H\beta$ flux from that table, and the total observed $H\beta$ flux of $1410 \times 10^{-14}\text{ erg cm}^{-2}\text{ s}^{-1}$ (Acker et al., 1992), we obtain $C_{H\beta}=0.33$.

The second method we use to determine the extinction is to compare the observed $H\beta$ flux to that predicted by the 6 cm radio flux using the following equation from Pottasch (1984):

$$F(H\beta) = \frac{S_{6cm}}{2.82 \times 10^9 t^{0.53} (1 + He^+/H^+ + 3.7He^{++}/H^+)}$$

where t is the electron temperature in 10^4 K and 2.82×10^9 does the unit conversion so that S_{6cm} is in Jy and $F(H\beta)$ is in $\text{erg cm}^{-2}\text{ s}^{-1}$. Using ionic helium abundances

Table 2.4 Derivation of extinction coefficient from hydrogen recombination lines

λ (μm)	Line	$F_{LineObserved}^a$	$F_{H\beta Predicted}^b$
11.30	H I(9-7)	12.0	3922
12.37	H I(7-6) + ^c	30.5	2808
19.06	H I(8-7)	9.67	2336
Average predicted H β flux			3022

^aObserved line flux in 10^{-14} erg cm^{-2} s^{-1} .

^bPredicted H β flux in 10^{-14} erg cm^{-2} s^{-1} .

^cThe H I(7-6) and H I(11-8) are blended in the spectrum. The contribution of the H I(11-8) line is removed before predicting the H β flux (see §2.5.1).

from §2.5.4, $t=1.27$, and $S_{6cm} = 0.089 \pm 0.008$ Jy (Gregory et al., 1994), we predict that $F(\text{H}\beta) = 2345 \times 10^{-14}$ erg cm^{-2} s^{-1} , which gives $C_{H\beta} = 0.22$. This value is close to the value derived from the hydrogen recombination lines of $C_{H\beta}=0.33$.

We correct the IR and UV lines for extinction using the average of the results from our infrared hydrogen recombination line and radio predictions, $C_{H\beta} = 0.27$ (corresponding to $E_{B-V} = 0.18$) along with the extinction law from Fluks et al. (1994). We note that our value of the extinction is higher than in some previous studies. Milingo et al. (2002b) use the ratio of H α /H β to get $C_{H\beta} = 0.09$. Torres-Peimbert & Peimbert (1977) use Balmer line ratios to get $C_{H\beta} = 0.15$. Perhaps the short baselines used to measure extinction in those studies led to a low value of $C_{H\beta}$. In contrast, Kingsburgh & Barlow (1994) use radio data to predict H β and get $C_{H\beta} = 0.40$. We use the extinction corrected optical line fluxes from Milingo et al. (2002b) as opposed to applying our own extinction correction to the observed fluxes because their extinction correction gives the correct Balmer decrement and corrects for calibration errors.

2.5.2 Electron Density

We assume an electron temperature (T_e) of 12700 K to derive the electron density (N_e). We justify this choice of T_e in §2.5.3; however, we use ratios of extinction corrected fluxes from pairs of lines of the same ion close in energy to derive the electron density, and these line ratios depend only slightly on T_e , so an error in the adopted T_e will not greatly affect the determination of N_e . The results of the density calculations are shown in Table 2.5. The S II density is unreliable because the lines used to determine it are weak (about 1/1000 of the $H\beta$ flux) and their ratio is in the non-linear regime of the line ratio versus density curve. The Ne III 15.55 μm /36.01 μm ratio is also in the non-linear regime and gives an imprecise density. The Ar III 8.99 μm /21.82 μm ratio is in the low density limit. We adopt a density of $N_e = 1860 \text{ cm}^{-3}$ derived from the S III line ratio as it provides the most accurate measurement of the density.

There is a wide range of values for N_e in the literature. For example, Torres-Peimbert & Peimbert (1977) give N_e from the intersection of [O II] and [N II] line ratios on a plot of T_e vs N_e as 12000 cm^{-3} and N_e from the $H\beta$ flux as 1700 cm^{-3} . Whereas Milingo et al. (2002a) give $N_e = 10 \text{ cm}^{-3}$ from the [S II] lines, which is an inaccurate density indicator in this case as discussed above. Finally Kingsburgh & Barlow (1994) give $N_e = 490 \text{ cm}^{-3}$ from the [Ar IV] 4711 Å/4740 Å lines, but those lines are weak (only $\sim 5\%$ of the $H\beta$ flux), and the 4711 Å line is blended with He I, which makes the density derived from this line ratio unreliable. For the most part, abundances are not greatly affected by the adopted value of the density. For the range of densities for IC 2448 given in the literature ($N_e = 10\text{--}12000 \text{ cm}^{-3}$), all abundances are within 35% of their values for $N_e = 1860 \text{ cm}^{-3}$, except the sulfur abundance which is a factor of two larger at $N_e = 12000 \text{ cm}^{-3}$ than at $N_e = 1860 \text{ cm}^{-3}$.

Table 2.5 Electron densities assuming $T_e = 12700$ K. The S III lines provide the most accurate measurement of the density, and so we assume a density of 1860 cm^{-3} .

ion	lines used (μm)	Ioniz. Potential (eV)	Line Ratio	N_e (cm^{-3})
S II	0.6731/0.6717	10.36	1.00	781
S III	18.71/33.47	23.33	1.66	1860

2.5.3 Electron Temperature

We use extinction corrected fluxes from pairs of lines of the same ion widely separated in energy to derive the electron temperature (T_e) assuming an electron density of $N_e = 1860 \text{ cm}^{-3}$. The results are shown in Table 2.6. It is possible to determine T_e from pairs of ionic lines not in the table (e.g. N II $5755 \text{ \AA}/6584 \text{ \AA}$ and Ar V $7005 \text{ \AA}/13.10 \mu\text{m}$); however, the T_e determined from those ratios is not as accurate because one or both of the lines in each of those ratios is not high quality. We adopt $T_e = 12700$ K from the average of the electron temperatures in the table. We use this value of the temperature in the subsequent abundance analysis. For comparison, Torres-Peimbert & Peimbert (1977) give $T(\text{O III}) = 12500$ K. Milingo et al. (2002a) give $T(\text{O III}) = 12500$ K, $T(\text{N II})=22400$ K, and $T(\text{S III}) = 25200$ K; however, they deem the values of $T(\text{N II})$ and $T(\text{S III})$ unrealistic. Kingsburgh & Barlow (1994) give $T(\text{O III}) = 11000$ K. We note that there is no correlation of T_e with ionization potential, although such a correlation has been noticed in some previous studies (e.g. Pottasch & Beintema (1999); Bernard-Salas et al. (2001)).

2.5.4 Abundances

We use the N_e and T_e given above together with the IR, optical, and UV extinction corrected line fluxes to determine the ionic abundances for ions of Ar, Ne, S,

Table 2.6 Electron temperatures assuming $N_e = 1860 \text{ cm}^{-3}$

ion	lines used (μm)	Ioniz. Potential (eV)	Line Ratio	T_e (K)
S III	0.6312/18.71	23.33	0.125	13900
Ar III	0.7751/8.99	27.63	0.334	11500
O III	0.4363/0.5007	35.12	0.0140	13100
Ne III	0.3869/15.55	40.96	1.27	12400

Table 2.7 Ionic and elemental abundances

Ion	λ (μm)	N_{ion}/N_{H^+}	N_{elem}/N_{H^+}
He ⁺	0.4471	0.060	
He ⁺⁺	0.4686	0.034	0.094
Ar ⁺ ^a	6.99	$<4.21 \times 10^{-08}$	
Ar ⁺⁺	8.99, 21.82	3.57×10^{-07}	
Ar ³⁺	0.4740	7.73×10^{-07}	
Ar ⁴⁺	13.10	1.82×10^{-08}	1.15×10^{-06}
Ne ⁺	12.81	5.24×10^{-07}	
Ne ⁺⁺	15.55	4.96×10^{-05}	
Ne ³⁺	0.2422	1.41×10^{-05}	
Ne ⁴⁺	24.30	$<1.31 \times 10^{-08}$	6.42×10^{-05}
S ⁺⁺	18.71, 33.47	4.15×10^{-07}	
S ³⁺	10.51	1.53×10^{-06}	1.95×10^{-06}
O ⁺	0.7323	2.82×10^{-06}	
O ⁺⁺	0.4363, 0.4959, 0.5007	2.10×10^{-04}	
O ³⁺	25.89	3.86×10^{-05}	2.51×10^{-04}
N ⁺	0.6584	1.20×10^{-07}	
N ⁺⁺	0.1750	2.39×10^{-05}	
N ³⁺	0.1483	3.09×10^{-05}	
N ⁴⁺ ^b	0.1241	4.20×10^{-06}	5.49×10^{-05}
C ⁺	0.2326	2.09×10^{-06}	
C ⁺⁺	0.1907	1.64×10^{-04}	
C ³⁺	0.1548	1.05×10^{-04}	2.71×10^{-04}

^aAr⁺ may originate from the PDR (instead of the ionized region). However, it does not affect the total argon abundance because the upper limit is small compared to abundances of other argon ions.

^bN⁴⁺ probably originates from the star and thus it is not included in the total nitrogen abundance.

Table 2.8 Comparison of abundances in IC 2448 to other sources. Numbers below should be multiplied by 10^x where x is given in parenthesis in the left hand column to get abundances. For example, the abundance He/H in the present work is 9.4×10^{-2} .

Element	IC 2448 Abundances				Solar ^d	IC 2165 ^e
	present	TPP ^a	M ^b	KB ^c		
He(-2)	9.4	11	12	8.7	8.5	10
Ar(-6)	1.2	...	1.2	0.75	4.2	1.2
Ne(-5)	6.4	8.3	6.8	11	12	5.7
S(-6)	2.0	...	9.2	6.8	14	4.5
O(-4)	2.5	4.1	3.3	5.3	4.6	2.5
N(-5)	5.5	3.2	9.3	24	6.0	7.3
C(-4)	2.7	8.6	2.5	4.8
C+N+O(-4)	5.8	16	7.7	8.0

^aTorres-Peimbert & Peimbert (1977) from optical data.

^bMilingo et al. (2002a) from optical data.

^cKingsburgh & Barlow (1994) from UV and optical data.

^dSolar abundances from Asplund et al. (2005) and Feldman & Widing (2003) as described in Pottasch & Bernard-Salas (2006).

^eIC 2165 abundances from Pottasch et al. (2004).

O, N, and C. The helium ionic abundances are calculated using emissivities in Benjamin et al. (1999). Then we sum the ionic abundances for all expected stages of ionization of an element to determine the abundance of that element. The S^+ probably originates in the PDR because it has an IP of 10.4 eV; thus it is not included in the total sulfur abundance. The N^{4+} 1241 Å line probably originates from the star because no other ions with such large ionization potentials (IP = 77.7 eV) are observed; thus it is not included in the total nitrogen abundance.

The infrared spectrum enables us to observe lines of Ar^{4+} , Ne^+ , S^{3+} , and O^{3+} that are missing or weak in the combined optical and UV spectrum of IC 2448; and it additionally allows us to place upper limits on the amount of Ar^+ and Ne^{4+} . Observations of the S^{3+} and O^{3+} infrared lines are particularly important for determining accurate elemental abundances because those ionization stages contribute significantly to the total sulfur and oxygen elemental abundances respectively. The results for ionic and total element abundances are shown in Table 2.7. We do not need to apply an ionization correction factor (ICF) because we observe all ionization stages expected to have a significant contribution to the elemental abundances derived here.

One might expect S^{4+} to be present in the H II region because ions with higher ionization potentials are observed. However, a model of the PN Me 2-1, which has a star with similar temperature to IC 2448's central star, indicates that the S^{4+} contribution to the total sulfur abundance is $\sim 15\%$. S^{4+} is not important because photons with enough energy to ionize S^{3+} to S^{4+} are absorbed by the more abundant ions of other elements that have similar ionization potentials (R. Surendiranath, private communication). We assume that the S^{4+} contribution to the total sulfur abundance is negligible, and so we do not use an ICF for sulfur.

2.6 Discussion

In Table 2.8 we compare the abundances we derive with those from previous works. Our helium, argon and neon abundances are all close to previous results. For the remaining elements, we discuss reasons why our results differ from previous ones below. The abundances of Ar, Ne, S, and O determined in this study should be more accurate and precise than in previous studies because we have used infrared lines that are less sensitive to temperature and extinction than optical and UV lines.

The sulfur abundance determined in this study is lower than previously reported. Milingo et al. (2002a) used an ICF of 39.18 to account for unseen S^{3+} , and such a large ICF leads to a large uncertainty in their sulfur abundance result. Kingsburgh & Barlow (1994) used an ICF of 3.13 to account for unseen S^{2+} and S^{3+} . Therefore, while we report a lower sulfur abundance than previous authors, it is more accurate because we observe both S^{2+} and S^{3+} in the IR spectrum and thus we do not need to use an ICF.

The oxygen abundance derived here is somewhat lower than given in former studies. This is mainly due to our use of the O^{3+} 25.89 μm line to determine the O^{3+} abundance, because the ICFs of previous studies overestimated the amount of O^{3+} . We find that the O^{3+} abundance is only 15% of the total oxygen abundance, while ICFs used in previous studies assume that O^{3+} contributes between 42% and 57% of the total oxygen abundance.

The nitrogen and carbon abundances determined here and in previous studies are uncertain. The nitrogen abundances determined from the two optical studies have large uncertainties because the optical studies must use large ICFs (Torres-Peimbert & Peimbert (1977) use 33.9 and Milingo et al. (2002a) use 1279.69) to account for unseen N^{++} , N^{3+} , and N^{4+} . This study and that of Kingsburgh &

Barlow (1994) use UV lines for important ionization stages that dominate the element abundances of nitrogen and carbon. However, the ionic abundances determined from UV lines are very sensitive to the adopted electron temperature and extinction. For example, lowering (raising) the adopted T_e by just 1000 K leads to an increase of $\sim 70\%$ (decrease of $\sim 40\%$) in the derived nitrogen and carbon abundances. Lowering (raising) the adopted $C_{H\beta}$ by 0.10 leads to up to a $\sim 30\%$ decrease (increase) in the derived nitrogen and carbon abundances. We use a higher T_e than Kingsburgh & Barlow (1994) (we use $T_e=12700$ K and they use $T_e=11000$ K), and we use a lower extinction (we use $C_{H\beta}=0.27$ whereas they use $C_{H\beta}=0.40$). Increasing the temperature and decreasing the extinction both have the effect of lowering the abundances derived from UV lines, causing the nitrogen and carbon element abundances derived in this study to be less than those derived by Kingsburgh & Barlow (1994).

The average of the Ar, Ne, and O abundances gives a metallicity of $\sim 0.45 Z_\odot$, with an uncertainty of roughly 30%. These elements are left relatively unchanged during stellar evolution. Thus their low abundances imply that IC 2448's progenitor star formed from metal deficient material, with a metallicity closer to that of the large magellanic cloud than to that of the sun. Sulfur is also left relatively unchanged during stellar evolution. However, many PNe have low sulfur abundances compared to solar, and so the sulfur abundance is not used in the average metallicity calculation. The sulfur abundance of IC 2448 is lower than the sulfur abundances of all 26 of the PNe studied by Pottasch & Bernard-Salas (2006), which supports the idea of a subsolar composition for IC 2448's progenitor star. The abundance of helium derived here for IC 2448 is somewhat above solar, which implies that some chemical processing took place within IC 2448's progenitor star. The nitrogen and carbon abundances are more uncertain, but close to solar.

Mendez et al. (1992) use their determinations of IC 2448’s stellar gravity ($\log g = 4.8$) and effective temperature ($T_{eff} = 65000$ K) to derive the current mass of IC 2448’s star as $0.58 M_{\odot}$. This current stellar mass corresponds to an initial stellar mass of $M_i \approx 1 M_{\odot}$ at a metallicity of $Z = 0.5-1.0 Z_{\odot}$ (Vassiliadis & Wood, 1993). This low stellar mass, along with the low metallicity of IC 2448’s progenitor star, imply that the first and perhaps the third dredge-up occurred.

First dredge-up would have increased the abundances of ^4He , ^{14}N , and ^{13}C , decreased the abundance of ^{12}C , and left the ^{16}O abundance the same (Marigo et al., 2003). Second dredge-up (which increases ^4He and ^{14}N but decreases ^{12}C , ^{13}C , and ^{16}O) is only expected to occur if the initial mass of the progenitor star is between 3 and 5 M_{\odot} (Marigo et al., 2003), and so it is not expected to occur here. Third dredge-up, which significantly increases ^4He and ^{12}C and slightly increases the amounts of some other elements (Marigo et al., 2003), might have occurred. It is expected to occur in stars that have $M_i \gtrsim 1.5 M_{\odot}$ at $Z = Z_{\odot}$, but this limit is at lower masses for lower Z (Marigo et al., 1999). Third dredge-up enriches the amount of carbon relative to oxygen, and thus a C/O ratio greater than one would indicate that third dredge-up occurred (Iben & Renzini, 1983).

The C/O ratio in IC 2448 derived here is 1.1, but the carbon abundance of IC 2448 is very uncertain as discussed above. Thus we cannot determine if the C/O ratio is really greater or less than one. The IR spectrum of IC 2448 (Figure 2.1) does not show PAHs which are often observed in PNe with $\text{C/O} > 1$, nor does it show silicates which are often observed in PNe with $\text{C/O} < 1$ (Zuckerman & Aller, 1986; Bernard-Salas & Tielens, 2005). The uncertainty in our carbon abundance and the lack of PAHs and silicates in the IR spectrum do not allow us to determine if IC 2448 is carbon-rich or oxygen-rich.

The abundances of IC 2448 are close to the abundances of PN IC 2165 which

is a spherical nebula with a low mass ($\lesssim 3 M_{\odot}$) progenitor star (Pottasch et al., 2004). IC 2165 probably experienced third dredge-up (in addition to first dredge-up) because it has $C/O \sim 2$ (Pottasch et al., 2004). The elements not much affected by the various dredge-up episodes (Ar, Ne, S, and O) all have subsolar values in IC 2448 and IC 2165, which implies that the progenitor stars of these nebula were created from metal deficient gas.

The IR continuum of IC 2448 gives a cool dust temperature of ~ 100 K, supporting previous studies that show IC 2448 to be an old, evolved nebula. Additionally, IR lines that would come from the photodissociation region such as [Ar II] and [Si II] are not observed. Perhaps this indicates that most of the photodissociation region has been destroyed, which fits the picture of IC 2448 being an old PN where the ionization front has gobbled up most of the photodissociation region.

2.7 Conclusions

This is the first mid-IR spectral study of IC 2448. The abundance of helium is slightly above solar, indicating that some chemical enrichment has occurred. The high uncertainties in the nitrogen and carbon abundances (due to their reliance on abundances determined from UV lines which depend strongly on the electron temperature and to a lesser extent on the extinction) make it difficult to determine how much chemical enrichment occurred. The elements not affected much by stellar evolution (Ar, Ne, S, and O) all have subsolar values in IC 2448, indicating that the progenitor star formed out of somewhat metal deficient material. Our use of infrared ionic lines which are less sensitive to extinction and temperature, and some of which arise from ions with no observable lines in the optical or UV, leads to a more accurate determination of abundances for Ar, Ne, S, and O than previously possible. The abundances determined fit with the picture of IC 2448 having a low

mass progenitor star that underwent first and perhaps third dredge-up. The IR continuum gives a cool dust temperature of ~ 100 K, supporting previous studies that show IC 2448 to be an old, evolved nebula. Additionally, lines that would arise from the PDR are missing or weak, indicating that much of the PDR is destroyed, consistent with IC 2448 being an old PN.

This work is based in part on observations made with the *Spitzer Space Telescope*, which is operated by the Jet Propulsion Laboratory, California Institute of Technology under NASA contract 1407. Support for this work was provided by NASA through Contract Number 1257184 issued by JPL/Caltec. This work is also based in part on INES data from the IUE satellite. This research made use of the SIMBAD database, operated at CDS, Strasbourg, France. We thank R. Surendiranath for his comments on the contribution of S^{4+} to the total sulfur abundance.

CHAPTER 3
CHEMICAL ABUNDANCES AND DUST IN PLANETARY
NEBULAE IN THE GALACTIC BULGE

Paper by S. Gutenkunst, J. Bernard-Salas, S. R. Pottasch, G. C. Sloan, &
J. R. Houck, accepted for publication in *The Astrophysical Journal*

3.1 Abstract

We present mid-infrared Spitzer spectra of eleven planetary nebulae in the Galactic Bulge. We derive argon, neon, sulfur, and oxygen abundances for them using mainly infrared line fluxes combined with some optical line fluxes from the literature. Due to the high extinction toward the Bulge, the infrared spectra allow us to determine abundances for certain elements more accurately than previously possible with optical data alone. Abundances of argon and sulfur (and in most cases neon and oxygen) in planetary nebulae in the Bulge give the abundances of the interstellar medium at the time their progenitor stars formed; thus these abundances give information about the formation and evolution of the Bulge. The abundances of Bulge planetary nebulae tend to be slightly higher than those in the Disk on average, but they do not follow the trend of the Disk planetary nebulae, thus confirming the difference between Bulge and Disk evolution. Additionally, the Bulge planetary nebulae show peculiar dust properties compared to the Disk nebulae. Oxygen-rich dust features (crystalline silicates) dominate the spectra of all of the Bulge planetary nebulae; such features are more scarce in Disk nebulae. Additionally, carbon-rich dust features (polycyclic aromatic hydrocarbons) appear in roughly half of the Bulge planetary nebulae in our sample, which is interesting in light of the fact that this dual chemistry is comparatively rare in the Milky Way as a whole.

3.2 Introduction

Abundances of planetary nebulae (PNe) have long been used to aid in the understanding of the chemical history of the Milky Way. Certain elements such as argon and sulfur (and neon as long as the initial mass is not near $3 M_{\odot}$ and oxygen if initial mass of the progenitor star is $\lesssim 5M_{\odot}$, Karakas & Lattanzio 2003; Karakas 2003) are not changed in the course of the evolution of the low and intermediate mass precursor stars of PNe. Thus the abundances of these elements give the chemical composition of the cloud from which the PNe progenitor stars formed. Many abundance studies have been made of PNe (as well as stars and H II regions) in the Galactic Disk, leading to the determination of abundance gradients across the Disk (e.g. Shaver et al., 1983; Rolleston et al., 2000; Pottasch & Bernard-Salas, 2006). However, due to the high extinction toward the Bulge, there is a relative paucity of abundance studies of PNe as well as stars and H II regions in the Bulge.

Galactic bulges and spheroids may contain half of the stars in the local universe (Ferreiras et al., 2003). Thus, understanding their chemical evolution and formation is important to a general theory of galaxy formation. Insights into our own Galactic Bulge formation have implications for bulge formation in general.

Abundances of Galactic Bulge planetary nebulae (GBPNe) have the potential to answer questions about how the Bulge formed. For example, what type of collapse formed the Bulge (dissipational or dissipationless)? And, has secular evolution within the Galaxy since Bulge formation caused a significant amount of star formation within the Bulge (Minniti et al., 1995)? At a bare minimum, a difference between abundance gradients of PNe in the Bulge and Disk would imply that they formed in separate processes.

The large extinction toward the GBPNe makes infrared (IR) lines preferable to optical lines for determining their abundances. Additionally, infrared lines provide

essential data on important ionization stages of argon, neon, and sulfur as well as O IV for oxygen. We complement the IR data with optical data where necessary, so that we need no or only small ionization correction factors (ICFs) to account for unobserved stages of ionization. Finally, abundances derived from IR lines depend only weakly on the electron temperature (Rubin et al., 1988; Pottasch & Beintema, 1999). All of these factors lead to more accurately determined abundances than previously possible with optical lines alone. Likewise, IR spectra are well suited to study the various dust features of GBPNe because signatures of both oxygen-rich dust (in the form of crystalline silicates) and carbon-rich dust (in the form of polycyclic aromatic hydrocarbons; PAHs) can be observed if they are present.

Abundances for a number of Galactic Disk planetary nebulae (GDPNe) were determined with the use of spectra taken with the *Infrared Space Observatory* (*ISO*; e.g. Pottasch & Bernard-Salas, 2006). However, *ISO* lacked the sensitivity to study PNe further than 3–4 kpc away from the Sun. As a result, *ISO* only studied two Bulge PNe, M1-42 and M2-36. Due to the better sensitivity of the Infrared Spectrograph (IRS; Houck et al., 2004) on the *Spitzer Space Telescope* (Werner et al., 2004) we are able to obtain spectra of GBPNe closer to the Galactic Center; the furthest GBPN in our sample is about 10 kpc from the Sun.

In this paper we present *Spitzer* IRS spectra of eleven GBPNe. The next section describes the *Spitzer* data, while §3.4 describes the supplementary data we use. In §3.5 we describe the data analysis, deriving ionic and total abundances of argon, neon, sulfur, and oxygen. Additionally we identify the crystalline silicate features and measure PAH fluxes. Finally we discuss what our results imply for the evolution of the Galactic Bulge and its PNe in §3.6 and conclude in §3.7.

3.3 Spitzer IRS Data

3.3.1 Observations

We observed eleven GBPNe with the *Spitzer* IRS between September 2006 and September 2007 as part of the Guaranteed Time Observation program 30550. In order to minimize slit losses, PeakUp with 0.4'' positional accuracy was performed for the six PNe where it was possible, while blind pointing with $\sim 1''$ positional accuracy was done for the remaining five PNe. We observed these PNe with the IRS Short-Low (SL), Short-High (SH), and Long-High (LH) modules, covering the wavelength range from 5 to 40 μm . In order to subtract the background and minimize the effect of rogue pixels, we took off-source observations for SH and LH; for the SL module we subtracted the background by differencing the orders. The data were taken in staring mode so that spectra were obtained at two nod positions along each IRS slit. For SH and LH, a short exposure time of six seconds was used to keep the bright lines from saturating, with a total of four cycles for redundancy and to aid in the removal of cosmic rays; for the SL module, data were taken in three cycles of fourteen seconds each. Table 3.1 gives the object names, their Astronomical Observation Request (AOR) keys and coordinates.

3.3.2 Source Selection

The sources were selected to ensure they belong to the Bulge according to the following criteria. (1) Foremost, the best criterion for ensuring Bulge membership is having galactic coordinates $|\ell| < 10^\circ$ and $|b| < 10^\circ$ (Pottasch & Beintema, 1999). All of the sources were selected to meet this criterion. (2) We selected objects with high radial velocities, except for two objects, PNG001.6-01.3 and PNG002.1+03.3, where they are unknown and whose IRAS fluxes and positions indicate that they

are members of the Bulge, (Acker et al., 1992). (3) Finally, the objects have diameters $\lesssim 5''$. Pottasch & Beintema (1999) consider all PNe with diameters $> 12''$ to be foreground objects, and thus choosing small diameters helped to ensure Bulge membership. Table 3.2 gives the radial velocities and diameters of our GBPNe.

Additionally, in order to make certain that we could get good *Spitzer* IRS spectra of the GBPNe, we chose isolated objects in the IRAS Point Source Catalog (PSC) with small radial extent, accurate coordinates, and observable intensities. While the IRAS PSC is not as sensitive as our *Spitzer* observations (the IRAS PSC catalog is sensitive to a couple hundred mJy whereas our *Spitzer* observations are sensitive to a few mJy), we check that only one source is on the slit during the data reduction. The criterion of selecting PNe with small sizes also ensured that nearly all of the flux from most of the PNe could be observed within SL, the smallest IRS slit at $3.6''$ across. The sources also were chosen to have coordinates known to better than $1.4''$ from the radio positions of Condon & Kaplan (1998), and these coordinates were refined with the 2MASS catalog. Finally, we chose objects with radio fluxes at 21 cm (F_{21cm}) that implied IR fluxes bright enough ($F_{21cm} > 10$ mJy) to allow for short integration times, but dim enough ($F_{21cm} < 50$ mJy) to not saturate any of the IRS modules. Table 3.2 gives the IRAS fluxes at 12 and $25 \mu\text{m}$ as well as the radio fluxes at 21 cm for our objects.

Table 3.1 Positions and AORkeys for observed GBPNe

PNG	On Position ^a			Off Position	
	Number	AORkey	RA		DEC
	000.7+03.2	17646848	17 34 54.71	-26 35 56.9	17650176
	000.7+04.7	17647616	17 29 25.97	-25 49 07.1	17650432
	001.2+02.1	17648896	17 40 12.84	-26 44 21.9	17650688
	001.4+05.3	17647872	17 28 37.63	-24 51 07.2	17650944
	001.6-01.3	17649152	17 54 34.94	-28 12 43.3	17651200
	002.1+03.3	17649408	17 37 51.14	-25 20 45.2	17651456
	002.8+01.7	17649664	17 45 39.81	-25 40 00.6	17651712
	006.0-03.6	17648128	18 13 16.05	-25 30 05.3	17651968
	351.2+05.2	17648384	17 02 19.07	-33 10 05.0	17652224
	354.2+04.3	17648640	17 14 07.02	-31 19 42.6	17652480
	358.9+03.2	17647104	17 30 43.82	-28 04 06.8	17652736

^aRA and DEC are in J2000.0. RA is in hours, minutes, seconds; DEC is in degrees, arcmin, arcsec.

Table 3.2 Properties of observed GBPNes

PNG	$\log(F_{H\beta})^a$	$R_{\odot,PN}^b$	R_{GC}^c	V_{rad}^d	Diam ^a	IRAS Fluxes (Jy) ^e	F_{6cm}^a	F_{21cm}^f
Number	(erg cm ⁻² s ⁻¹)	(kpc)	(kpc)	(km s ⁻¹)	($''$)	$F_{12\mu m}$	(mJy)	(mJy)
000.7+03.2	-13.40 ± 0.20	7.01	1.0±2.9	-175	5.2	<2.01	15	15.6
000.7+04.7	-13.90 ± 0.30	...	<4	+40	2.7	0.50	27.7	12.8
001.2+02.1	-13.73 ± 0.10	6.64	1.4±2.8	-172	4.0	2.19	26	24.2
001.4+05.3	-12.70 ± 0.30	7.90	0.2±1.9	+42	5.0	<0.28	13	13.8
001.6-01.3	-13.90 ± 0.30	...	<4	...	4.5	<3.41	...	19.7
002.1+03.3	<4	...	4.8	<1.93	5	46.0
002.8+01.7	-13.48 ± 0.10	7.50	0.6±2.5	+164	3.8	13.8
006.0-03.6	-12.11 ± 0.02	4.91	3.2±2.1	+136	5.1	<1.45	51	41.2
351.2+05.2	-12.10 ± 0.10	7.69	1.2±1.2	-128	5.0	0.55	12	14.4
354.2+04.3	-12.62 ± 0.10	10.71	2.8±4.0	-75	4.0	<0.34	9.1	11.6
358.9+03.2	-13.03 ± 0.10	5.12	2.9±2.2	+190	4.0	<2.70	32	27.3

^aFrom the Strasbourg-ESO Catalogue of Galactic Planetary Nebula (Acker et al., 1992). The diameter quoted here is the larger of the optical and radio diameters given in the catalogue.

^bHeliocentric distance, $R_{\odot,PN}$, from Zhang (1995).

^cGalactocentric distance, R_{GC} , calculated assuming that the Sun is at 8.0 kpc from the Galactic Center. If $R_{\odot,PN}$ is unknown, then the PN is assumed to lie within 4 kpc of the Galactic Center.

^dFrom Durand et al. (1998) and Beaulieu et al. (1999).

^eFrom the IRAS catalogue of Point Sources, Version 2.0, Helou et al. (1988).

^fFrom Condon & Kaplan (1998).

3.3.3 Data Reduction

We start with basic calibrated data (bcd) from the *Spitzer Science Center's* pipeline version s15.3 or s16.1, and run it through the IRSCLEAN¹ program to remove rogue pixels, which uses a mask of rogue pixels from the same campaign as the data. Then we take the mean of repeated observations (cycles) to improve the signal to noise ratio. After that the background is subtracted using the off-source positions for SH and LH, and using the off-order for SL (for example, SL1 nod1 - SL2 nod1). Next we use SMART (Higdon et al., 2004) to manually extract the images, using full-slit extraction for SH and LH and variable-column extraction for SL; we also inspect the spectral profiles of each target with the Manual Source Finder tool in SMART to ensure that only one source is within the slit. Spikes due to deviant pixels which the IRSCLEAN program missed are removed manually in SMART. In order to account for flux that fell outside of the IRS slits (due either to a slight mispointing and/or the extended size of the GBPNe), we apply multiplicative scaling factors to each order and nod. The highest flux in LH sets the scaling because LH is large enough to contain the entire flux of all of our GBPNe. Thus, one nod in LH is scaled to the other, the SH nods are then scaled to LH, and the SL nods and orders are then scaled to match SH. Table 3.3 gives the scaling factors; they are usually quite small (≤ 1.20) except for three PNe where the scaling factors in SL (the aperture with the smallest width) reach up to 1.70. Figure 3.1 plots the scaled and nod-averaged spectra. We predict the 12 and 25 μm IRAS fluxes from these scaled IRS spectra and find generally good agreement with the actual IRAS fluxes, confirming that only the IRAS source is within the IRS slit. Finally we use the gaussian profile fitting routine in SMART to measure line fluxes for each nod position of the scaled spectra. Table 3.4 gives the observed

¹The IRSCLEAN program is available from the *Spitzer Science Center's* website at <http://ssc.spitzer.caltech.edu>

nod-averaged line fluxes. Uncertainties on the line fluxes are usually $\leq 10\%$, with uncertainties greater than this marked in the table. A less-than sign in Table 3.4 indicates a 3σ upper limit obtained from the instrument resolution and the root mean square (RMS) deviation in the spectrum at the wavelength of the line.

3.4 Supplementary Data

We supplement our IR data with optical and radio data from the literature to aid abundance determinations for three reasons. First, we use the observed $H\beta$ and 6 cm radio fluxes to derive the extinction toward GBPNe. Table 3.2 gives these fluxes from the Strasbourg-ESO Catalogue of Galactic Planetary Nebula (Acker et al., 1992). Second, we adopt electron temperatures derived from ratios of optical line fluxes (discussed in §3.5.1). Third, we use optical line fluxes for ions not observable in our IR spectra (specifically lines fluxes of Ar IV, S II, O II, and O III) to reduce the need for ICFs. (As an aside, no UV line data for any of the GBPNe in our sample are available due to the large extinction toward the Bulge.) When the optical line fluxes are given as observed line fluxes, we apply the logarithmic extinction at $H\beta$ ($C_{H\beta}$) given in the paper to correct the lines for extinction because it gives the correct Balmer decrement. When more than one paper gives a value for a line flux, we take the average (after correcting all line fluxes for extinction), and Table 3.5 gives the optical extinction corrected line fluxes adopted for the calculation of abundances.

All of the PNe in this sample should be within ~ 4 kpc or less of the Galactic Center because they were selected to be members of the Bulge. In order to determine approximately where they are within the Bulge to place them on a plot of abundance versus galactocentric distance, we adopt the heliocentric statistical distances from Zhang (1995). We chose these distances because Zhang (1995) lists

distances to more of our objects than other studies, such as van de Steene & Zijlstra (1995) and Cahn et al. (1992). An accurate statistical distance scale for PNe is difficult to obtain, and controversies exist as to which statistical distance scales are the best: for example Bensby & Lundström (2001) find that Zhang’s distance scale is good, while Ciardullo et al. (1999) find that it is not as good. However, regardless of which statistical distances we adopt, the conclusions of the paper will remain unchanged because all of the PNe in our sample are constrained to be in the Bulge by other criteria and we include the large uncertainties that go with these statistical distances in the data analysis.

We adopt the distance from the Sun to the Galactic Center, R_o , from Reid (1993) who determines the best estimate of this distance by taking a weighted average of the various determinations of R_o from different methods. Reid (1993) finds that $R_o = 8.0 \pm 0.5$ kpc, and this value seems to agree with more current estimates of this distance (e.g. López-Corredoira et al., 2000; Eisenhauer et al., 2005; Groenewegen et al., 2008). Galactocentric distances (R_{GC}) are then calculated assuming this R_o , and uncertainties on R_{GC} are calculated using standard error propagation and assuming an uncertainty of 40% on the heliocentric distance (Zhang 1995 estimates the accuracy of the PN distance scale as 35-50% on average). If the distance to a PN is unknown, we assume it is within 4 kpc of the Galactic Center. Table 3.2 lists the heliocentric and galactocentric distances for each object.

Table 3.3 Multiplicative scaling factors for GBPNe spectra. LHn1 stands for LH nod 1, SL1n2 stands for SL order 1 nod 2, etc.

PNG Number	LHn1	LHn2	SHn1	SHn2	SL1n1	SL1n2	SL3n1	SL3n2	SL2n1	SL2n2
000.7+03.2	1.00	1.00	1.00	1.00	1.00	1.00	1.00	1.00	1.00	1.00
000.7+04.7	1.02	1.00	1.00	1.00	1.00	1.00	1.00	1.00	1.00	1.00
001.2+02.1	1.02	1.00	1.00	1.05	1.00	1.00	1.00	1.00	1.00	1.00
001.4+05.3	1.03	1.00	1.15	1.17	1.15	1.15	1.00	1.15	1.00	1.00
001.6-01.3	1.05	1.00	1.15	1.15	1.15	1.15	1.50	1.50	1.50	1.50
002.1+03.3	1.00	1.00	1.20	1.20	1.20	1.20	1.20	1.20	1.20	1.20
002.8+01.7	1.01	1.00	1.05	1.10	1.10	1.10	1.10	1.15	1.10	1.10
006.0-03.6	1.02	1.00	1.15	1.15	1.15	1.15	1.60	1.70	1.50	1.40
351.2+05.2	1.02	1.00	1.15	1.15	1.50	1.50	1.50	1.40	1.50	1.40
354.2+04.3	1.02	1.00	1.15	1.15	1.20	1.20	1.20	1.20	1.20	1.20
358.9+03.2	1.02	1.00	1.12	1.10	1.15	1.15	1.00	1.20	1.00	1.00

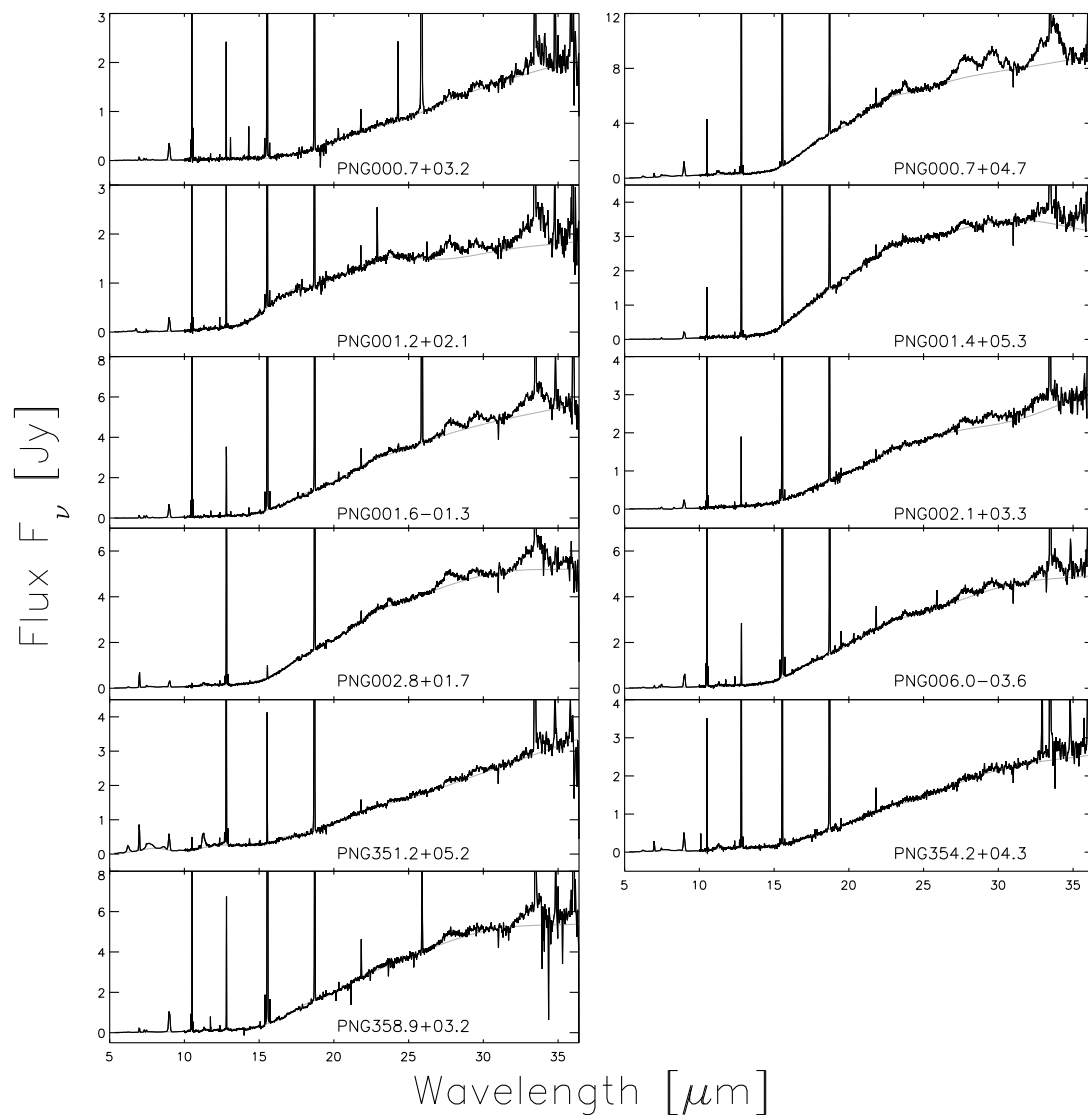


Figure 3.1 Scaled, nod-averaged *Spitzer* IRS spectra (black) of our GBPNe. SL data is presented below $10 \mu\text{m}$, and HR data above $10 \mu\text{m}$. The spline-fits to the continua (which we subtract from the spectra later in order to better view the crystalline silicate features) is over-plotted (grey).

Table 3.4 Observed infrared line fluxes. The H I lines at 7.46 μm and 12.37 μm both have contributions from more than one H I line, as discussed in §3.5.1. All line fluxes are from HR spectra except the lines with $\lambda < 10 \mu\text{m}$ which are from SL. A less-than sign indicates a three sigma upper limit. All line flux uncertainties are $\leq 10\%$ unless otherwise indicated.

Line	λ μm	Observed line fluxes for each object labeled by PNG number ($10^{-14} \text{ erg cm}^{-2} \text{ s}^{-1}$)														
		000.7+03.2	000.7+04.7	001.2+02.1	001.4+05.3	001.6-01.3	002.1+03.3	002.8+01.7	006.0-03.6	351.2+05.2	354.2+04.3	358.9+03.2				
[Ar II]	6.99	26.15	111.62	<8.53	6.63 ^a	51.51 ^a	<4.80	253.42	35.44 ^a	304.57	92.77	85.93				
H I(6-5)+	7.46	13.47	36.22 ^a	22.15	19.40	49.27	18.57 ^b	31.19 ^a	61.70	28.02 ^a	19.67	38.81				
[Ar V]	7.90	8.82 ^a	<13.74	<2.95	<2.26	<12.65	<5.38	<7.96	<10.93	<14.98	<8.17	<9.49				
[Ar III]	8.99	162.55	397.33	124.24	90.22	278.81	100.22	108.59	260.64	173.77	192.54	472.17				
[S IV]	10.52	1401.40	186.81 ^a	573.91	67.45	1882.50	688.40	10.42 ^b	2179.00	19.77	182.90	1593.55 ^a				
H I(7-6)+	12.37	5.35 ^a	14.18 ^a	10.53 ^a	6.70 ^a	9.37 ^a	7.37 ^b	11.16 ^a	17.13	8.10 ^a	7.58 ^b	11.89 ^a				
[Ne II]	12.82	88.21	1414.80	133.51	408.05	142.14	72.09	1188.85	106.01	1132.05	687.65	228.45				
[Ar V]	13.10	14.98 ^a	<3.69	<3.30	<5.12	9.25	<4.47	<4.73	<4.35	<3.90	<4.25	<3.75				
[Ne V]	14.32	22.06	<3.09	<2.40	<2.61	11.74	<2.63	<3.63	<2.85	<4.62	<3.51	<3.52				
[Ne III]	15.56	1590.25	1466.85	1500.55	333.59	3669.75	1313.55	17.82	3455.80	126.08	676.02	5245.25				
[S III]	18.73	419.10	503.54	344.60	333.46	737.29	255.92	601.26	669.36	795.01	600.36	866.11				
[Ar III]	21.84	11.03 ^a	22.48	8.10	7.01 ^a	22.43 ^b	5.91 ^b	12.44 ^b	20.29 ^c	9.27 ^a	11.78	34.77				
[Ne V]	24.30	30.29	<8.73	<2.71	<3.18	8.63 ^b	<2.40	<4.78	<4.50	<2.55	<3.06	<8.33				
[O IV]	25.91	3580.55 ^a	<8.83	<2.63	<3.83	1313.85	<2.42	<4.52	16.94 ^a	<3.33	<2.85	101.99				
[S III]	33.50	344.92	110.49	190.76	164.33	264.60	158.36	227.22	214.29	499.02	417.67	267.07				
[Ne III]	36.03	181.76	121.71	150.23	<36.43	350.23	110.85	<25.80	283.73	<29.97	70.92 ^a	401.05				

^aUncertainty between 10 and 20%.

^bUncertainty between 20 and 50%.

^cUncertainty between 50 and 100%.

Table 3.5 Extinction corrected optical line fluxes. No optical line fluxes for PNG002.1+03.3 were found in the literature. References: Acker et al. (1991), Ratag et al. (1997), Cuisinier et al. (2000), Escudero et al. (2004), and Wang & Liu (2007).

Line	λ Å	Extinction corrected line fluxes relative to $H\beta=100$ for each object labeled by PNG number											
		000.7+03.2	000.7+04.7	001.2+02.1	001.4+05.3	001.6-01.3	002.8+01.7	006.0-03.6	351.2+05.2	354.2+04.3	358.9+03.2
[O II]	3727	114.0	55.13	59.60	130.0	
[Ne III]	3869	69.6	...	32.86	95.19	...	9.70	
[O III]	4363	12.4	2.81	6.68	
[Ar IV]+He I	4712	7.00	1.91	
[Ar IV]	4740	4.61	1.93	
[O III]	4959	279.1	123.99	231.9	118.2	354.2	...	369.54	7.27	46.41	...	339.1	
[O III]	5007	790.4	360.37	728.0	304.7	1003.8	22.65	1067.55	25.89	136.5	...	989.4	
[S III]	6312	1.86	1.37	1.34	0.71	2.08	...	1.01	...	2.02	
[S II]	6717	13.35	2.76	2.77	2.70	6.40	4.77	4.35	6.46	5.96	...	6.68	
[S II]	6731	19.47	5.12	4.37	3.30	14.38	9.06	7.83	9.31	9.36	...	12.41	
[Ar V]	7005	0.67	
[Ar III]	7135	30.79	29.22	15.79	12.24	21.54	6.56	16.15	4.86	9.34	...	30.66	
[Ar IV]	7236	...	0.96	
[Ar IV]	7264	...	1.06	
[O II]	7325	5.15	11.42	7.10	8.33	...	3.87	6.29	0.91	2.07	...	7.73	

3.5 Data Analysis

3.5.1 Abundances

Before determining abundances for this sample of GBPNe, we must first calculate and then correct for extinction. Additionally we adopt electron temperatures (T_e) from the literature and then employ infrared line ratios to derive the electron densities (N_e). After that we use the values of the above quantities to obtain abundances for each ion. The following subsection discuss the details of the calculations of extinction, the selection of T_e and N_e , and finally the derivation of ionic and total abundances.

Extinction Correction

We first calculate the reddening correction by comparing the $H\beta$ flux predicted from IR hydrogen recombination lines to the observed $H\beta$ flux (see Table 3.6). In order to predict the $H\beta$ flux from the IR H I lines, we adopt the theoretical ratios of hydrogen recombination lines from Hummer & Storey (1987) and assume case B recombination for a gas at $T_e = 10^4$ K and $N_e = 10^3$ cm $^{-3}$. The H I(7-6) line at 12.37 μ m and the H I(11-8) line at 12.39 μ m are blended in the SH spectrum, and theoretically the H I(7-6) line contributes 89% of total line flux. Similarly, nearby lines of H I(6-5), H I(17-8), H I(8-6), and H I(11-7) contribute to the H I line at 7.46 μ m, with the H I(6-5) flux theoretically contributing 74% of the total line flux. The contributions of additional lines are removed before calculating the predicted $H\beta$ flux from the H I(7-6) and H I(6-5) IR lines.

Additionally we calculate extinction by comparing the $H\beta$ flux predicted from the radio flux at 6cm to the observed $H\beta$ flux. We assume that $T_e = 10^4$ K (and thus $t \equiv T_e/10^4$ K = 1), $\text{He}^+/\text{H}^+ = 0.09$, and $\text{He}^{++}/\text{H}^+ = 0.03$ and use the following

formula from Pottasch (1984):

$$F(H\beta)_{6cm}^{predicted} = \frac{S_{6cm}}{2.82 \times 10^9 t^{0.53} (1 + He^+/H^+ + 3.7He^{++}/H^+)}$$

where 2.82×10^9 converts units so that S_{6cm} is in Jy and $F(H\beta)$ is in $\text{erg cm}^{-2} \text{ s}^{-1}$. Table 3.2 gives the values for S_{6cm} and $F(H\beta)$ while Table 3.6 gives the calculated values of the extinction.

For the abundance calculations, in order to weight the extinctions calculated from both of the above methods equally, we use

$$C_{H\beta,final} = \frac{C_{H\beta,HI(7-6)}}{4} + \frac{C_{H\beta,HI(6-5)}}{4} + \frac{C_{H\beta,radio}}{2}$$

when we have extinctions from both H I lines and the radio, otherwise we just take an average (see Table 3.8 for these adopted values). There is no $H\beta$ flux available for PNG002.1+03.3 and thus we adopt an extinction to it from the average of the other GBPNe extinctions. Table 3.6 gives the extinction values derived here along with those from the literature. In general there is very good agreement between the different methods.

We use the extinction law from Fluks et al. (1994) and assume the standard R_V of the Milky Way of 3.1. However, there is evidence that interstellar extinction is steeper than this toward the Bulge, e.g. Walton et al. (1993b) find that $R_V=2.3$ and Ruffle et al. (2004) find $R_V = 2.0$. Nevertheless, abundances determined from IR lines are not greatly affected by this change in R_V : an $R_V=2.0$ usually changes their abundances by $\lesssim 5\%$ (and at most 10%) compared to the usual $R_V=3.1$. Thus, because the previous optical studies to which we compare assumed $R_V=3.1$, and because the IR lines are even less affected by the choice of R_V , we assume $R_V=3.1$.

Table 3.6 Comparison of the derived $C_{H\beta}$ with the literature. References: ARKS91 = Acker et al. (1991), RPD97 = Ratag et al. (1997), CMKAS00 = Cuisinier et al. (2000), ECM04 = Escudero et al. (2004), WL07 = Wang & Liu (2007), and TASK92 = Tylenda et al. (1992).

PNG	This work ^a		ARKS91		RPDM97		CMKAS00		ECM04		WL07		TASK92	
	Number	$\overline{H\text{I}(7-6)}$	$\overline{H\text{I}(6-5)}$	6 cm	Balmer	Balmer	6 cm	Balmer	Balmer	$\overline{H\alpha/H\beta}$	$\overline{H\alpha/H\beta}$	6 cm	Balmer	6 cm
000.7+03.2	2.10	2.00	2.05	2.17	2.35	2.26	2.11	2.2	2.0
000.7+04.7	3.02	2.93	2.81	3.33	2.88	3.3	2.8
001.2+02.1	2.72	2.55	2.62	2.71	2.40	2.7	2.6
001.4+05.3	1.50	1.46	1.28	1.25	1.45	1.36	1.3
001.6-01.3	2.84	3.06	...	3.35	3.4:	...
002.1+03.3
002.8+01.7	2.50	2.45	...	3.07	3.1	...
006.0-03.6	1.31	1.37	1.29	...	1.43	1.35	1.41	1.18	1.30	1.32	1.30	1.32
351.2+05.2	0.98	1.02	0.65	1.11	0.985	0.735	1.14	0.68
354.2+04.3	1.47	1.39	1.05	1.69	1.78	1.67	1.08
358.9+03.2	2.08	2.09	2.01	2.22	2.23	2.15	2.29	2.2	2.04

^aSee §3.5.1.

Electron Temperature and Density

In order to derive abundances, we adopt two electron temperatures (T_e): $T[\text{N II}]$ for the low-ionization potential ions (Ar II, Ne II, S II, and O II), and $T[\text{O III}]$ for the high-ionization potential ions. Table 3.7 gives the electron temperatures from the literature. When possible, our adopted $T[\text{N II}]$ and $T[\text{O III}]$ are an average of the values from the literature. If temperatures are not available in the literature, we assume the average value from the other GBPNe in the sample ($\langle T[\text{N II}] \rangle = 8100$ K and $\langle T[\text{O III}] \rangle = 10700$ K). Abundances from IR lines depend only weakly on the adopted T_e , and thus our assumption does not strongly affect our abundances — especially those of argon, neon, and sulfur which are mostly determined from IR lines.

We determine electron densities (N_e) from IR line ratios of S III, Ne III, Ar III, Ar V, and Ne V (see Table 3.7). The S III line ratio gives the best estimate of N_e , and thus we adopt it for the abundance analysis. Densities determined from the other line ratios are more uncertain because they either rely on at least one line with a weak flux, or the density is outside the range of what the line ratio can accurately measure. The adopted N_e from the S III ratios have an average of 3500 cm^{-3} , and range from 1000 to 9200 cm^{-3} .

Ionic and Total Abundances

Table 3.8 lists the parameters used in determining the PNe ionic abundances. Note that we use a predicted $H\beta$ flux from the IR H I lines in order to ensure that the hydrogen comes from within the same slit as the IR forbidden lines. Table 3.9 presents the ionic abundances themselves. In order to determine total elemental abundances, the ionic abundances for each element are summed. When the ionic abundance can be determined by more than one line, we choose the abundance(s)

from the most reliable line(s), and mark the lines used in Table 3.9. If necessary, the sum of the ionic abundances for each element is then multiplied by an ionization correction factor (ICF) to account for unobserved ions that are expected to be present. For argon, we apply an ICF for the nine objects for which Ar^{+3} is not observed. For neon, we apply an ICF for the four high ionization nebulae with unobserved Ne^{+3} . ICFs are generally small, and we can derive accurate total elemental abundances for many objects, especially for the elements of neon and sulfur whose abundances are derived mainly from IR lines and which rarely need ICFs. Table 3.10 presents the total elemental abundances.

The Ar^{+3} abundance can only be determined directly from optical lines for two of the GBPNe (PNG000.7+03.2 and PNG006.0-03.6). However, the Ar^{+3} abundance cannot contribute a large amount because the abundance of Ar^{+4} always accounts for $<2\%$ of the total argon abundance. We adopt an ICF to account for unobserved Ar^{+3} determined by $\text{Ar}^{+3} = 0.28 * \text{Ar}^{+2}$ because the two GBPNe with observed Ar^{+3} have $\text{Ar}^{+3}/\text{Ar}^{+2} = 0.27$ and 0.29 . Additionally, the GDPNe in the sample of Pottasch & Bernard-Salas (2006) for which the ionic abundance of Ar^{+4} is less than 2% of the total argon abundance (like our sample of GBPNe) have $\text{Ar}^{+3}/\text{Ar}^{+2}$ ranging from 0.15 to 0.68 with a mean of 0.30 , so our assumption of $\text{Ar}^{+3} = 0.28 * \text{Ar}^{+2}$ is justified.

The Ne^{+3} abundance cannot be determined directly for any of our GBPNe because its lines lie in the UV. However, it is only expected to contribute significantly if the O^{+3} line is detected in the IRS spectrum because its ionization potential (IP= 63.45 eV) is near that of O^{+3} (IP = 54.93 eV). The O^{+3} line is detected in only four of the spectra of our GBPNe (PNG000.7+03.2, PNG001.6-01.3, PNG006.0-03.6, and PNG358.9+03.2). Thus, for these four objects only, an ICF is necessary to account for unobserved Ne^{+3} . Similarly to Ar^{+3} , the Ne^{+3} cannot

contribute a huge amount because the abundance of Ne^{+4} always accounts for $<1\%$ of the total abundance of neon. Taking the average of a sample of Galactic PNe, Bernard-Salas et al. (2008) find that $\text{Ne}^{+3} = 0.35 * (\text{Ne}^{+2} + \text{Ne}^{+4})$, and thus we adopt an ICF determined by this to account for unobserved Ne^{+3} .

The uncertainties in the derived elemental abundances result from uncertainties in the line fluxes, $C_{H\beta}$, T_e , N_e and ICFs. The measured H I line fluxes typically have uncertainties $\lesssim 20\%$, while the measured fine structure line fluxes usually have uncertainties $\lesssim 10\%$. Uncertainties are also introduced into the line fluxes from the adopted scaling factors which are typically $\lesssim 15\%$ for the high resolution lines (those lines above $10 \mu\text{m}$), but reach 50–70% for the low resolution lines for three objects. However, our scaling factors cannot be far off because the $C_{H\beta}$ determined from H I lines in in the high and low resolution spectra agree well and the ionic Ar^{+2} abundance determined from Ar III lines in the high and low resolution spectra also agree well, even for the nebulae with the largest scaling factors. The uncertainties in $C_{H\beta}$ and T_e of $\sim 10\%$ each do not have a large affect on the total elemental abundances of argon, neon, and sulfur because these abundances are determined mainly from IR lines; however, they will have a larger affect on the total abundance of oxygen. The uncertainty on N_e is $\sim 30\%$. The uncertainties on the ICFs for argon and neon are most likely less than a factor of two, causing an abundance uncertainty for these elements of $\lesssim 30\%$ due to the ICFs (when the ICFs are necessary). A comparison to optically derived abundances for the same objects by various authors gives an estimate of the typical total abundance uncertainty of $\sim 50\%$ (this work, Górný et al., 2004; Bernard-Salas et al., 2008).

Table 3.7 Electron temperatures and densities. Electron temperatures were taken from the literature, with references given by the table notes. We derive electron densities from IR line ratios; ‘low’ indicates that the density is lower than the theoretical ratio can measure.

PNG Number	Temperature T_e (K)		Density N_e (cm^{-3})				
	[O III]	[N II]	[S III]	[Ne III]	[Ar III]	[Ar V]	[Ne V]
000.7+03.2	10200 ^b , 13300 ^e	8000 ^c , 8400 ^e	1000 ^g	low	120 ^g	370 ^g	low
000.7+04.7	10200 ^d , 10200 ^b	8500 ^d	9200	3100 ^g	10000
001.2+02.1	10200 ^b	...	2100 ^g	low	2000 ^g
001.4+05.3	10200 ^b	8300 ^c	2500 ^g	...	low
001.6-01.3	4700	low	500 ^g	...	3000 ^g
002.1+03.3	1700 ^g	2200 ^g	7500
002.8+01.7	10200 ^b	...	3900	...	low
006.0-03.6	9800 ^e , 9840 ^f	9300 ^e , 11370 ^f	5000	3600 ^g	low
351.2+05.2	10200 ^b , 9300 ^e	7000 ^e , 6000 ^a	1700 ^g	...	14000
354.2+04.3	10200 ^b	6600 ^e , 6400 ^a	1400 ^g	low	5400 ^g
358.9+03.2	10200 ^b , 7700 ^e , 10400 ^a	8300 ^e , 8200 ^a , 8900 ^e	5300	7700	low

^aAcker et al. (1991)

^bCahn et al. (1992)

^cCuisinier et al. (2000)

^dEscudero et al. (2004)

^eRatag et al. (1997)

^fWang & Liu (2007)

^gThe measured line ratio is at the low end (in the non-linear regime) of the densities that the theoretical line ratio can measure.

Table 3.8 Adopted parameters for determining abundances

PNG Number	$F_{H\beta, predicted}$ (10^{-14} erg cm $^{-2}$ s $^{-1}$)	$C_{H\beta}$	N_e (cm $^{-3}$)	T[O III] (K)	T[N II] (K)
000.7+03.2	483	2.05	1000	11800	8200
000.7+04.7	1328	2.89	9200	10200	8500
001.2+02.1	902	2.62	2100	10200	8100 ^b
001.4+05.3	630	1.38	2500	10200	8300
001.6-01.3	1280	2.95	4700	10700 ^b	8100 ^b
002.1+03.3	662 ^a	1.87 ^a	1700	10700 ^b	8100 ^b
002.8+01.7	1071	2.47	3900	10200	8100 ^b
006.0-03.6	1791	1.32	5000	9800	10300
351.2+05.2	816	0.82	1700	9800	6500
354.2+04.3	674	1.23	1400	10200	6500
358.9+03.2	1211	2.04	5300	14200	8500

^aNo extinction nor H β flux is given in literature for PNG002.1+03.3, so we cannot calculate the extinction from our data. We use the average extinction of the other GBPNe ($C_{H\beta} = 1.87$) for the extinction toward PNG002.1+03.3.

^bWhen we could not find T[O III] or T[N II] in the literature, we adopted the average value from the other GBPNe in this sample.

Table 3.9 Ionic abundances

Ion	x ^a	λ	Ionic abundances for each object labeled by PNG number														
			000.7+03.2	000.7+04.7	001.2+02.1	001.4+05.3	001.6-01.3	002.1+03.3	002.8+01.7	006.0-03.6	351.2+05.2	354.2+04.3	358.9+03.2	17.60	32.30	43.70	
Ar ⁺	-7	6.99 ^b	5.97	9.39	<1.07	1.14	4.63	<0.81	26.90	1.74	47.20	17.60	32.30	43.70	7.69		
Ar ⁺²	-7	8.99	39.60	42.00	17.90	16.60	29.50	18.30	13.30	17.70	24.00	17.70	24.00	43.70	7.69		
Ar ⁺²	-7	21.8 ^b	35.10	34.70	15.30	18.40	31.80	14.40	20.70	20.60	18.60	27.80	27.80	44.40	7.69		
Ar ⁺²	-7	7135	20.70	25.70	13.90	10.80	17.20	...	5.76	15.70	4.71	8.23	8.23	14.90	7.69		
Ar ⁺³	+7	4712	11.50	6.88	7.69		
Ar ⁺³	-7	4740 ^b	9.59	5.96	7.69		
Ar ⁺⁴	-7	7.88	0.76	<0.44	<0.14	<0.15	<0.42	<0.34	<0.32	<0.25	<0.77	<0.50	<0.50	<0.31	7.69		
Ar ⁺⁴	-7	13.1 ^b	0.82	<0.11	<0.10	<0.23	0.24	<0.19	<0.14	<0.08	<0.13	<0.17	<0.17	<0.10	7.69		
Ne ⁺	-5	12.8 ^b	3.14	18.80	2.63	10.80	2.01	1.89	19.70	0.83	25.60	19.10	19.10	3.20	7.69		
Ne ⁺²	-5	15.5 ^b	21.80	8.43	11.70	3.59	20.90	13.50	0.12	13.70	1.04	6.67	6.67	28.20	7.69		
Ne ⁺²	-5	36.0 ^b	27.70	8.84	13.10	<4.54	23.30	12.80	<2.00	13.80	<2.87	7.97	7.97	25.90	7.69		
Ne ⁺²	-5	3869	3.93	...	3.04	10.40	...	0.90	0.90	...	7.69		
Ne ⁺⁴	-7	14.3 ^b	3.89	<0.26	<0.23	<0.35	0.87	<0.34	<0.31	<0.15	<0.46	<0.42	<0.42	<0.28	7.69		
Ne ⁺⁴	-7	24.3 ^b	5.22	<1.67	<0.31	<0.54	1.04	<0.34	<0.61	<0.40	<0.29	<0.39	<0.39	<1.02	7.69		
S ⁺	-7	6717 ^b	14.50	8.22	4.13	4.06	14.40	...	9.66	4.97	18.20	15.40	15.40	13.90	7.69		
S ⁺	-7	6731 ^b	18.20	7.86	4.55	3.31	18.60	...	11.00	5.23	18.70	18.40	18.40	14.50	7.69		
S ⁺²	-7	18.7 ^b	99.30	77.60	49.20	66.50	88.00	46.90	81.10	57.20	118.00	105.00	105.00	94.00	7.69		
S ⁺²	-7	33.4 ^b	92.30	71.10	45.50	62.90	86.50	43.30	75.70	55.10	115.00	99.90	99.90	85.10	7.69		
S ⁺²	-7	6312	25.30	29.90	30.50	16.00	55.10	...	23.10	23.10	14.70	7.69		
S ⁺³	-7	10.5 ^b	73.90	5.99	18.80	2.88	50.80	28.00	0.31	38.10	0.61	6.76	6.76	38.90	7.69		
O ⁺	-6	3728 ^b	128.00	31.20	279.00	582.00	582.00	...	7.69		
O ⁺	-6	7327 ^b	225.00	179.00	261.00	240.00	113.00	32.90	218.00	534.00	534.00	143.00	7.69		
O ⁺²	-6	4959 ^b	174.00	117.00	218.00	111.00	289.00	401.00	7.88	43.70	43.70	130.00	7.69		
O ⁺²	-6	5007 ^b	170.00	118.00	237.00	99.50	284.00	...	7.36	401.00	9.72	44.50	44.50	131.00	7.69		
O ⁺³	-6	25.8 ^b	157.00	<0.43	<0.08	<0.18	41.80	<0.09	<0.16	0.41	<0.10	<0.10	<0.10	3.11	7.69		

^aTo get abundances, multiply numbers in table by 10^x.

^bIonic lines used to calculate total elemental abundances (§3.5.1).

Table 3.10 Comparison of total elemental abundances for individual Bulge PNe. Obtain abundances relative to hydrogen by multiplying the numbers in the Table by 10^x where x is -6 for argon, -4 for neon, -5 for sulfur, and -4 for oxygen.

PNG Number	This work						RPDM97 ^a						CMKAS00 ^b						ECM04 ^c						WL07 ^d					
	Ar	Ne	S	O	Ar	O	Ar	Ne	S	O	Ar	S	O	Ar	Ne	S	O	Ar	Ne	S	O	Ar	Ne	S	O					
000.7+03.2	5.2	3.7	1.9	5.1	4.8	5.1	0.56	0.62	2.1	7.1	2.0	10.0		
000.7+04.7	5.4	2.7	0.88	3.0	4.4	...	0.36	1.9		
001.2+02.1	2.0	1.5	0.70	4.9	1.7	0.35	0.46	3.0		
001.4+05.3	2.5	1.4	0.71	3.5	1.9:	0.56	4.9		
001.6-01.3	4.6	3.2	1.6	3.3		
002.1+03.3	1.8	1.5	0.73		
002.8+01.7	5.3	2.0	0.89	1.2		
006.0-03.6	2.8	1.9	0.99	4.3	2.3	1.1	0.85	4.8	1.9	0.98	1.3	4.6		
351.2+05.2	7.1	2.7	1.4	2.6	2.9	...	2.3	2.2		
354.2+04.3	5.3	2.6	1.3	6.0	3.8	1.6	0.71	7.2		
358.9+03.2	6.5	4.0	1.4	2.8	5.6	5.1	0.36	9.3	3.6:	1.2	6.3		

^aRatag et al. (1997).

^bCuisinier et al. (2000). The colon (:) denotes low quality abundances due to a lack of data.

^cEscudero et al. (2004).

^dWang & Liu (2007).

3.5.2 Crystalline Silicates

Crystalline silicate features are present around 28 and 33 μm in the spectra of all GBPNe in our sample, while no amorphous silicate features are observed. In order to illustrate the crystalline silicate features more clearly, we define and subtract a continuum determined by a smooth spline fit to feature-free regions of each spectrum. Figure 3.1 shows the spline fit to the spectral continua and Figure 3.2 shows the continuum-subtracted spectra. The spline fit continuum is physically meaningless, and we only use it to elucidate the crystalline silicate features. Following Molster (2000) we identify the 28 micron complex (26.5 – 31.5 μm) and 33 micron complex (31.5 μm to past the end of our spectra) both as having features originating from the magnesium-rich crystalline silicates forsterite (Mg_2SiO_4) and enstatite (MgSiO_3).

The strength of the silicate emission bands can give an approximate estimate of the crystalline dust temperatures. Matsuura et al. (2004) note that the absence of a 23.7 μm feature indicates that forsterite is cooler than 100 K. This feature is either not present or very weak in the spectra of our GBPNe, and thus the forsterite dust in these objects must be cold, with a temperature $\lesssim 100$ K.

3.5.3 PAHs

PAHs are present in six of the eleven GBPNe in our sample: PNG000.7+04.7, PNG002.8+01.7, PNG006.0-03.6, PNG351.2+05.2, PNG354.2+04.3, and PNG358.9+03.2. Absorption of energetic photons excites the PAH emission features at 6.2, 7.7, 8.6, 11.2, and 12.7 μm . PAHs which emit in this spectral range have on the order of tens to hundreds of carbon atoms (Schutte et al., 1993). C—C stretching and bending or deformations causes the 6.2 and 7.7 μm features, while in-plane C—H bending produces the 8.6 μm feature, and out-of-plane C—H

bending gives rise to the 11.2 and 12.7 μm features (Allamandola et al., 1989).

Table 3.11 gives the net integrated PAH fluxes. We calculate these by first subtracting a spline-fit continuum and then summing the remaining flux in each PAH wavelength range; if atomic lines are present, we subsequently subtract their flux to arrive at the net PAH flux. For the 7.7 μm PAH, we subtract the H I line at 7.46 μm (and for PNG006.0-03.6 and PNG358.9+03.2 the 7.32 μm line as well). For the 12.7 μm PAH, we remove the contribution from the Ne^+ line at 12.81 μm ; however, the 12.7 μm PAH is much weaker than the 12.81 μm Ne^+ line, and thus the net 12.7 μm PAH flux is very uncertain. The 11.29 μm H I is weak and always near the $3\text{-}\sigma$ upper limit in our spectra; it contributes less than 5% to the 11.2 μm PAH flux (except for PNG006.0-03.6 and PNG358.9+03.2 where it may contribute up to 20%) and we do not remove it. Figure 3.3 shows plots of the continuum-subtracted, normalized PAH profiles.

3.6 Discussion

3.6.1 Elemental Abundances

Comparison of Abundances of Individual Objects with the Literature

In Table 3.10 we compare total elemental abundances from this work with abundances from four papers in the literature: Ratag et al. (1997); Cuisinier et al. (2000); Escudero et al. (2004); Wang & Liu (2007). All of these studies derive total elemental abundances from collisionally excited optical lines, and therefore their abundances are more dependent on the adopted extinction and electron temperature than the current study. A detailed comparison with these studies is hindered by the fact that only one study (Wang & Liu, 2007) lists their ionic abundances and ICFs. For individual objects, our total elemental abundances of

argon, neon, and sulfur tend to be higher than the optical abundances. This is due in part to the fact that the IR derived abundances for ions of Ar^{+2} , Ne^{+2} and S^{+2} always give a higher ionic abundance than the optically derived abundances for the same ions. On the other hand, the total elemental abundances of oxygen derived here do not have such a systematic offset because the main contributors to the total oxygen abundance, O^+ and O^{+2} , are determined from optical line fluxes which are taken from the same literature sources to which we compare abundances; PNG002.1+03.3 does not have an oxygen abundance listed in Table 3.10 because we could not find any optical line fluxes for this object.

Argon The values for the total argon abundance in this work are systematically higher than the values given in the literature (except in one case where the values are close). Several factors can lead to this offset: **(1)** In most cases, total elemental argon abundances in this work and prior studies of the GBPNe in our sample must use an ICF to account for unobserved Ar^{+3} ; different ICFs will lead to different total argon abundances. When the 4740 Å Ar^{+3} line is observed, our elemental argon abundance value agrees to within 30% of the values in the literature. **(2)** For the low excitation PNe (PNG002.8+01.7, PNG351.2+05.2, and PNG354.2+04.3, Excitation Class, EC~2–3), the IR data show that Ar^+ contributes significantly to the total argon abundance, and thus optical studies without observed Ar^+ must either use an ICF to account for it or risk underestimating the total argon abundance. **(3)** When we derive the Ar^{+2} ionic abundance from the IR lines and the optical 7135 Å line, we always get a value from the IR lines that is higher than that from the optical line (often within 50%, but sometimes off by a factor of a few), which causes many of our IR derived total argon abundances to be systematically higher than those derived in the literature. This may be due to the uncertainty in T_e when using optical lines to derive the Ar^{+2} abundance: lowering the electron

temperature by 1000 to 2000 K significantly increases the Ar^{+2} ionic abundance derived from the optical line (while only slightly increasing the Ar^{+2} ionic abundance derived from the IR lines), bringing the optical Ar^{+2} abundances into good agreement with the IR Ar^{+2} abundances in most cases.

Neon The values for the total neon abundance are systematically higher in this study than in the literature (in all except one case where the values are close). The factors that may cause this are: **(1)** The IR data show that Ne^+ is the dominant contributor to the total elemental neon abundance in roughly half of our GBPNe. There is no Ne^+ line observable in the optical, and thus the optical studies have not observed the most important ionization stage of neon for these PNe. **(2)** Lines of Ne^{+3} lie in the UV part of the spectrum, and thus our study and previous optical studies must use an ICF to account for it in high ionization nebulae (PNG000.7+03.2, PNG001.6-01.3, PNG006.0-03.6, and PNG358.9+03.2); different assumed ICFs could account for part of the discrepancy for these PNe. **(3)** When we derive the Ne^{+2} ionic abundance from the IR lines and the optical 3869 Å line, we always get a value from the IR lines that is higher than that from the optical. Similarly to Ar^{+2} , this may be due (at least in part) to the uncertainty in T_e having large effects on the optically derived abundances. Lowering the electron temperature by 1000 to 2000 K increases the Ne^{+2} ionic abundance derived from the optical line (while only slightly changing the Ne^{+2} ionic abundance derived from the IR lines), bringing the optical and IR derived Ne^{+2} abundances into better agreement.

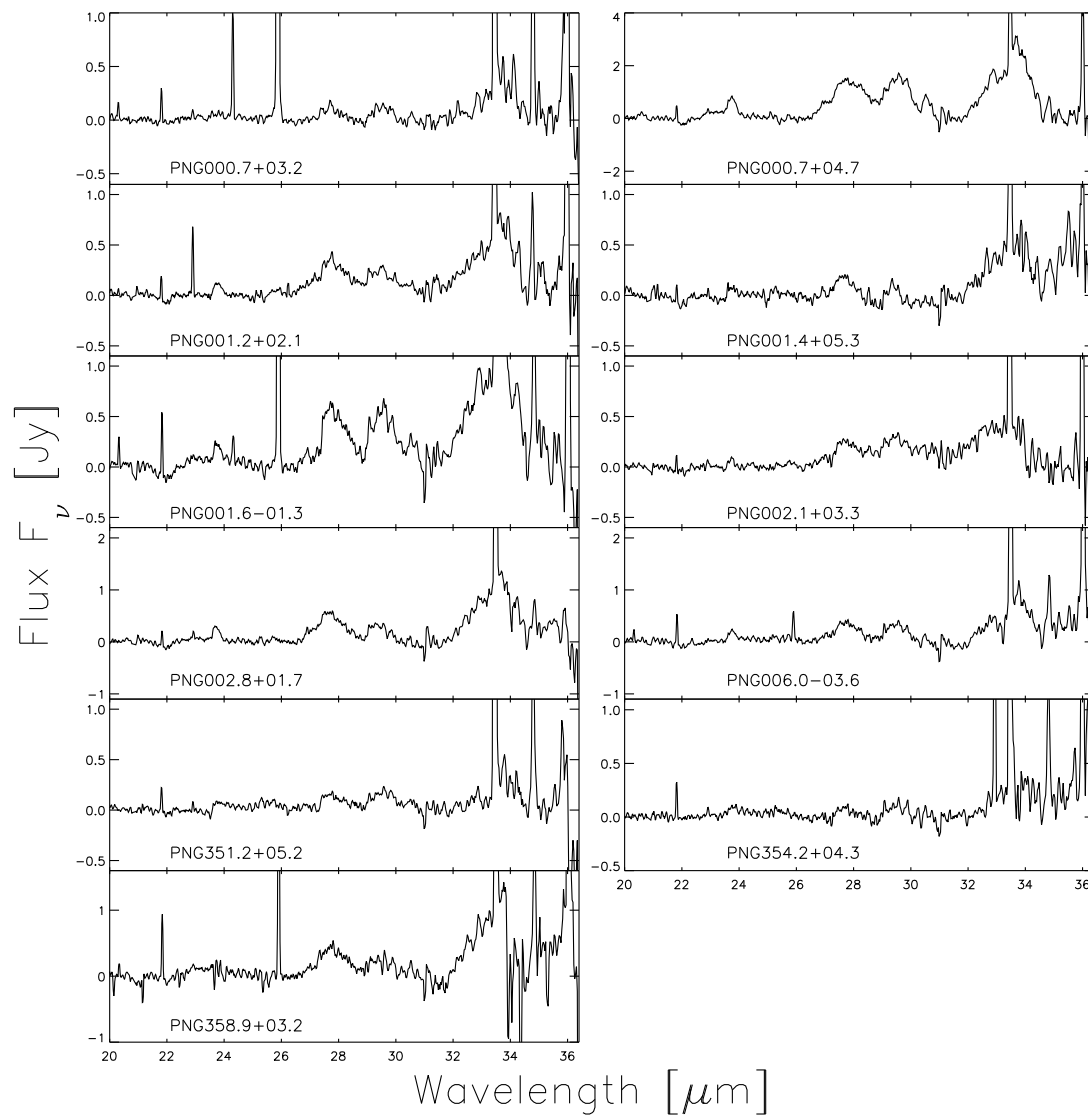


Figure 3.2 Continuum subtracted spectra showing the crystalline silicate features. See Figure 3.1 for the spline fit to the continuum.

Table 3.11 Net PAH feature fluxes

PNG Number	Net PAH Feature Fluxes (x 10 ⁻²⁰ W cm ⁻²)							
	6.2 μ m LR	7.7 μ m LR	8.6 μ m LR	11.2 μ m LR	11.2 μ m HR	12.7 μ m LR	12.7 μ m HR	
000.7+04.7	15.0 \pm 0.2	27.3 \pm 0.6	4.6 \pm 0.2	11.3 \pm 0.2	16.5 \pm 0.8	12. \pm 6.	12. \pm 6.	
002.8+01.7	5.3 \pm 0.1	8.4 \pm 0.7	2.49 \pm 0.08	6.08 \pm 0.07	7.6 \pm 0.5	9. \pm 6.	9. \pm 6.	
006.0-03.6	4.0 \pm 0.2	11.0 \pm 0.8	2.0 \pm 0.1	4.4 \pm 0.1	7.4 \pm 0.5	4.1 \pm 0.5	4.1 \pm 0.5	
351.2+05.2	29.0 \pm 0.9	40.8 \pm 0.7	10.0 \pm 0.1	22.0 \pm 0.3	24.0 \pm 0.5	11. \pm 4.	11. \pm 4.	
354.2+04.3	5.0 \pm 0.2	8.1 \pm 0.3	2.2 \pm 0.1	6.32 \pm 0.08	7.4 \pm 0.5	7. \pm 4.	7. \pm 4.	
358.9+03.2	2.1 \pm 0.3	4.7 \pm 0.6	1.4 \pm 0.2	3.4 \pm 0.2	3.4 \pm 0.8	1. \pm 1.	1. \pm 1.	

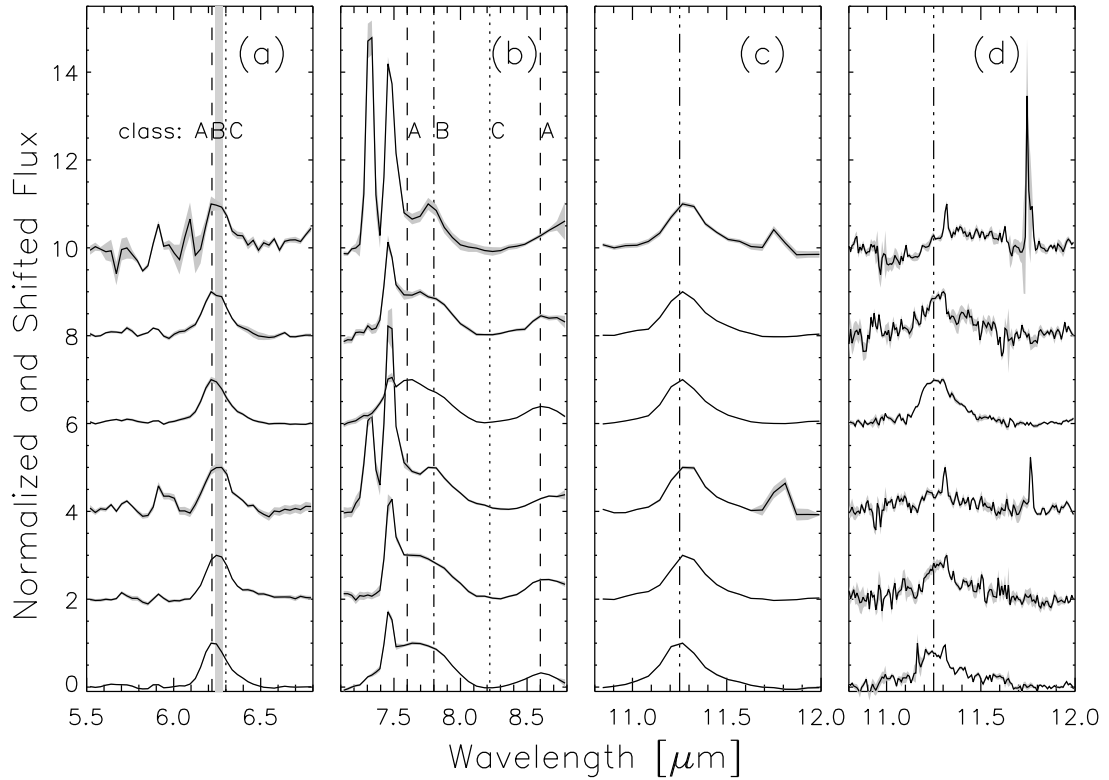


Figure 3.3 Profiles of PAH features for PNG358.9+03.2, PNG354.2+04.3, PNG351.2+05.2, PNG006.0-03.6, PNG002.8+01.7, and PNG000.7+04.7 (from top to bottom). **(a)** Profiles of $6.2 \mu\text{m}$ PAHs in LR. The dashed line indicates class A PAHs; the grey shaded area indicates class B; the dotted line indicates class C. **(b)** Profiles of $7.7 \mu\text{m}$ and $8.6 \mu\text{m}$ PAHs in LR. The dashed lines indicate class A PAHs; the dot-dashed line, class B; the dotted line, class C. **(c)** Profiles of $11 \mu\text{m}$ PAH in LR. **(d)** Profiles of $11 \mu\text{m}$ PAH in HR.

Sulfur Most of the values for our total sulfur abundance are higher than those given in the literature. This is due in part at least to having derived a higher S^{+2} abundance from the IR lines as compared to the optical line. The major contributors to the total elemental sulfur abundance are S^{+2} and S^{+3} , both observed in our IR spectra. The optical S^{+2} line at 6312 \AA is often weak and quite sensitive to T_e , and S^{+3} is not observed in the optical (Ratag et al., 1997). We use optical lines to determine the abundance of S^+ , but this is not a major contributor to the total sulfur abundance.

Oxygen Our values for the total oxygen abundance usually agree to within a factor of two of those in the literature, and often within 50%. For the one case where we can compare to the study in the literature with published ionic abundances (Wang & Liu, 2007), the ionic abundance of O^+ is higher by 50% in this work than in that study, but the ionic abundance of O^{+2} (the dominant ion) is lower by 10% than in that study, and the total elemental oxygen abundances agree within 10%. The IR data show that for one object (PNG000.7+03.2), the O^{+3} contributes significantly ($\sim 30\%$) to the total oxygen abundance, and thus optical studies must either use an uncertain ICF or underestimate the total oxygen abundance in this object.

Considering that we employ more observed stages of ionization than purely optical studies and also that we derive ionic abundances for the major contributors to the total elemental abundances for argon, neon, and sulfur from IR lines (which are less sensitive to $C_{H\beta}$ and T_e than abundances from optical lines), our GBPNe abundances for these elements are more accurate than previous studies. Our GBPNe abundance of oxygen, however, should be of similar accuracy to previous optical studies because we must rely on optical lines for the dominant ionization stages, but we make a slight improvement by measuring or placing an upper limit on the abundance from the O^{+3} infrared line.

Comparison of Mean Abundances with the Literature

We compare our mean Bulge abundance from the GBPNe to mean Bulge abundances derived from other GBPNe abundance studies, red giant stars, and H II regions in Table 3.12. The mean abundances of our GBPNe generally agree well with mean abundances of GBPNe determined from the optical studies. The mean neon abundances are the most discrepant, with ours being a factor of ~ 2 higher than those in the literature (reasons for such a discrepancy are given in §3.6.1). Our

mean argon and sulfur abundances are within the range of the previous studies, while our mean oxygen abundance is only slightly lower.

Cunha & Smith (2006) derive abundances for seven red giant stars in the Bulge, Lecureur et al. (2007) forty-seven, and Fulbright et al. (2007) twenty-five. Cunha & Smith (2006) derive oxygen abundances from lines of OH vibrational-rotational molecular transitions observed in infrared spectra, while Lecureur et al. (2007) and Fulbright et al. (2007) derive oxygen abundances from the [O I] line at 6300 Å in optical spectra. The oxygen abundances of our GBPNe fall well within the range of values for red giants from these studies, but the mean oxygen abundance of the GBPNe is a factor of ~ 2 lower than that of the red giants. However, given the uncertainties, small sample size, and different methods used, there is a good agreement.

Simpson et al. (1995) give abundances derived from IR lines for 18 H II regions between 0 and 10 kpc from the Galactic Center, while Martín-Hernández et al. (2002) use *ISO* spectra to derive abundances of 26 H II regions between 0 and 14 kpc (distances for both studies were redetermined so that $R_{\odot}=8.0$ kpc). In order to determine a mean H II region Bulge abundance from these studies, we take the mean of all H II regions in each study within 4 kpc of the Galactic Center. The Bulge H II region abundances from these two studies generally agree well with our GBPNe abundances, but the Bulge oxygen abundance of Simpson et al. (1995) and Bulge argon abundance of Martín-Hernández et al. (2002) are a factor of ~ 2 higher. There are only 5 objects in the central 4 kpc of Simpson et al. (1995) and only 3 in the central 4 kpc of Martín-Hernández et al. (2002) (and only 11 in our GBPNe sample), and thus the small size of the samples may suggest that the mean does not reflect a true average of the whole Bulge population. Our mean sulfur abundance is the same as that of Martín-Hernández et al. (2002), but over a factor

Table 3.12 Comparison of mean Bulge abundances. Obtain abundances relative to hydrogen by multiplying the numbers in the Table by 10^x where x is -6 for argon, -4 for neon, -5 for sulfur, and -4 for oxygen. References: RPD97 = Ratag et al. (1997), CMKAS00 = Cuisinier et al. (2000), ECM04 = Escudero et al. (2004), WL07 = Wang & Liu (2007), CS06 = Cunha & Smith (2006), LHZ07 = Lecureur et al. (2007), FMR07 = Fulbright et al. (2007), SCREH95 = Simpson et al. (1995), and MHPM02 = Martín-Hernández et al. (2002).

Study	Ar/H	Ne/H	S/H	O/H
PNe				
Current	4.4	2.5	1.1	3.7
RPD97	3.8	0.98	1.0	5.2
CMKAS00	2.1	...	0.78	5.4
ECM04	4.7	0.75	0.63	3.9
WL07	2.0	1.2	1.1	5.1
Red Giant Stars				
CS06	7.3
LHZ07	8.8
FMR07	6.2
H II Regions				
SCREH95	...	2.5	2.7	12
MHPM02	7.9	2.4	1.1	...

of two smaller than that of Simpson et al. (1995). Interestingly, while our mean GBPNe neon abundance is a factor of ~ 2 higher than previous GBPNe studies, it agrees very well with the mean Bulge H II region neon abundances from these studies.

In order to compare abundances across the Disk as well as the Bulge of the Galaxy, we supplement our abundances of GBPNe with those of GDPNe that are derived from mainly IR lines in a similar way to the abundances derived in this work. They are mostly from Pottasch & Bernard-Salas (2006) who use chiefly *ISO* data (excluding the strange low metallicity Hu 1-2), and complemented with abundances of several GDPNe using mainly *Spitzer* data: NGC 2392 (Pottasch et al., submitted), M1-42 (Pottasch et al., 2007), and IC 2448 (Guiles et al., 2007), and additionally abundances of one PN (NGC 3918) that uses data from IRAS (Clegg et al., 1987). In Table 3.13 we compare mean abundances of PNe and H II regions with galactocentric distances in the range 0–4 kpc (Bulge), 4–8 kpc (Inner Disk) and beyond 8 kpc (Outer Disk). The abundances from PNe agree reasonably well with the abundances from H II regions derived by Martín-Hernández et al. (2002), but do not agree as well with the abundances from H II regions derived by Simpson et al. (1995). Ratios of abundances of the various α -elements to each other (for example, Ne/S, S/Ar, Ne/O) in both PNe and H II regions show flat behavior with galactocentric distance (within the uncertainties), as expected for elements which are thought to be made in the same processes in massive stars.

Nature of the Bulge

The absence or presence of an abundance gradient in the Bulge (and the magnitude of the gradient if present) gives insight into how the Bulge formed. If the Bulge has an abundance gradient, then it formed by dissipational collapse, where self-enhancement of abundances occurred as the collapse continued inwards. However,

Table 3.13 Abundances of PNe and H II regions across the Galaxy. Obtain abundances relative to hydrogen by multiplying the numbers in the Table by 10^x where x is -6 for argon, -4 for neon, -5 for sulfur, and -4 for oxygen.

Distance range (kpc)	Ar/H	Ne/H	S/H	O/H
PNe: This work + others (see §3.6.1)				
0–4	4.6	2.7	1.2	4.5
4–8	4.3	1.9	1.2	5.0
8–...	2.7	1.1	0.63	4.2
H II Regions: Simpson et al. (1995)				
0–4	...	2.5	2.7	12
4–8	...	1.5	1.2	5.6
8–...	...	0.68	0.76	3.6
H II Regions: Martín-Hernández et al. (2002)				
0–4	7.9	2.4	1.1	...
4–8	4.7	2.2	0.89	...
8–...	2.6	1.2	0.65	...

if the Bulge does not have an abundance gradient, then it formed by dissipationless collapse, where mergers of small protogalactic pieces caused an inhomogeneous collapse over a long period of time and the mergers mixed stars of different ages and metallicities. If the Bulge has only a shallow abundance gradient, then the gravitational potential of the bar in our Galaxy caused concentrated star formation at its center and the stars eventually left the Disk to become (part of) the Bulge (Minniti et al., 1995).

Several (mainly optical) studies of GBPNe point toward a slightly more metal-rich Bulge than Disk (Ratag et al., 1992; Cuisinier et al., 2000; Górny et al., 2004; Wang & Liu, 2007). However, Ratag et al. (1992) find that the average abundances of GBPNe cannot be predicted by the abundance gradient observed for GDPNe, hinting that stars in the Bulge are a distinct population from the Disk. Additionally, Górny et al. (2004) find that the O/H gradient becomes shallower and may even decrease in the most inner parts of the Disk based on their sample of GDPNe

towards the Galactic Center. On the other hand, Exter et al. (2004) find essentially no difference in abundances between their Bulge and Disk PNe samples; however, their results also point to a discontinuation of the Disk metallicity gradient. The large extinction toward the Bulge hinders optical studies of GBPNe. Thus, in this work we seek to confirm the results of the optical studies using mainly infrared data.

In order to discover if the abundance trend in the Disk continues in the Bulge, Figure 3.4 shows abundances of argon, neon, sulfur, and oxygen versus galactocentric distance for both the GBPNe and GDPNe (GDPNe data discussed in §3.6.1). We fit lines to the plots of GBPNe and GDPNe abundances versus galactocentric distance in this figure separately (excluding from the fit to the oxygen abundance the four GDPNe that are thought to have depleted oxygen due to hot bottom burning, as discussed in Pottasch & Bernard-Salas 2006), and Table 3.14 gives parameters for these fits. The elemental abundance gradients of the GDPNe range from -0.08 to -0.14 dex/kpc and have uncertainties of 0.03 – 0.04 dex/kpc. In Figure 3.4 we also over plot the oxygen abundance gradient passing through the fit to the GDPNe abundances at 8 kpc on the plots for the other elements in order to illustrate that the abundances of the GBPNe are not consistent with the abundance versus galactocentric radius trend of GDPNe, whether the abundance data is fit directly to determine the gradient or if the shallower oxygen abundance gradient is assumed. The GBPNe have abundances significantly lower than the abundance in the Bulge predicted by the GDPNe abundance gradients.

Unfortunately the uncertainties in our fit to the abundance gradient of GBPNe do not allow us to determine if an abundance gradient is present in the Bulge; thus we cannot conclude anything about the specific method of Bulge formation. The large velocities of objects in the Bulge may smear out any abundance gradient

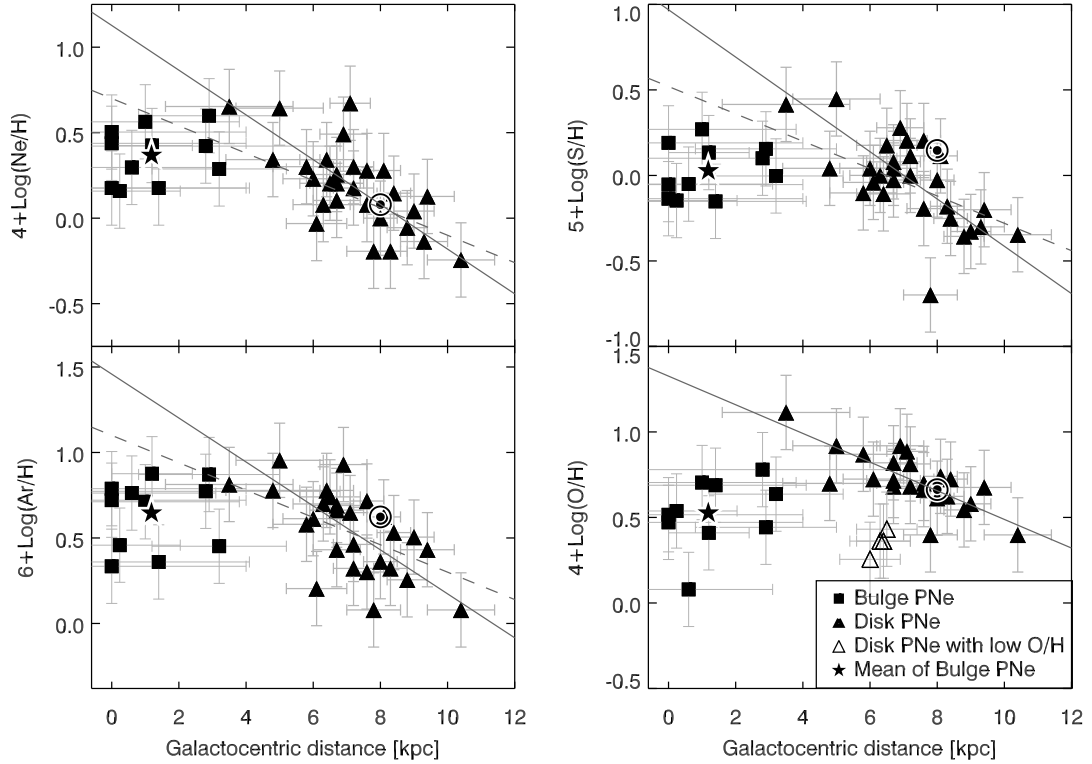


Figure 3.4 The argon, neon, sulfur, and oxygen abundances of GBPNe and GDPNe versus the galactocentric distance. GBPNe are represented by filled squares and GDPNe by filled triangles while the assumed solar metallicity as discussed in Pottasch & Bernard-Salas (2006) is represented by the sun symbol, and the star indicates the mean of the GBPNe abundances. The solid grey lines represent least squares fits to the GDPNe abundances, excluding from the fit to the oxygen abundance the four GDPNe that are thought to have depleted oxygen (as discussed in Pottasch & Bernard-Salas (2006); open triangles). The dashed grey lines in the plots of argon, neon, and sulfur represent the oxygen abundance slope passing through the solid line fit at 8 kpc. Coefficients of the linear fits to both GBPNe and GDPNe are given in Table 3.14. The GBPNe placed on the graph exactly at $R_{GC}=0.0$ kpc have unknown galactocentric distances and are not included when we perform a linear fit to the data. The y-axis range for all the plots spans 2.0 dex, so that equal slopes will look equal in the plots. Distance uncertainties are propagated from the statistical distance uncertainties while abundance uncertainties are assumed to be 50%.

Table 3.14 Parameters of linear fits to abundance gradients in GBPNe and GDPNe

Element	GBPNe		GDPNe	
	y-int (dex)	slope (dex/kpc)	y-int (dex)	slope (dex/kpc)
neon	0.0 ± 0.9	0.2 ± 0.3	1.1 ± 0.3	-0.13 ± 0.04
sulfur	-0.2 ± 0.6	0.2 ± 0.3	1.0 ± 0.3	-0.14 ± 0.04
argon	-12 ± 13	8 ± 260	1.5 ± 0.3	-0.13 ± 0.04
oxygen	-0.0 ± 0.9	0.3 ± 0.6	1.3 ± 0.3	-0.08 ± 0.03

that was originally present. However, the GBPNe abundances clearly do not follow the abundance gradient trend of GDPNe (see Figure 3.4): while the GBPNe have slightly higher average abundances than the GDPNe, they still fall far below the GDPNe abundance gradient extrapolated into the Bulge. This corroborates optical studies which had previously shown a discontinuity between the Bulge and Disk abundance gradients, confirming the distinct nature of the Bulge compared to the Disk.

3.6.2 Crystalline Silicates

Prior to *ISO*, crystalline silicates had only been observed in solar system comets (e.g. Hanner et al., 1994) and in β Pic, a debris disk system (Knacke et al., 1993). *ISO* and now *Spitzer* have observed crystalline silicates in many sources. However, it is remarkable that we observe crystalline silicates in every single one of the GBPNe. We suggest here that this is because the GBPNe have disks.

In their *ISO* study of crystalline silicate dust around evolved stars, Molster (2000) and Molster et al. (2002) make mean continuum subtracted spectra for sources which are thought to have a dusty disk (disk sources) and sources which are expected to have a normal outflow (outflow sources). They find that the dust features of disk and outflow sources show definitive differences in strength, shape,

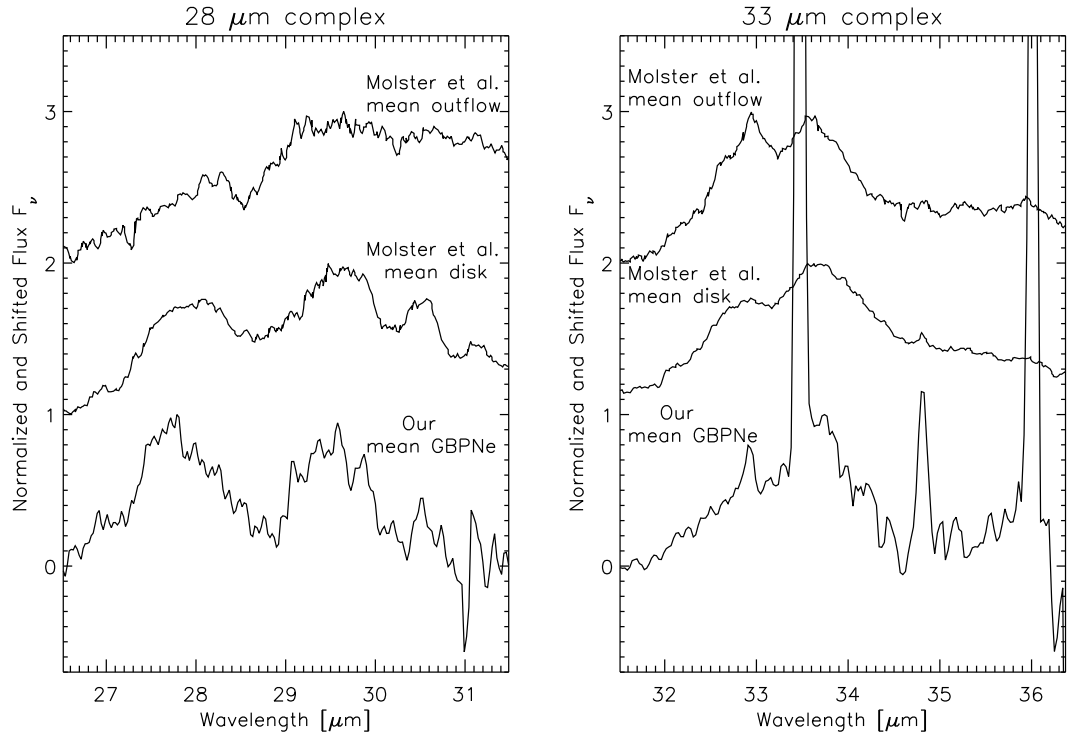


Figure 3.5 Normalized and shifted mean 28 and 33 μm spectra of our GBPNe compared to the mean disk and outflow sources from Molster et al. (2002).

and position of their dust features. In Figure 3.5 we plot normalized mean spectra of our GBPNe for the 28 and 33 μm features and compare them to the normalized mean disk and outflow spectra from Molster et al. (2002). Both the 28 and 33 μm complexes in our GBPNe look similar to the mean disk sources in Molster et al. (2002), but Molster et al. (2002) have several cautions about their mean spectra (for example, the *ISO* SWS band 3E, which covers the $\sim 27.5\text{--}29.2$ μm , is known to have less reliable calibration). However, the similarity of the crystalline silicate dust features in our GBPNe to those of Molster’s disk sources gives indirect evidence that the silicates in our GBPNe are in disks.

If the crystalline silicates in these GBPNe are in fact in disks, then they point toward binary evolution of the progenitor stars. Edgar et al. (2007) ran numerical

models that show how a binary companion can shape the AGB wind to form a crystalline dust torus. In their models, the shock temperatures reached when the wind blows past the companion anneal the dust and make it crystalline. They conclude that “Crystalline dust torii provide strong evidence for binary interactions in AGB winds.” As we discuss later in §3.6.4, over half of the GBPNe in this study show dual chemistry, which also implies binary evolution.

In our GBPNe sample, all of the nebulae show crystalline silicates, indicative of oxygen-rich material. Previous studies have found a low C/O ratio in GBPNe compared to GDPNe (e.g. Walton et al., 1993a; Wang & Liu, 2007; Casassus et al., 2001). The higher fraction of O-rich PNe in the Bulge compared to the Disk implies that the Bulge should have a larger injection of silicate grains into its interstellar medium (ISM) than the Disk (Casassus et al., 2001).

3.6.3 PAHs

PAHs can be separated into different classes based on the position of their 6.2 μm and 7.7 μm peaks. Class A PAHs peak at shorter wavelengths than class B, which peak at shorter wavelengths than class C (Peeters et al., 2002). Figure 3.3 shows the peak positions for the different classes of PAHs along with the GBPNe PAH features. The GBPNe in this study have class A, AB, and B PAHs, and thus have PAH profiles similar to GDPNe. The lack of type C PAHs in the PNe indicates that their PAHs are all processed, i.e. the aliphatic component is negligible (Sloan et al., 2007).

The PAH flux ratios $F_{7.7\mu\text{m}}/F_{11.2\mu\text{m}}$ and $F_{6.2\mu\text{m}}/F_{11.2\mu\text{m}}$ both trace the ionization fraction of the PAHs, and are often plotted against each other in a figure. The GBPNe studied here have $F_{7.7\mu\text{m}}/F_{11.2\mu\text{m}}$ between 1 and 3, and $F_{6.2\mu\text{m}}/F_{11.2\mu\text{m}}$ between 0.5 and 1.4, and follow the same trend as Galactic Disk and Magellanic

Cloud PNe (Bernard-Salas et al., in preparation).

3.6.4 Dual Chemistry Nebulae

ISO detected crystalline silicates and PAHs simultaneously in [WR] PNe — those PNe with H-poor and C-rich WR-type central stars (Waters et al., 1998). This dual chemistry is unusual in GDPNe (Bernard-Salas & Tielens, 2005). However, in our sample of GBPNe, six of the eleven nebulae have dual chemistry, showing both crystalline silicates and PAHs in their spectra. The fraction of [WR] PNe is significantly larger in the Bulge than the Disk (Górny et al., 2004), and thus the large fraction of PNe in the Bulge exhibiting dual chemistry makes sense. Possible explanations for this dual chemistry include (Little-Marenin, 1986; Willems & de Jong, 1986; Waters et al., 1998; Cohen et al., 1999): (1) a thermal pulse recently ($\lesssim 1000$ years ago) turned an O-rich outflow into a C-rich one, and (2) the central star of the PN is in a binary system and the silicate grains orbit the system in a disk that existed long before the PN.

What explains how the majority of our GBPNe show dual chemistry? The explanation of a thermal pulse at the end of the AGB having suddenly changed the chemical composition of the central star from O-rich to C-rich within the last thousand years seems implausible because it is unlikely that we would catch so many GBPNe in this short stage (e.g. Lloyd Evans, 1991). A growing body of evidence supports the binary system with an old silicate disk explanation of dual chemistry in PNe and late-type stars (Waters et al., 1998; Molster et al., 2001; Matsuura et al., 2004). Taking one of these studies as an example, Matsuura et al. (2004) present mid-IR images of the post-AGB star IRAS 16279-4757 which shows both PAHs and crystalline silicates. Their images and model of this star imply that it has a C-rich bipolar outflow with an inner low-density C-rich region surrounded

by an outer dense O-rich torus, indicating that mixed chemistry and morphology are related; mixed chemistry may point to binary evolution.

Other evidence also suggests that many of our GBPNe probably have binaries with silicate disks: (1) $\sim 40\%$ of compact PNe in the Bulge have binary-induced morphologies (Zijlstra, 2007); (2) binary-induced novae are observed to be concentrated in the bulge of the galaxy M31 (e.g. Shafter & Irby, 2001; Rosino, 1973), and thus perhaps in the Bulge of our galaxy as well; (3) asymmetric (e.g. bipolar, quadrupolar) morphology is more common in PNe in high metallicity environments than in low metallicity ones (Stanghellini et al., 2003); (4) the current study showing the similarity of the mean GBPNe spectra to the mean disk spectra of Molster et al. 2002 (§3.6.2); and (5) the silicates are crystalline and not amorphous, indicating that they have been blasted over time and are likely stored in a disk (Molster et al., 1999). Thus it seems likely that the GBPNe in our sample with dual chemistry have a binary at their center with a silicate disk that formed long before the PN stage, while the PAHs reside in the PN outflow itself, possibly shooting out along the poles.

3.7 Conclusions

We extract the *Spitzer* IRS spectra of eleven PNe in the Bulge to study their abundances and dust properties. We conclude that:

(1) The abundances of argon, neon, sulfur, and oxygen are significantly lower in the PNe in the Bulge than the abundances for the Bulge predicted by the abundance gradient in the Disk, consistent with the idea that the Bulge and Disk evolved separately.

(2) All of the spectra in our sample of PNe in the Bulge show crystalline silicates, indicating that these crystalline silicates are likely stored in disks, which

would further imply that the progenitor stars of these PNe evolved in binary systems.

(3) Six of the eleven spectra of PNe in the Bulge in our sample show PAHs in addition to the crystalline silicates. This dual chemistry also points toward binary evolution: the PAHs are in the current PN outflow and the crystalline silicates reside in a old disk created by binary interaction.

This work is based in part on observations made with the *Spitzer Space Telescope*, which is operated by the Jet Propulsion Laboratory, California Institute of Technology under NASA contract 1407. Support for this work was provided by NASA through Contract Number 1257184 issued by JPL/Caltec. This research made use of the SIMBAD database, operated at CDS, Strasbourg, France.

CHAPTER 4

ABUNDANCES IN H II REGIONS ACROSS M51 FROM *SPITZER* SPECTRA

4.1 Introduction

Determining the elemental abundances of H II regions across disks of spiral galaxies gives important information about how they formed and evolved (see Chapter 1). However, only a small number of galaxies have direct measurements of abundances in H II regions across their entire disks, including the metal-rich nuclear regions, because it is difficult to detect the faint optical lines necessary for determining the electron temperature in these metal-rich regions. Thus astronomers employ indirect methods for determining abundances across external galaxies, such as the R_{23} method (Pagel et al., 1979) which relies on an empirical relation between strong line fluxes and abundances. These indirect methods imply abundances significantly above solar at the centers of many nearby spiral galaxies.

In this chapter we seek to employ data from the *Spitzer Space Telescope* (Werner et al., 2004) Infrared Spectrograph (IRS; Houck et al., 2004) in order to derive abundances from twelve H II regions across the galaxy M51, which has been thought to have a high central abundance since the early 1990's. For example, Vila-Costas & Edmunds (1992) inferred abundances of 15 H II regions across M51 from the empirical strong-line R_{23} method, finding an abundance gradient of -0.06 dex/kpc and a predicted oxygen abundance at the center of $12 + \log(\text{O}/\text{H}) = 9.54$ dex ($7.5 \times \text{O}/\text{H}_{\odot}$, adopting $(\text{O}/\text{H})_{\odot} = 4.6 \times 10^{-4}$ from Asplund et al. (2005)). They also found abundances greater than solar in all of the observed H II regions. Additionally, Diaz et al. (1991) employed spectrophotometric observations and theoretical photoionization models to indirectly determine abundances for six

giant H II regions across M51, and found abundances for these regions from 2.8 to $5.5 \times (\text{O}/\text{H})_{\odot}$.

Recently however, Bresolin et al. (2004) took deep optical spectra of several metal-rich H II regions within M51. They detected the faint lines necessary for determining the electron temperature, and thus were able to directly determine abundances. Their abundances for H II regions in M51 are the most accurate to date because they do not rely on indirect methods. Such direct determinations of the abundances give important information relevant to understanding how galaxies form and evolve as well as providing a check on indirect calculations of abundances. Strikingly, Bresolin et al. (2004) find that the oxygen abundances of the central metal-rich H II regions in M51 are a factor of several lower than found by the above studies (Diaz et al., 1991; Vila-Costas & Edmunds, 1992) which employ indirect methods. This finding suggests a flatter abundance gradient across M51 and implies that the empirical determination of abundances from strong lines may be in error, perhaps due to problems in the theoretical models employed in calibrating the indirect methods. In the ideal case we could directly determine abundances from lines in *Spitzer* infrared spectra of H II regions across M51 and test the results of Bresolin et al. (2004).

M51 (a.k.a. NGC 5194 and the Whirlpool) is a famous nearly face-on (inclination = 20° , Tully, 1974) grand-design spiral galaxy at a distance of 8.4 Mpc (Feldmeier et al., 1997). It was the first galaxy where the spiral structure was noticed (by Lord Rosse in 1845; Bailey et al., 2005), and the pronounced spiral structure is probably due to the tidal interaction with its companion galaxy, NGC 5195 (Salo & Laurikainen, 2001). Additionally, M51 harbors a supermassive black hole in its nucleus (Crane & van der Hulst, 1992).

Neon and sulfur are made in the α -process in massive stars, and thus we would

expect their abundance ratio to remain constant across a galaxy. IRS spectra of H II regions may show lines from ions of Ne^+ , Ne^{++} , S^{++} , and S^{3+} . These are the dominant ions which contribute to the neon and sulfur abundances in most H II regions, and thus we can estimate the total neon to sulfur ratio from these lines to see if it remains constant or varies across the galaxy. Rubin et al. (2007) made a similar study employing IRS data on H II regions across the galaxy M83.

In the following section (§4.2) we describe the observations and data reduction of both the *Spitzer* IRS maps and the $\text{H}\alpha$ map. We derive abundances in §4.3. §4.4 gives our results about the hardness of the radiation field and the neon to sulfur abundance ratio across M51, and we summarize what we learned in §4.5.

4.2 Observations and Data Reduction

4.2.1 Spitzer Data

For the present study we analyze the spectral maps of H II regions across M51 taken with *Spitzer* IRS by the Spitzer Infrared Nearby Galaxies Survey (SINGS) team (Kennicutt et al., 2003)¹. Specifically, we employ their Short-High module maps which cover the wavelength range from 10 to 19 μm at a resolution of $R \sim 600$. This wavelength range includes lines from Ne II, Ne III, Ne V, S III, and S IV. The data were taken in ‘mapping mode’ with an integration time of 30 seconds \times 2 cycles. The map was made by stepping the slit across each H II region in half-slit sized steps for redundancy in order to reduce the affects of under-sampling and issues with diffraction². Figure 4.1 shows IRS slit overlays on the SINGS $\text{H}\alpha$ map of M51. Table 4.1 lists the central positions of each H II region mapped, indexed by the letter (A–L) which labels each mapped H II region in Figure 4.1.

¹SINGS team website: <http://sings.stsci.edu/>

²For details see: http://ssc.spitzer.caltech.edu/irs/documents/specmap_bop/

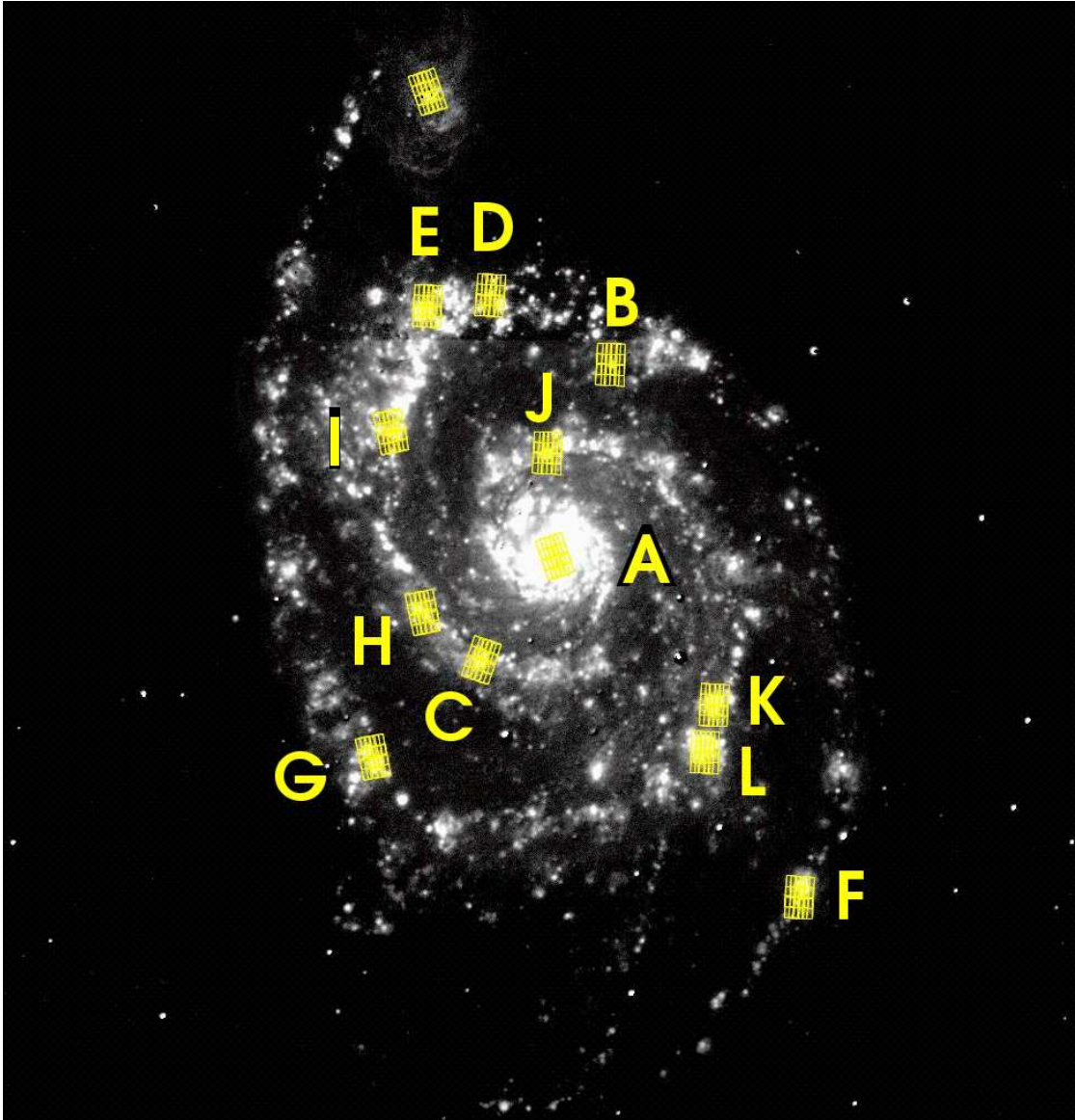


Figure 4.1 SINGS H α continuum subtracted image of M51 with overlays of the SH IRS maps. The region mapped by the IRS at the top of the image is NGC5195, the companion galaxy to M51.

We extract spectra processed through version S15.3 of the *Spitzer* Science Center’s pipeline with CUBISM³. Figure 4.2 displays IRS spectra of the M51 H II regions. The spectrum of the H II region in the nucleus (Region A) shows lines from Ne II, Ne III, Ne V, S III, S IV, and molecular hydrogen as well as features from Polycyclic Aromatic Hydrocarbon (PAH) at 11.2 and 12.7 μm . The extranuclear H II regions have weaker lines and do not show the high ionization Ne V or S IV lines.

Table 4.1 gives the area extracted for each region in steradians. Each extracted area was a rectangle approximately $15'' \times 26''$, or $\sim 600 \times 1000$ pc at the adopted distance of 8.4 Mpc to M51. Once we have the spectra we measure the fluxes in the spectral lines with SMART (Higdon et al., 2004) by fitting a gaussian to each line. Table 4.2 lists the observed line fluxes; most have uncertainties $<10\%$ and all have uncertainties $<20\%$. If a line is not detected, we calculate a 3σ upper limit by determining the flux in a gaussian of width given by the resolution of the instrument and of height three times the root mean square (RMS) deviation in the spectrum at the line’s wavelength.

³CUBISM (CUBe Builder for IRS Spectral Mapping) was developed at the University of Arizona by the SINGS team and is available from the Spitzer Science Center at Caltech.

Table 4.1 M51 H II region data

Region	Coordinates (J2000)		Observed H α flux ^a ($\times 10^{-13}$) erg cm ⁻² s ⁻¹ sr ⁻¹	Extracted Area ^b ($\times 10^{-8}$) sr	A _v ^c	T _e (K) ^d	
	RA	DEC				T _e (Ne II, S III)	T _e (Ne III, S IV)
A	13 29 52.7	47 11 43	21.0	1.17	4.00	6600 ^e	5800 ^e
B	13 29 49.7	47 13 29	0.56	1.17	...	6600 ^e	5800 ^e
C	13 29 56.7	47 10 46	2.32	1.17	2.17	6600 ^e	5800 ^e
D	13 29 56.2	47 14 07	2.20	1.17	2.61	6400 ^f	5600 ^f
E	13 29 59.6	47 14 02	5.68	1.27	1.01	6400	5600
F	13 29 39.5	47 08 36	3.46	1.16	2.24	7300	6800
G	13 30 02.5	47 09 52	6.78	1.36	0.91	6200 ^g	5400 ^g
H	13 29 59.8	47 11 13	2.50	1.36	3.11	6600 ^e	5800 ^e
I	13 30 01.6	47 12 52	3.60	1.17	3.57	6600 ^e	5800 ^e
J	13 29 53.1	47 12 40	2.49	1.17	1.78	4800	3700
K	13 29 44.2	47 10 22	7.69	1.27	1.93	5700	4600
L	13 29 44.6	47 09 55	7.93	1.36	1.64	5700 ^f	4600 ^f

^aObserved H α flux from the region extracted by CUBISM for each H II region as discussed in §4.2.2.

^bRectangular area centered on each H II region and extracted with CUBISM; all areas $\sim 15 \times 26''$ or $\sim 600 \times 1000$ pc.

^cExtinctions from van der Hulst et al. (1988) from H α /radio. For two regions (E and J) the IRS map covered several H II regions of van der Hulst et al. (1988) and in these cases the A_v is the average of the extinctions from the covered regions.

^dTemperatures from Bresolin et al. (2004).

^eT_e is the average from the sample of Bresolin et al. (2004).

^fT_e is from a nearby H II region. T_e for region D is from region E; T_e for region L is from region K.

^gRegion G covers the regions 53 and 55 in Bresolin et al. (2004) and thus we average those temperatures.

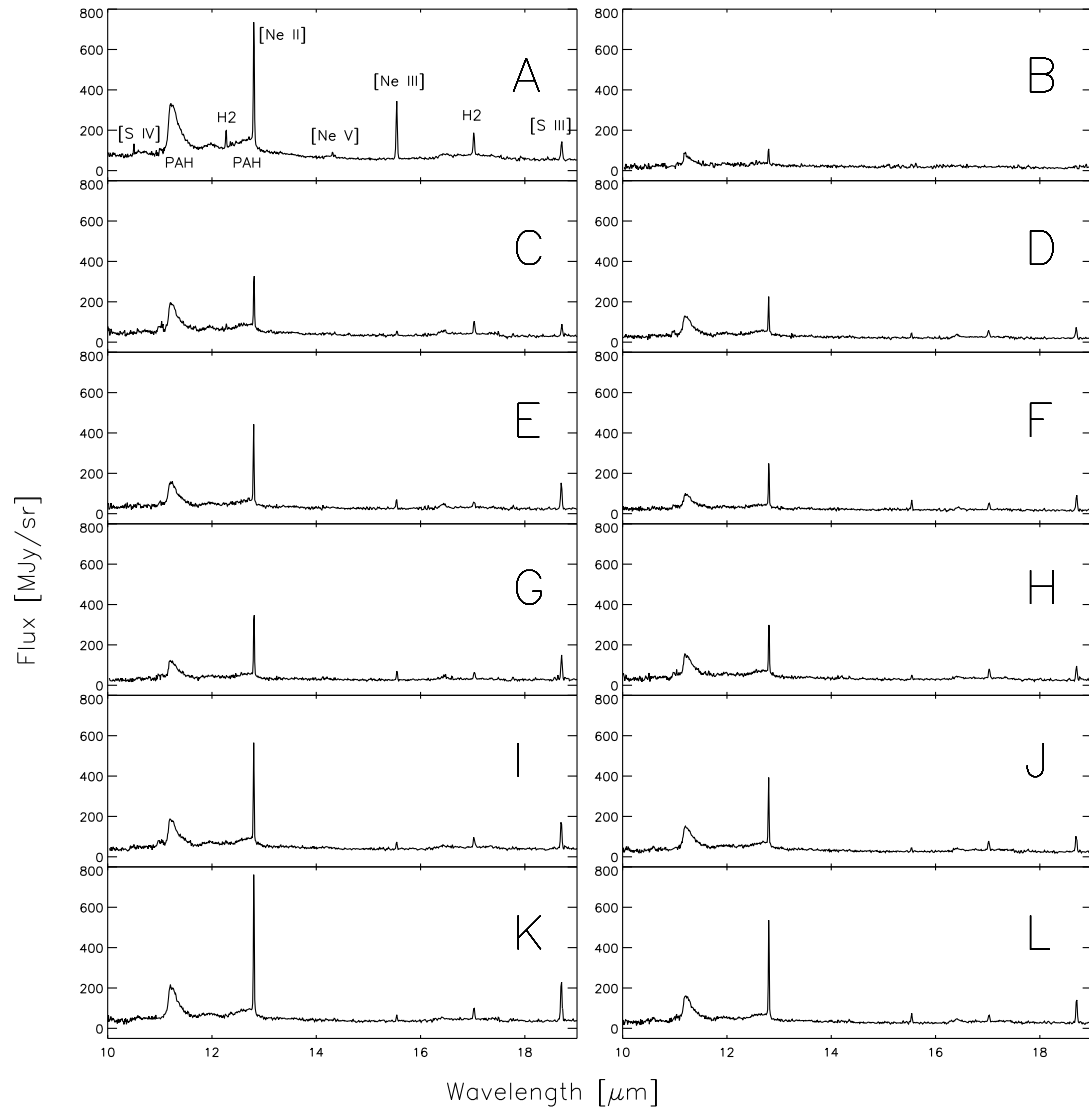


Figure 4.2 IRS spectra of H II regions in M51.

Table 4.2 M51 H II region line fluxes. Uncertainties are less than 10% unless otherwise noted. A less-than sign indicates a 3σ upper limit as discussed in §4.2.1.

Region	Observed line fluxes (10^{-6} erg cm $^{-2}$ s $^{-1}$ sr $^{-1}$)				
	S IV	Ne II	Ne V	Ne III	S III
	10.51 μ m	12.81 μ m	14.32 μ m	15.55 μ m	18.71 μ m
A	23	278	8.9 ^a	106	28
B	<42	34	<21	<25	<25
C	<33	111	<21	7.7 ^a	16 ^a
D	<27	68	<16	7.9 ^a	16
E	<36	150	<20	15	38
F	<30	89	<15	15 ^a	23
G	<33	134	<19	15	34
H	<38	110	<20	6.7 ^a	20
I	<34	189	<19	11 ^a	41
J	<40	128	<16	6.2 ^b	22
K	<43	276	<20	9.3	58
L	<41	186	<17	15	34

^aUncertainty between 10 and 15%.

^bUncertainty between 15 and 20%.

4.2.2 H α Map

This project originated out of a pilot effort to assess the feasibility of determining the abundances of H II regions across several galaxies from *Spitzer* IRS maps of these galaxies made by the IRS team here at Cornell and the SINGS team. Unfortunately, none of these IRS maps were deep enough for the hydrogen recombination lines to be observed in the spectra (the strongest H I line with a wavelength in the range of the SH module of the IRS being the H I(7-6) line at 12.36 μ m). Thus we made observations of these galaxies with the Wide-field InfraRed Camera (WIRC) on the Palomar 200" Hale Telescope in the Br- γ and Pa- β H I lines in order to determine the amount of hydrogen as well as the extinction in the IRS slits. Unfortunately we were unable to accurately determine the amount of hydrogen in the

IRS slits from these WIRC observations due to a combination of cloudy weather and the difficulty of obtaining a sufficiently high signal-to-noise ratio in the H I lines for the fainter H II regions.

As an alternate approach, we looked through the subset of galaxies mapped by the IRS that had an optical H I map and extinctions to the individual H II regions given in the literature. However, this approach has the problem that we must rely on optical measurements which are more affected by extinction and also on extinction values computed from different apertures than the area of the extracted IRS maps. We chose the galaxy M51 for this study because it had an H α map made by the SINGS team (see Figure 4.1) and extinctions given in the literature to all but one of the H II regions mapped with the IRS.

We tried two methods for determining the background in the SINGS H α map: (1) adopting a sky annulus chosen so that it does not fall on nearby H II regions, and (2) adopting a constant background determined from the average of the four corners of the array (where there is less contamination from H II regions in the galaxy). The two different types of background subtraction gave H α fluxes that agreed within 50%. We tested the sky subtraction methods by using them both to determine the H α fluxes in circular apertures of 6.5'' radius. We then compared these H α flux values with those for the same apertures published by the SINGS team (Calzetti et al., 2005) who adopted a background subtraction method which involved fitting a local background in each of twelve areas across the map and would be difficult to duplicate. The sky annulus did the best job of reproducing the Calzetti et al. (2005) results, with our H α flux values often within 20% of theirs (and almost all within a factor of 2), thus we adopt this sky subtraction method.

Due to the uncertainty in determining the amount of hydrogen in the extracted area of the IRS maps from the H α map and also the uncertainty in determining

the extinctions, unfortunately we are unable to determine accurate abundances with respect to hydrogen, although we describe the process below. However, we can determine more accurate abundance ratios because in such ratios the amount of hydrogen cancels out.

4.3 Data Analysis

4.3.1 Extinction Correction

We adopt extinctions for M51 H II regions from van der Hulst et al. (1988). They used 6 cm and 20 cm observations to determine the thermal radio emission and then determined the extinction from the $H\alpha$ to radio ratio. Depending on the size of the H II region, they used apertures from 12'' to 21'' in diameter. Additionally, they did 9''-aperture optical spectrophotometry on several H II regions and thus also determined Balmer-decrement extinctions for a subset of H II regions with $H\alpha$ /radio extinctions. Table 4.1 lists the A_v values we adopt for determining abundances.

4.3.2 Electron Temperature and Density

Table 4.1 also lists the temperatures for each region adopted for determining abundances. They are from Bresolin et al. (2004). The $T_e(\text{Ne II, S III})$ is the temperature we adopt for determining abundances from Ne II and S III line fluxes; similarly, the $T_e(\text{Ne III, S IV})$ is the temperature we adopt for determining abundances from Ne III and S IV line fluxes. The $T_e(\text{Ne II, S III})$ we adopt is equal to $T_e(\text{S}^{+2}, \text{Ar}^{+2})$ from Bresolin et al. (2004) because the ionization potential of Ne II (21.56eV) is close to that of S III (23.34eV) and Ar III (27.63eV). Similarly, the $T_e(\text{Ne III, S IV})$ we adopt is equal to $T_e(\text{S}^{+3}, \text{Ar}^{+3})$ from Bresolin et al. (2004) because the ionization potential of Ne III (29.65eV) is close to that of S IV (30.81eV) and Ar IV (31.66eV).

S IV) we employ is equal to $T_e(\text{O}^{+2}, \text{Ne}^{+2})$ of Bresolin et al. (2004) because the ionization potential of S IV (34.79eV) is close to that of O III (35.12eV) and Ne III (40.96eV). When Bresolin et al. (2004) do not give T_e for a given H II region, we adopt the average temperature from their sample. However, if an H II region without a T_e given by Bresolin et al. (2004) resides nearby another H II region with T_e given, then we adopt the T_e of the nearby region. Abundances derived from infrared lines depend only weakly on T_e , and thus choosing an average T_e or one from a nearby H II region will have little affect on the abundances.

For the electron density we assume $N_e = 100 \text{ cm}^{-3}$ for all H II regions in M51. Bresolin et al. (2004) determined that $N_e < 150 \text{ cm}^{-3}$ for the H II regions in M51, and the adopted electron density does not have a large affect on the abundances.

4.3.3 Abundances

We assume the above $\text{H}\alpha$ flux, extinction, electron temperatures and density in order to derive the abundances for each ion, following the procedure outlined in §1.3.3. Our procedure employs the $\text{H}\beta$ flux, so here we predict the observed $\text{H}\beta$ flux from the $\text{H}\alpha$ flux by using the theoretical ratio of $(\text{H}\alpha \text{ flux})/(\text{H}\beta \text{ flux}) = 3.0$ for case B recombination for a gas at $T_e=5000 \text{ K}$ and $N_e= 100 \text{ cm}^{-3}$ from Hummer & Storey (1987) and the extinction given in Table 4.1. Table 4.3 lists the ionic abundances (and upper limits for unobserved ions) for three ions of neon and two ions of sulfur. These abundances with respect to hydrogen should be viewed with caution because the $\text{H}\alpha$ flux has a large uncertainty; however, ratios of abundances will not be affected.

Table 4.3 Abundances in M51 H II regions.

Region	Ne ⁺ 12.81 μm ($\times 10^{-3}$)	Ne ⁺⁺ 15.55 μm ($\times 10^{-5}$)	Ne ⁺⁴ 14.32 μm ($\times 10^{-6}$)	S ⁺⁺ 18.71 μm ($\times 10^{-5}$)	S ⁺³ 10.51 μm ($\times 10^{-6}$)	Ne ⁺ +Ne ⁺⁺ ($\times 10^{-3}$)	S ⁺⁺ +S ⁺³ ($\times 10^{-5}$)
A	0.29	5.25	0.43	0.29	0.42	0.34	0.33
C	1.02	3.36	<8.93	1.51	<5.05	1.05	1.51
D	0.67	3.70	<7.31	1.56	<4.56	0.71	1.56
E	1.23	5.96	<7.60	3.13	<4.75	1.29	3.13
F	1.03	8.24	<8.75	2.55	<5.56	1.11	2.55
G	1.30	6.75	<8.26	3.31	<5.08	1.37	3.31
H	1.11	3.23	<9.36	2.01	<6.51	1.14	2.01
I	1.14	3.21	<5.42	2.45	<3.59	1.17	2.45
J	1.24	2.86	<6.35	2.22	<6.55	1.27	2.22
K	1.48	2.38	<4.80	3.19	<3.76	1.50	3.19
L	0.61	2.41	<2.40	1.12	<2.24	0.63	1.12

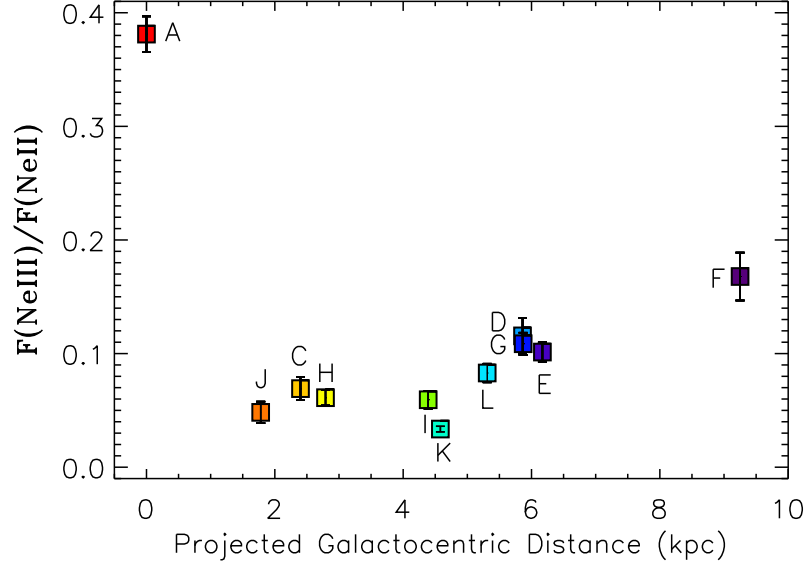


Figure 4.3 M51 H II region Ne III/Ne II flux ratio versus radial distance. The Ne III/Ne II flux ratio increases with increasing hardness of the radiation field.

4.4 Discussion

4.4.1 Ionizing Radiation Field

In Figure 4.3 we plot the Ne III/Ne II flux ratio (which indicates the hardness of the radiation field as discussed in §1.3.4) with respect to the projected galactocentric distance. For the extranuclear H II regions, the radiation field becomes harder as the distance from the galactic center increases. This is typical for extranuclear H II regions in galaxies, and could be due to decreasing stellar age and/or global abundance as the distance from the center increases: younger stars have harder radiation fields and stars with lower abundances also have harder radiation fields (due to less line blanketing) as discussed in §1.3.4 and seen in Figure 1.4. In the nucleus of M51 (Region A), the radiation field is much harder than in the extranuclear H II regions. The supermassive black hole in the nucleus of M51 causes the hard radiation field there.

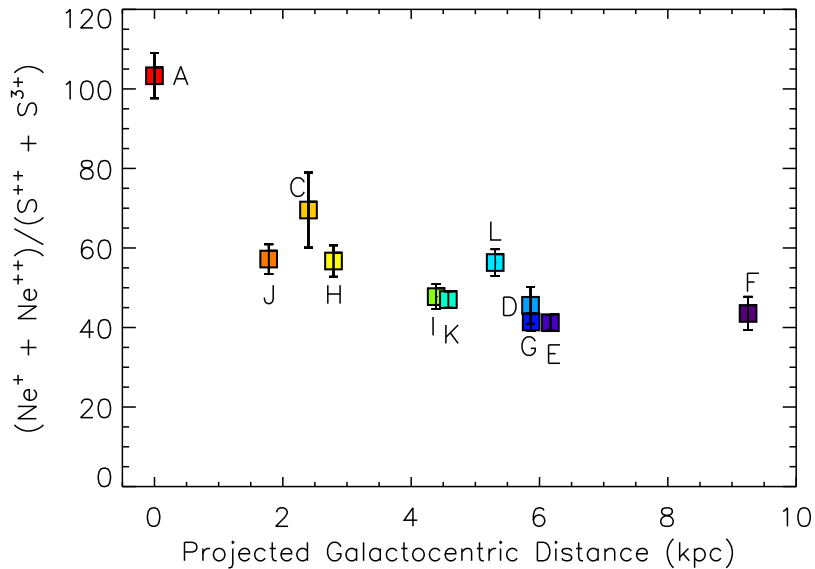


Figure 4.4 M51 $(\text{Ne}^+ + \text{Ne}^{++}) / (\text{S}^{++} + \text{S}^{3+})$ abundance ratio versus radial distance.

4.4.2 Neon to Sulfur Abundance Ratio

We do not plot the neon and sulfur abundances versus radial distance because the uncertainties (mainly due to calculating the amount of H^+ in the same region mapped with the IRS) on them are so large that they yield a scatter plot. (Comparing neon and sulfur abundances for regions in common with Bresolin et al. (2004) we are off by factors of a few.) Fortunately, the uncertainty on their abundance ratio is much smaller. Because we observe the dominant ionization states of neon and sulfur in these H II regions, we may approximate Ne/S by $(\text{Ne}^+ + \text{Ne}^{++}) / (\text{S}^{++} + \text{S}^{3+})$. We only observe the high ionization stage Ne^{+4} in the central H II region, and even there the abundance of Ne^{+4} is negligible compared to the abundances of Ne^+ and Ne^{++} , and we think that the sum of $\text{Ne}^+ + \text{Ne}^{++}$ should reliably trace the total neon abundance. However, none of the extranuclear regions have S^{3+} observed, and thus they are all relatively low excitation and S^+ may contribute significantly to their total sulfur abundance.

Figure 4.4 shows a plot of the $(\text{Ne}^+ + \text{Ne}^{++}) / (\text{S}^{++} + \text{S}^{3+})$ abundance ratio versus projected galactocentric distance. We assume that uncertainties in the line fluxes dominate this abundance ratio and propagate the uncertainties accordingly. We find that the Ne/S abundance ratio seems to decrease with increasing galactocentric radius. One would expect the Ne/S abundance ratio to be constant because both neon and sulfur are made in the same processes in massive stars. However, S^+ is not included in our trace of the Ne/S ratio, and S^+ probably contributes more to the total sulfur abundance in the inner H II regions that have softer radiation fields (see Figure 4.3); in addition, the inner metal-rich H II regions probably have a higher amount of dust (Sandford et al., 1995), which could lower the measured total sulfur abundance there because sulfur may be depleted onto the dust (while neon would not be depleted because it is chemically inert). Given these considerations, $(\text{Ne}^+ + \text{Ne}^{++}) / (\text{S}^{++} + \text{S}^{3+})$ probably gives an upper limit to the total neon to sulfur ratio. Rubin et al. (2007) also studied the neon to sulfur ratio as traced by $(\text{Ne}^+ + \text{Ne}^{++}) / (\text{S}^{++} + \text{S}^{3+})$ for H II regions across the galaxy M83 and found similar results, namely that Ne/S appeared to decrease with increasing radial distance.

4.5 Conclusions

We extracted *Spitzer* IRS spectra for twelve H II regions across the nearly face-on spiral galaxy M51. We measured line fluxes or upper limits for the following ions in each H II region: Ne^+ , Ne^{++} , Ne^{+4} , S^{++} , and S^{+3} ; lines from the ions of Ne^{+4} and S^{+3} were only observed in the nuclear H II region where a supermassive black hole resides, causing a hard radiation field. Then we derived abundances (or upper limits on the abundances) for these ions. However, we could not accomplish the original goal of determining accurate elemental abundances with respect to hydrogen across M51 because of the large uncertainty in the $\text{H}\alpha$ flux within each

extracted area along with the added uncertainty from adopting an extinction from a different sized aperture. We did find that in the extranuclear H II regions, the hardness of the radiation field as traced by the Ne III/Ne II flux ratio increases as the distance from the galactic center increases (attributed to decreasing abundance and/or stellar age with increasing distance). Additionally, we found that the neon to sulfur ratio as traced by $(\text{Ne}^+ + \text{Ne}^{++})/(\text{S}^{++} + \text{S}^{3+})$ appears to decrease with increasing distance from the nucleus, but this probably does not reflect a trend in the true Ne/S ratio, but rather reflects the affect of not accounting for unobserved S^+ and/or depletion of sulfur onto dust.

In order to determine accurate Ne/H and S/H abundances from *Spitzer* IRS spectra, it is necessary to measure the hydrogen within the IRS slit. The short integration time of the SINGS maps (1 minute at each pointing with a maximum integration time of 4 minutes at the center of the maps where the pointings overlap) is not long enough to detect the H I(7-6) line in the SH module of the *Spitzer* IRS. However, longer integration times of $\sim 15+$ minutes do allow the detection of this line in H II regions of external galaxies. For example, the program by Robert Rubin (program ID 20057) makes small maps of H II regions in M33 with a maximum integration time in the centers of the maps of 18 minutes, and they detect the H I(7-6) line, usually above the 3σ limit (private communication). A program by Fabio Bresolin (program ID 30205) does staring mode observations of ten H II regions in nearby galaxies with a 26 minute integration time on each region, and they should also detect the H I(7-6) line. Programs such as Rubin's and Bresolin's with integration times long enough to detect the H I(7-6) line are the way to determine accurate neon and sulfur abundances from infrared spectra of H II regions across galaxies. Future investigators will be able to determine abundances from infrared lines with the Mid-Infrared Instrument (MIRI) on the

James Webb Space Telescope (JWST); MIRI will provide high resolution ($R \sim 3000$) spectroscopy from 5 to 28 μm and thus cover the H I(7-6) at 12.37 μm as well as lines from important ionization stages of argon, neon, and sulfur.

BIBLIOGRAPHY

- Acker, A., Marcout, J., Ochsenbein, F., Stenholm, B., & Tylenda, R. 1992, Strasbourg - ESO catalogue of galactic planetary nebulae. Part 1; Part 2 (Garching: European Southern Observatory, 1992)
- Acker, A., Raytchev, B., Koeppen, J., & Stenholm, B. 1991, *A&AS*, 89, 237
- Allamandola, L. J., Tielens, G. G. M., & Barker, J. R. 1989, *ApJS*, 71, 733
- Asplund, M., Grevesse, N., & Sauval, A. J. 2005, in *ASP Conf. Ser. 336: Cosmic Abundances as Records of Stellar Evolution and Nucleosynthesis*, ed. T. G. Barnes, III & F. N. Bash, 25–+
- Bailey, M. E., Butler, C. J., & McFarland, J. 2005, *Astronomy and Geophysics*, 46, 26
- Ballero, S. K., Matteucci, F., Origlia, L., & Rich, R. M. 2007, *A&A*, 467, 123
- BBC. 2001
- Beaulieu, S. F., Dopita, M. A., & Freeman, K. C. 1999, *ApJ*, 515, 610
- Benjamin, R. A., Skillman, E. D., & Smits, D. P. 1999, *ApJ*, 514, 307
- Bensby, T. & Lundström, I. 2001, *A&A*, 374, 599
- Bernard-Salas, J. 2003, *Physics and Chemistry of Gas in Planetary Nebulae* (Thesis, University of Groningen)
- Bernard-Salas, J., Pottasch, S. R., Beintema, D. A., & Wesselius, P. R. 2001, *A&A*, 367, 949
- Bernard-Salas, J., Pottasch, S. R., Gutenkunst, S., Morris, P. W., & Houck, J. R. 2008, *ApJ*, 672, 274

- Bernard-Salas, J. & Tielens, A. G. G. M. 2005, *A&A*, 431, 523
- Bernstein, R. A., Freedman, W. L., & Madore, B. F. 2002, *ApJ*, 571, 107
- Berrington, K. A. 1985, *Journal of Physics B: Atomic and Molecular Physics*, 18, L395
- Berrington, K. A., Burke, P. G., Dufton, P. L., & Kingston, A. E. 1985, *Atomic Data and Nuclear Data Tables*, 33, 195
- Blum, R. D. & Pradhan, A. K. 1992, *ApJS*, 80, 425
- Bresolin, F., Garnett, D. R., & Kennicutt, Jr., R. C. 2004, *ApJ*, 615, 228
- Buonanno, R., Corsi, C. E., Pecci, F. F., Fahlman, G. G., & Richer, H. B. 1994, *ApJ*, 430, L121+
- Cahn, J. H., Kaler, J. B., & Stanghellini, L. 1992, *A&AS*, 94, 399
- Calzetti, D., Kennicutt, Jr., R. C., Bianchi, L., Thilker, D. A., Dale, D. A., Engelbracht, C. W., Leitherer, C., Meyer, M. J., Sosey, M. L., Mutchler, M., Regan, M. W., Thornley, M. D., Armus, L., Bendo, G. J., Boissier, S., Boselli, A., Draine, B. T., Gordon, K. D., Helou, G., Hollenbach, D. J., Kewley, L., Madore, B. F., Martin, D. C., Murphy, E. J., Rieke, G. H., Rieke, M. J., Roussel, H., Sheth, K., Smith, J. D., Walter, F., White, B. A., Yi, S., Scoville, N. Z., Polletta, M., & Lindler, D. 2005, *ApJ*, 633, 871
- Carollo, D., Beers, T. C., Lee, Y. S., Chiba, M., Norris, J. E., Wilhelm, R., Sivarani, T., Marsteller, B., Munn, J. A., Bailer-Jones, C. A. L., Fiorentin, P. R., & York, D. G. 2007, *Nature*, 450, 1020
- Carroll, B. W. & Ostlie, D. A. 1996, *Institute for Mathematics and Its Applications*

- Casassus, S., Roche, P. F., Aitken, D. K., & Smith, C. H. 2001, MNRAS, 327, 744
- Chiappini, C., Matteucci, F., & Gratton, R. 1997, ApJ, 477, 765
- Chiappini, C., Romano, D., & Matteucci, F. 2003, MNRAS, 339, 63
- Ciardullo, R., Bond, H. E., Sipior, M. S., Fullton, L. K., Zhang, C.-Y., & Schaefer, K. G. 1999, AJ, 118, 488
- Clegg, R. E. S., Harrington, J. P., Barlow, M. J., & Walsh, J. R. 1987, ApJ, 314, 551
- Cohen, M., Barlow, M. J., Sylvester, R. J., Liu, X.-W., Cox, P., Lim, T., Schmitt, B., & Speck, A. K. 1999, ApJ, 513, L135
- Cohen, M., Megeath, S. T., Hammersley, P. L., Martín-Luis, F., & Stauffer, J. 2003, AJ, 125, 2645
- Condon, J. J. & Kaplan, D. L. 1998, ApJS, 117, 361
- Crane, P. C. & van der Hulst, J. M. 1992, AJ, 103, 1146
- Cuisinier, F., Maciel, W. J., Köppen, J., Acker, A., & Stenholm, B. 2000, A&A, 353, 543
- Cunha, K. & Smith, V. V. 2006, ApJ, 651, 491
- Diaz, A. I., Terlevich, E., Vilchez, J. M., Pagel, B. E. J., & Edmunds, M. G. 1991, MNRAS, 253, 245
- Draine, B. T. 2003, ARA&A, 41, 241
- Draine, B. T. & Li, A. 2001, ApJ, 551, 807
- Durand, S., Acker, A., & Zijlstra, A. 1998, A&AS, 132, 13

- Edgar, R. G., Nordhaus, J., Blackman, E., & Frank, A. 2007, ArXiv e-prints, 709
- Eggen, O. J., Lynden-Bell, D., & Sandage, A. R. 1962, ApJ, 136, 748
- Eisenhauer, F., Genzel, R., Alexander, T., Abuter, R., Paumard, T., Ott, T., Gilbert, A., Gillessen, S., Horrobin, M., Trippe, S., Bonnet, H., Dumas, C., Hubin, N., Kaufer, A., Kissler-Patig, M., Monnet, G., Ströbele, S., Szeifert, T., Eckart, A., Schödel, R., & Zucker, S. 2005, ApJ, 628, 246
- Escudero, A. V., Costa, R. D. D., & Maciel, W. J. 2004, A&A, 414, 211
- Exter, K. M., Barlow, M. J., & Walton, N. A. 2004, MNRAS, 349, 1291
- Feldman, U. & Widing, K. G. 2003, Space Science Reviews, 107, 665
- Feldmeier, J. J., Ciardullo, R., & Jacoby, G. H. 1997, ApJ, 479, 231
- Ferland, G. J. 2003, ARA&A, 41, 517
- Ferreras, I., Wyse, R. F. G., & Silk, J. 2003, MNRAS, 345, 1381
- Fluks, M. A., Plez, B., The, P. S., de Winter, D., Westerlund, B. E., & Steenman, H. C. 1994, A&AS, 105, 311
- Fulbright, J. P., McWilliam, A., & Rich, R. M. 2007, ApJ, 661, 1152
- Galavis, M. E., Mendoza, C., & Zeppen, C. J. 1997, A&AS, 123, 159
- Galliano, F., Madden, S. C., Tielens, A. G. G. M., Peeters, E., & Jones, A. P. 2008, ArXiv e-prints, 801
- Górny, S. K., Stasińska, G., Escudero, A. V., & Costa, R. D. D. 2004, A&A, 427, 231

- Gregory, P. C., Vavasour, J. D., Scott, W. K., & Condon, J. J. 1994, *ApJS*, 90, 173
- Groenewegen, M. A. T., Udalski, A., & Bono, G. 2008, *ArXiv e-prints*, 801
- Guiles, S., Bernard-Salas, J., Pottasch, S. R., & Roellig, T. L. 2007, *ApJ*, 660, 1282
- Hanner, M. S., Lynch, D. K., & Russell, R. W. 1994, *ApJ*, 425, 274
- Helou, G., Walker, D. W., Helou, G., & Walker, D. W., eds. 1988, *Infrared astronomical satellite (IRAS) catalogs and atlases. Volume 7: The small scale structure catalog, Vol. 7*
- Herter, T., Briotta, Jr., D. A., Gull, G. E., Shure, M. A., & Houck, J. R. 1982, *ApJ*, 259, L109
- Higdon, S. J. U., Devost, D., Higdon, J. L., Brandl, B. R., Houck, J. R., Hall, P., Barry, D., Charmandaris, V., Smith, J. D. T., Sloan, G. C., & Green, J. 2004, *PASP*, 116, 975
- Houck, J. R., Roellig, T. L., van Cleve, J., Forrest, W. J., Herter, T., Lawrence, C. R., Matthews, K., Reitsema, H. J., Soifer, B. T., Watson, D. M., Weedman, D., Huisjen, M., Troeltzsch, J., Barry, D. J., Bernard-Salas, J., Blacken, C. E., Brandl, B. R., Charmandaris, V., Devost, D., Gull, G. E., Hall, P., Henderson, C. P., Higdon, S. J. U., Pirger, B. E., Schoenwald, J., Sloan, G. C., Uchida, K. I., Appleton, P. N., Armus, L., Burgdorf, M. J., Fajardo-Acosta, S. B., Grillmair, C. J., Ingalls, J. G., Morris, P. W., & Teplitz, H. I. 2004, *ApJS*, 154, 18
- Huggins, W. & Miller, W. A. 1864, *Philosophical Transactions of the Royal Society of London Series I*, 154, 437

- Hummer, D. G., Berrington, K. A., Eissner, W., Pradhan, A. K., Saraph, H. E., & Tully, J. A. 1993, *A&A*, 279, 298
- Hummer, D. G. & Storey, P. J. 1987, *MNRAS*, 224, 801
- Iben, Jr., I. & Renzini, A. 1983, *ARA&A*, 21, 271
- Kaler, J. B. 1985, *ARA&A*, 23, 89
- Karakas, A. I. 2003, *Asymptotic Giant Branch Stars: their influence on binary systems and the interstellar medium* (Thesis, Monash Univ. Melbourne. Available at <http://www.mso.anu.edu.au/~akarakas/research.html>)
- Karakas, A. I. & Lattanzio, J. C. 2003, *Publications of the Astronomical Society of Australia*, 20, 393
- Keenan, F. P., Aller, L. H., Bell, K. L., Hyung, S., McKenna, F. C., & Ramsbottom, C. A. 1996, *MNRAS*, 281, 1073
- Kennicutt, Jr., R. C., Armus, L., Bendo, G., Calzetti, D., Dale, D. A., Draine, B. T., Engelbracht, C. W., Gordon, K. D., Grauer, A. D., Helou, G., Hollenbach, D. J., Jarrett, T. H., Kewley, L. J., Leitherer, C., Li, A., Malhotra, S., Regan, M. W., Rieke, G. H., Rieke, M. J., Roussel, H., Smith, J.-D. T., Thornley, M. D., & Walter, F. 2003, *PASP*, 115, 928
- Kerber, F., Mignani, R. P., Guglielmetti, F., & Wicenec, A. 2003, *A&A*, 408, 1029
- Kingsburgh, R. L. & Barlow, M. J. 1994, *MNRAS*, 271, 257
- Knacke, R. F., Fajardo-Acosta, S. B., Telesco, C. M., Hackwell, J. A., Lynch, D. K., & Russell, R. W. 1993, *ApJ*, 418, 440

- Kwok, S. 2000, *The Origin and Evolution of Planetary Nebulae* (The origin and evolution of planetary nebulae / Sun Kwok. Cambridge ; New York : Cambridge University Press, 2000. (Cambridge astrophysics series ; 33))
- Lecqueur, A., Hill, V., Zoccali, M., Barbuy, B., Gómez, A., Minniti, D., Ortolani, S., & Renzini, A. 2007, *A&A*, 465, 799
- Leger, A., D'Hendecourt, L., & Boccarda, N., eds. 1987, *Polycyclic aromatic hydrocarbons and astrophysics; Proceedings of the NATO Advanced Research and CNRS Workshop, Les Houches, France, Feb. 17-22, 1986*
- Leitherer, C., Schaerer, D., Goldader, J. D., Delgado, R. M. G., Robert, C., Kune, D. F., de Mello, D. F., Devost, D., & Heckman, T. M. 1999, *ApJS*, 123, 3
- Li, A. & Draine, B. T. 2002, *ApJ*, 572, 232
- Little-Marenin, I. R. 1986, *ApJ*, 307, L15
- Lloyd Evans, T. 1991, *MNRAS*, 249, 409
- López-Corredoira, M., Hammersley, P. L., Garzón, F., Simonneau, E., & Mahoney, T. J. 2000, *MNRAS*, 313, 392
- Marigo, P., Bernard-Salas, J., Pottasch, S. R., Tielens, A. G. G. M., & Wesselius, P. R. 2003, *A&A*, 409, 619
- Marigo, P., Girardi, L., & Bressan, A. 1999, *A&A*, 344, 123
- Martín-Hernández, N. L., Peeters, E., Morisset, C., Tielens, A. G. G. M., Cox, P., Roelfsema, P. R., Baluteau, J.-P., Schaerer, D., Mathis, J. S., Damour, F., Churchwell, E., & Kessler, M. F. 2002, *A&A*, 381, 606
- Mathis, J. S. 1990, *ARA&A*, 28, 37

- Matsuura, M., Zijlstra, A. A., Molster, F. J., Hony, S., Waters, L. B. F. M., Kemper, F., Bowey, J. E., Chihara, H., Koike, C., & Keller, L. P. 2004, *ApJ*, 604, 791
- Matteucci, F., ed. 2001, *Astrophysics and Space Science Library*, Vol. 253, The chemical evolution of the Galaxy
- Matteucci, F. 2008, *ArXiv e-prints*, 803
- Matteucci, F. & Greggio, L. 1986, *A&A*, 154, 279
- McCarthy, J. K., Mould, J. R., Mendez, R. H., Kudritzki, R. P., Husfeld, D., Herrero, A., & Groth, H. G. 1990, *ApJ*, 351, 230
- Mellema, G. 2004, *A&A*, 416, 623
- Mendez, R. H., Kudritzki, R. P., & Herrero, A. 1992, *A&A*, 260, 329
- Mendoza, C. 1983, in *IAU Symposium*, Vol. 103, *Planetary Nebulae*, ed. D. R. Flower, 143–172
- Milingo, J. B., Henry, R. B. C., & Kwitter, K. B. 2002a, *ApJS*, 138, 285
- Milingo, J. B., Kwitter, K. B., Henry, R. B. C., & Cohen, R. E. 2002b, *ApJS*, 138, 279
- Minniti, D., Olszewski, E. W., Liebert, J., White, S. D. M., Hill, J. M., & Irwin, M. J. 1995, *MNRAS*, 277, 1293
- Molster, F. J. 2000, PhD thesis, FNWI: Sterrenkundig Instituut Anton Pannekoek, Postbus 19268, 1000 GG Amsterdam, The Netherlands
- Molster, F. J., Waters, L. B. F. M., & Tielens, A. G. G. M. 2002, *A&A*, 382, 222

- Molster, F. J., Yamamura, I., Waters, L. B. F., Nyman, L.-Å., Käufel, H.-U., de Jong, T., & Loup, C. 2001, *A&A*, 366, 923
- Molster, F. J., Yamamura, I., Waters, L. B. F. M., Tielens, A. G. G. M., de Graauw, T., de Jong, T., de Koter, A., Malfait, K., van den Ancker, M. E., Van Winckel, H., Voors, R. H. M., & Waelkens, C. 1999, *Nature*, 401, 563
- Osterbrock, D. E. 1989, *Astrophysics of gaseous nebulae and active galactic nuclei* (Research supported by the University of California, John Simon Guggenheim Memorial Foundation, University of Minnesota, et al. Mill Valley, CA, University Science Books, 1989, 422 p.)
- Pagel, B. E. J., Edmunds, M. G., Blackwell, D. E., Chun, M. S., & Smith, G. 1979, *MNRAS*, 189, 95
- Palen, S., Balick, B., Hajian, A. R., Terzian, Y., Bond, H. E., & Panagia, N. 2002, *AJ*, 123, 2666
- Peeters, E., Hony, S., Van Kerckhoven, C., Tielens, A. G. G. M., Allamandola, L. J., Hudgins, D. M., & Bauschlicher, C. W. 2002, *A&A*, 390, 1089
- Pottasch, S. R., ed. 1984, *Planetary nebulae - A study of late stages of stellar evolution*
- Pottasch, S. R. & Beintema, D. A. 1999, *A&A*, 347, 975
- Pottasch, S. R. & Bernard-Salas, J. 2006, *A&A*, 457, 189
- Pottasch, S. R., Bernard-Salas, J., Beintema, D. A., & Feibelman, W. A. 2004, *A&A*, 423, 593
- Pottasch, S. R., Bernard-Salas, J., & Roellig, T. L. 2007, *A&A*, 471, 865

- Pradhan, A. K., Montenegro, M., Nahar, S. N., & Eissner, W. 2006, MNRAS, 366, L6
- Quinn, P. J., Hernquist, L., & Fullagar, D. P. 1993, ApJ, 403, 74
- Ramsbottom, C. A., Bell, K. L., & Keenan, F. P. 1997, MNRAS, 284, 754
- Ramsbottom, C. A., Berrington, K. A., Hibbert, A., & Bell, K. L. 1994, Physica Scripta, 50, 246
- Ratag, M. A., Pottasch, S. R., Dennefeld, M., & Menzies, J. 1997, A&AS, 126, 297
- Ratag, M. A., Pottasch, S. R., Dennefeld, M., & Menzies, J. W. 1992, A&A, 255, 255
- Reid, M. J. 1993, ARA&A, 31, 345
- Rolleston, W. R. J., Smartt, S. J., Dufton, P. L., & Ryans, R. S. I. 2000, A&A, 363, 537
- Rosino, L. 1973, A&AS, 9, 347
- Rubin, R. H., Simpson, J. P., Colgan, S. W. J., Dufour, R. J., Ray, K. L., Erickson, E. F., Haas, M. R., Pauldrach, A. W. A., & Citron, R. I. 2007, MNRAS, 377, 1407
- Rubin, R. H., Simpson, J. P., Erickson, E. F., & Haas, M. R. 1988, ApJ, 327, 377
- Ruffle, P. M. E., Zijlstra, A. A., Walsh, J. R., Gray, M. D., Gesicki, K., Minniti, D., & Comeron, F. 2004, MNRAS, 353, 796
- Salo, H. & Laurikainen, E. 2001, Astronomical and Astrophysical Transactions, 20, 93

- Sandford, S. A., Pendleton, Y. J., & Allamandola, L. J. 1995, *ApJ*, 440, 697
- Schutte, W. A., Tielens, A. G. G. M., & Allamandola, L. J. 1993, *ApJ*, 415, 397
- Searle, L. & Zinn, R. 1978, *ApJ*, 225, 357
- Shafter, A. W. & Irby, B. K. 2001, *ApJ*, 563, 749
- Shaver, P. A., McGee, R. X., Newton, L. M., Danks, A. C., & Pottasch, S. R. 1983, *MNRAS*, 204, 53
- Simpson, J. P., Colgan, S. W. J., Rubin, R. H., Erickson, E. F., & Haas, M. R. 1995, *ApJ*, 444, 721
- Sloan, G. C., Jura, M., Duley, W. W., Kraemer, K. E., Bernard-Salas, J., Forrest, W. J., Sargent, B., Li, A., Barry, D. J., Bohac, C. J., Watson, D. M., & Houck, J. R. 2007, *ApJ*, 664, 1144
- Stanghellini, L., Shaw, R. A., Balick, B., Mutchler, M., Blades, J. C., & Villaver, E. 2003, *ApJ*, 596, 997
- Torres-Peimbert, S. & Peimbert, M. 1977, *Revista Mexicana de Astronomia y Astrofisica*, 2, 181
- Tully, R. B. 1974, *ApJS*, 27, 437
- Tylenda, R., Acker, A., Stenholm, B., & Koeppen, J. 1992, *A&AS*, 95, 337
- Tylenda, R., Siódmiak, N., Górny, S. K., Corradi, R. L. M., & Schwarz, H. E. 2003, *A&A*, 405, 627
- van de Steene, G. C. & Zijlstra, A. A. 1995, *A&A*, 293, 541
- van der Hulst, J. M., Kennicutt, R. C., Crane, P. C., & Rots, A. H. 1988, *A&A*, 195, 38

- Vassiliadis, E. & Wood, P. R. 1993, *ApJ*, 413, 641
- Vila-Costas, M. B. & Edmunds, M. G. 1992, *MNRAS*, 259, 121
- Walton, N. A., Barlow, M. J., & Clegg, R. E. S. 1993a, in *IAU Symposium*, Vol. 155, *Planetary Nebulae*, ed. R. Weinberger & A. Acker, 581–+
- Walton, N. A., Barlow, M. J., & Clegg, R. E. S. 1993b, in *IAU Symposium*, Vol. 153, *Galactic Bulges*, ed. H. Dejonghe & H. J. Habing, 337–+
- Wang, W. & Liu, X. . 2007, *ArXiv e-prints*, 707
- Waters, L. B. F. M., Beintema, D. A., Zijlstra, A. A., de Koter, A., Molster, F. J., Bouwman, J., de Jong, T., Pottasch, S. R., & de Graauw, T. 1998, *A&A*, 331, L61
- Werner, M. W., Roellig, T. L., Low, F. J., Rieke, G. H., Rieke, M., Hoffmann, W. F., Young, E., Houck, J. R., Brandl, B., Fazio, G. G., Hora, J. L., Gehrz, R. D., Helou, G., Soifer, B. T., Stauffer, J., Keene, J., Eisenhardt, P., Gallagher, D., Gautier, T. N., Irace, W., Lawrence, C. R., Simmons, L., Van Cleve, J. E., Jura, M., Wright, E. L., & Cruikshank, D. P. 2004, *ApJS*, 154, 1
- Willems, F. J. & de Jong, T. 1986, *ApJ*, 309, L39
- Woosley, S. E., Wilson, J. R., Mathews, G. J., Hoffman, R. D., & Meyer, B. S. 1994, *ApJ*, 433, 229
- Zhang, C. Y. 1995, *ApJS*, 98, 659
- Zijlstra, A. A. 2007, *Baltic Astronomy*, 16, 79
- Zuckerman, B. & Aller, L. H. 1986, *ApJ*, 301, 772